Mode I fatigue delamination growth in composite laminates

Design of an automated DCB test setup

Friso Oude Tanke

Supervisor: dr. ir. L. Warnet

Mechanical Engineering: Production Technology
Engineering Technology, University of Twente
March 2024

UNIVERSITY OF TWENTE.

SUMMARY

This master thesis presents the design and implementation of a setup to automate crack length measurement in a Double Cantilever Beam (DCB) fatigue testing method, which is used to characterize the delamination resistance of composite materials under fatigue conditions. The testing method employed adheres to the protocol established by the ESIS TC4 Committee, which is currently used to conduct a Round Robin test. The proposed setup uses a high-resolution camera and image processing algorithms to automatically detect and measure the crack length during the test, reducing the need for manual measurements and improving accuracy and repeatability.

The thesis discusses the implementation of the setup in an existing testing environment and presents the design considerations and trade-offs required to ensure reliable operation. Several challenges related to the control of the servo-electric testing machine, the Instron Electropuls E3000, are discussed in detail. Additionally, the setup required the development of a LabVIEW program for measuring delamination length, data acquisition & analysis and communication with the machine, which is also described in this work.

Overall, the proposed automated crack length measurement setup provides improvement over current manual measurements as described in the protocol, reducing the potential for manual errors, eliminating the observer bias and improving the time efficiency of the testing process. The developed setup is used to characterize two different materials. The results of this work demonstrate the feasibility and effectiveness of automated crack length measurements in composite fatigue testing, with potential application to test and characterize other materials.

Keywords: Automated crack length measurement, DCB fatigue testing, composite materials, image processing.

NOMENCLATURE

a	total delamination (crack) length, measured from the load line
a_0	initial delamination length in the test specimen, i.e., the length of the film used as a starter delamination, measured from the load line
a_p	length of the delamination after the first pre-crack, measured from the load line
$a_p - a_0$	length of the pre-crack extension
da/dN	fatigue crack growth (FCG) rate, rate of delamination growth per cycle
N	number of fatigue cycles
A	a constant in the Hartman-Schijve equation
D	a constant in the Hartman-Schijve equation
n	an exponent in the Hartman-Schijve equation
G	energy release-rate
G_C	quasi-static interlaminar fracture energy
G_{C0}	quasi-static initiation value of G_C
G_{max}	maximum applied energy release rate in a fatigue cycle
G_{min}	minimum applied energy release rate in a fatigue cycle
ΔG	range of the applied energy release rate in the fatigue cycle, defined as $\Delta G = G_{max} - G_{min}$
$\Delta\sqrt{G}$	range of the applied energy release rate in the fatigue cycle, defined as $\Delta\sqrt{G} = \sqrt{G_{max}} - \sqrt{G_{min}}$
$\Delta\sqrt{G_{thr}}$	range of the fatigue threshold value of $\Delta\sqrt{G}$, defined as $\Delta\sqrt{G} = \sqrt{G_{max}} - \sqrt{G_{min}}$
$\Delta\sqrt{G_{max,thr}}$	threshold value of $\sqrt{G_{max}}$
$\Delta\sqrt{G_{min,thr}}$	threshold value of $\sqrt{G_{min}}$
R	load ratio
σ	standard deviation
δ	displacement
P	force
C	compliance
B	width of the specimen
h	half the thickness of the specimen
N	finite displacement correction to account for load-block effects
F	correction factor to account for large displacements
m	constant in the MCC-method
I	Mode I (tensile crack opening load)
$CFRP$	continuous fibre reinforced polymer
DCB	double cantilever beam
FCG	fatigue crack growth
SBT	simple beam theory
CBT	corrected beam theory
MCC	modified compliance calibration

CONTENTS

1 INTRODUCTION

1.1 Fracture toughness characterisation

Composite materials, or more specifically Continuous Fiber Reinforced Polymers (CFRPs), are widely used in various engineering applications due to their high specific strength and stiffness. CFRP laminates consist of multiple, stacked layers (plies) which are highly anisotropic due to fibers laying in a specific direction, see Figure 1.1. By the ability to orientate each ply in a different direction, a material can be created which can withstand forces for specific use cases. These outstanding material characteristics combined with a low density make CFRPs the material of choice for high-tech applications, such as aeronautical and space applications. However, fibers are bonded with a matrix material, which has much lower strength, resulting in a lack of reinforcement in the thickness direction and the direction perpendicular to the fibers (the 2-direction).

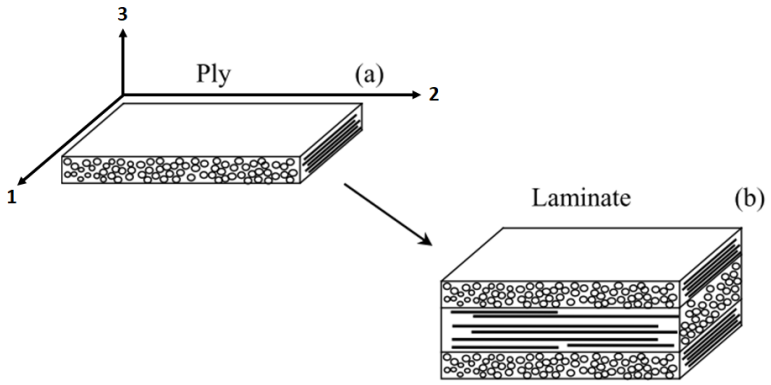

Figure 1.1: Ply and laminate

This means that the performance of CFRPs is often limited by delamination. Interlaminar delamination is the first failure mode which leads to a clear decrease in performance, in which layers are separated by fracture of the matrix material and/or the fiber-matrix interface as shown in Figure 1.2. Loads applied to the material can cause the polymer matrix to fracture or the matrix can debond from the fiber reinforcement. Delamination can initiate due to imperfections during the manufacturing process or due to effects of external factors during the working life, e.g. impact damage, by which transverse cracks can grow into delamination [1].

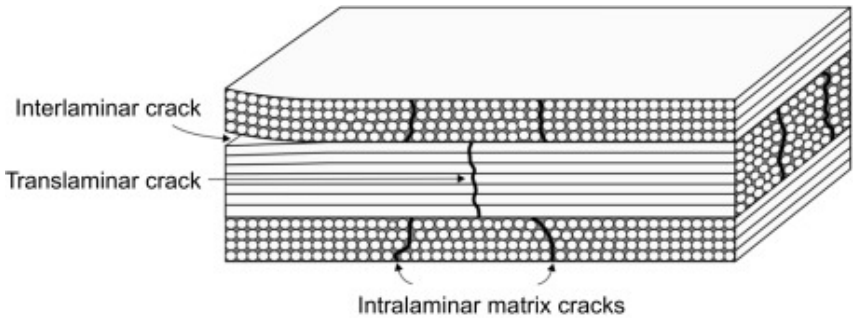

Figure 1.2: Typical composite fracture, with an illustration of interlaminar crack, or delamination [2]

Delamination particularly occurs under compressive, buckling load caused by cyclic loading. The resulting out-of-plane stress, which causes delamination, often occurs at many types of structural design features such as ply drops, skin-stiffener intersection, sandwich panels, on the free edge and the edges near geometric discontinuities such as holes, cutouts, flanges, stiffener terminations, bonded and bolted joints. Initiation of delamination can also be caused by contaminated fibers during manufacturing, insufficient wetting of fibers, curing shrinkage and out-of-plane impact [3]. Under fatigue load, the onset of cracks can grow and lead to a gradual decrease in the properties of the structure. Delamination has an impact on the capacity of the laminate to transfer load and can therefore have severe consequences. Hence, it is necessary to characterise the fracture of composite laminates under fatigue loading, before composites can be used in structural parts. Examples of structural parts of interest are, wind turbine blades, ship hulls, automotive structures, and structures in aerospace applications [4].

The double-cantilever beam (DCB) test is a common method used to evaluate the interlaminar fracture toughness of composite materials. The specimen can undergo either quasi-static loading or cyclic loading to expose it to fatigue conditions. The DCB test is a widely accepted standard test method that has been used in the aerospace and automotive industries for decades. For the quasi-static test, standards exist: ISO15024 [5] & ASTM D5528 [6]. For assessing fatigue loading, the ASTM D6115 [7] standard provides guidelines for analyzing the onset of fatigue delamination in composite materials. However, it does not address the propagation of fatigue delamination, which is a critical aspect of understanding material behaviour under fatigue loading conditions. Alderliesten et al. [8] proposed a specific protocol for this type of analysis, offering a framework for researchers to accurately assess the fatigue behaviour of composite materials. The thorough testing of a protocol using a Round Robin test is critical to ensure its reliability, reproducibility, and validity in various environments and conditions. The primary objective of a Round Robin test is to gather data from different laboratories. This approach helps to identify any potential ambiguities in the protocol and ensures the consistency of the test results. The results from the labs are compared to benchmark performance, allowing for the refinement and enhancement of the protocol towards creating a robust and effective standard. However, the current method of measurement described in the protocol tends to be time-consuming and labour-intensive. Additionally, it is susceptible to errors or biases, which may arise due to differences in the operators' techniques and the tools used.

The resistance to delamination of a material can be characterized by fracture toughness. The double-cantilever beam (DCB) test is a common method used to evaluate the interlaminar fracture toughness of composite materials. The laminate is loaded in the normal direction of the plane, by which a crack is initiated and propagated through the specimen. The initial delamination is made using a starter film, which is placed between 2 layers of the laminate. This type of loading is called mode I (Figure 1.3a). There are 3 different modes of loading as can be seen

in figure 1.3.

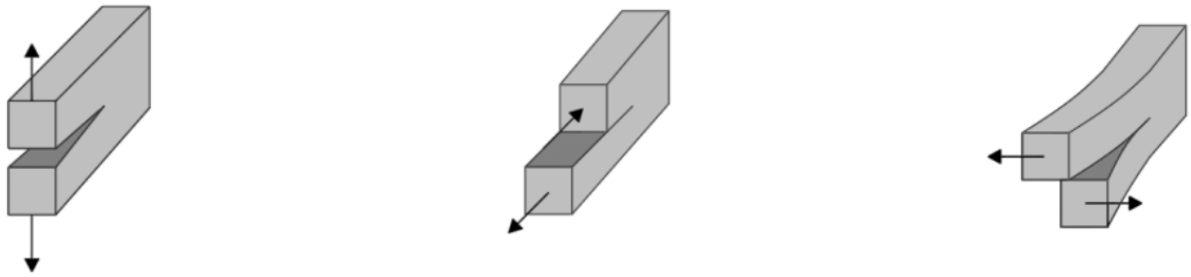

(a) Mode I (b) Mode II (c) Mode III

Figure 1.3: Loading modes [9]

It should be noted that since a multiplicity of possible delamination modes exist, the fatigue threshold for delamination growth is dependent upon the relative proportions of Mode I, II and III loading. Since mode I loading of composites is the most damaging mode, fatigue properties measured under Mode I may give the most conservative estimate of the life prediction of in-service components and structures [10]. To test the specimen under fatigue loading, a constant, cyclic displacement is applied to the specimen. When displacement, loading, and crack length are monitored, interlaminar fracture toughness and fatigue resistance can be obtained.

1.2 Objective, motivation & scope

The accuracy of measuring the crack length during a DCB test is critical for the accuracy of the characterisation of the subjected material. When this is not done properly, inaccurate material properties are obtained, which can lead to serious implications. According to the existing standards (ISO 15024 [5] & ASTM D5528 [6]) for quasi-static DCB-testing, measurement of crack length is done using a manually operated, travelling microscope. Another option is visual observation of the crack tip along a grid, marked on the side of the specimen. This way of measuring is prone to error because the operator must be very alert to sudden crack growth.

For Quasi-static testing, this means that the operator has to follow the crack and note crack lengths for a short period of time. For fatigue testing, on the other hand, testing may take up to several days, hence this is very time-consuming for an operator to monitor the test. An alternative is to film the test and post-analyse the crack advancement.

Alderliesten et al. [8] introduced a method for assessing crack length during fatigue tests by periodically interrupting the test at specific cycle intervals. Hence, the operator has to measure only when the machine is stopped, using a travelling microscope or camera footage. This way of measuring is still prone to human error. The primary aim of this assignment is to automate the measurement of crack length, with the dual objectives of reducing measurement errors and diminishing the requirement for operator intervention during testing.

This thesis presents the design and development of a setup meant to automate the crack length measurement during DCB fatigue testing of CFRPs under mode I conditions. The test has to be performed according to existing protocols and standards. By automating the crack length detection, the error made by manual measuring can be reduced. Also, no operator is needed to monitor the test during multiple days of testing.

The design and development of the automated crack length measurement setup involve several

stages, including system design, hardware selection, software development, and testing. The setup is evaluated using experimental tests to ensure its accuracy and reliability.

1.3 Project goal & objectives

In this section of the design report, the main goal and related objectives that have shaped the scope of this project are outlined. These objectives act as a guiding framework for the report. Later in the research, these goals and objectives will be revisited to assess the extent of progress achieved.

Main-goal:

Implement a protocol into the design of a setup capable of conducting DCB tests under fatigue conditions.

Objectives:

- *Minimise test and analysis duration by automating the crack length measurement process.*
- *Give argumentation for the choice of the specific technology used to perform the crack measurement, discussing its suitability for the intended application.*
- *Assess the precision and accuracy of the test setup by conducting test sequences on two different materials and comparing the results with existing data.*
- *Automate the control of the load ratio during testing to further minimize dependency on the operator.*

1.4 Report outline

The report is structured in the format of a design report and is divided into several parts. **Chapter 2** offers an overview of the relevant background theory. **Chapter 3** examines the existing testing protocol by Alderliesten et al. [8], breaking it down into functional requirements for the design. In **Chapter 4**, various solutions are proposed for each function and subsystem. **Chapter 5** provides a detailed description of the subsystems that comprise the final design. The precision and accuracy of the final design are assessed in **Chapter 6**, where measurement results are also presented and compared. **Chapter 7** provides feedback on the final setup and the data obtained. The report concludes with **Chapter 8**, which revisits the project goal and objectives outlined above. This final chapter brings together the key findings and insights from the research, leading to a set of conclusions and recommendations.

2 BACKGROUND AND RELEVANT THEORY

The Federal Aviation Administration (FAA) introduced in 2009 a so-called 'slow growth' approach to the certification of composites. This requires that in polymer-matrix fiber composites, delamination growth under cyclic-fatigue loading should be both slow and predictable. This approach caused attention to assess the growth of delaminations under fatigue loads. Especially on how to determine a 'valid' fatigue crack growth rate (FCG rate) in relation to the range of the energy release rate. With this relation, also known as fatigue resistance curves, eventually composite materials can be characterised and compared and composite structures can be designed [10].

2.1 Methods for the prediction of fatigue delamination growth

In their study, Pascoe and colleagues conducted a comprehensive review on fatigue-driven delamination growth prediction methods. Throughout their research, they identified four distinct categories, which are as follows [11]:

- stress/strain-based models
- fracture mechanics based models
- cohesive zone models
- finite element method models

The most common method of assessing the fatigue delamination resistance of fiber-reinforced plastics (FRPs) is the fracture mechanics approach [12]. Using this method, the dependence of the fatigue crack growth (FCG) rate on the applied energy release rate, G, is determined experimentally. Usually, these models are based on a sub-domain of linear elastic fracture mechanics (LEFM) [11].

2.1.1 Linear elastic fracture mechanics

Linear Elastic Fracture Mechanics (LEFM) is a way to describe the energy change a linear elastic body undergoes when the crack area of a sharp crack increases. It has the theoretical basis that all energy dissipation is associated with the fracture growth and the deformation that occurs is linear elastic. It is important to note that this theory encloses the growth of an already existing crack and hence nothing is said about the presence of a crack.

The most important parameter in LEFM is the energy release rate, G. This parameter is defined as the rate of energy that is released by the growth of a crack. In 1956, Irwin proposed this method of solving engineering problems of fracture, which is essentially equivalent to the Griffith model. The definition of the energy release rate is defined by equation 2.1

$$G = -\frac{d\Pi}{dA} \tag{2.1}$$

In which Π is the potential energy of an elastic body and A is the crack area. It should be noted that the term 'rate' used in 'energy release rate' does not refer to a derivative with respect to time. In this case, G is the rate of change in potential energy with crack area, therefore G could also be referred to as 'crack extension force' or 'crack driving force'. The potential energy of an elastic body is defined as follows:

$$\Pi = U - F \tag{2.2}$$

Where the strain energy stored in the body is indicated with U and F is the work done by external forces. First, a cracked plate is considered under plane stress conditions. The plate is 'load controlled' as illustrated in Figure 2.1.

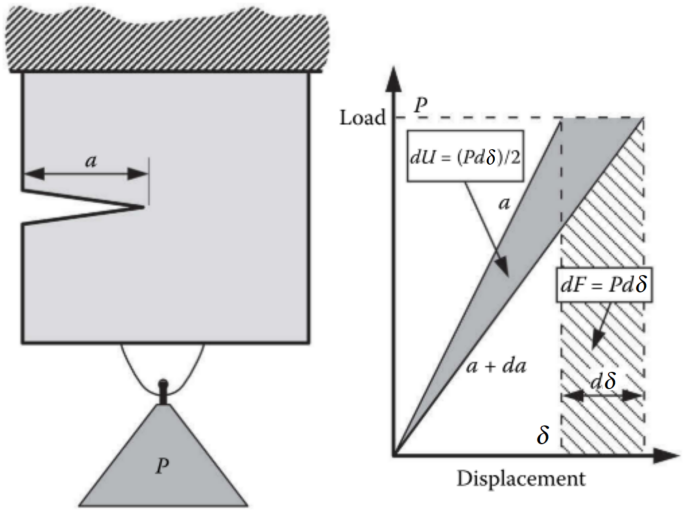

Figure 2.1: Load controlled cracked plate [13]

For this case, it holds that:

$$F = P\delta \tag{2.3}$$

and

$$U = \int_0^{\delta} P d\delta = \frac{P\delta}{2} \tag{2.4}$$

Therefore, it holds for the load-controlled situation:

$$\Pi = -U \tag{2.5}$$

This boils down to the following expression for the energy release rate for a load-controlled test:

$$G = \frac{1}{B}\left(\frac{dU}{da}\right)_P = \frac{P}{2B}\left(\frac{d\delta}{da}\right)_P \tag{2.6}$$

where B is the thickness of the plate. The same can be done for a displacement-controlled test. This is illustrated in Figure 2.3.

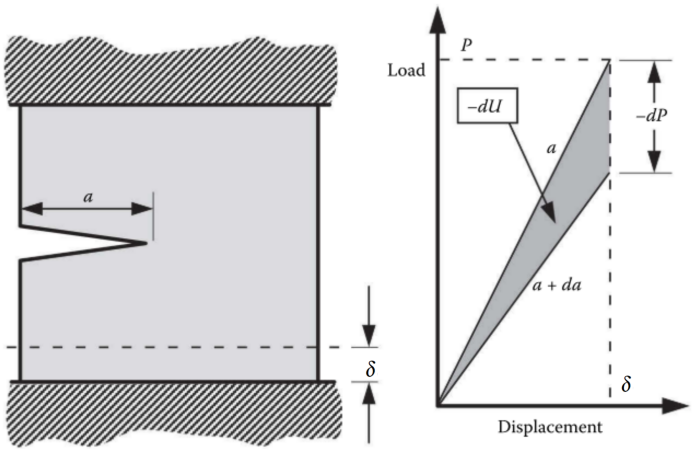

Figure 2.2: Displacement controlled cracked plate [13]

Now $F = 0$ and therefore $\Pi = U$. The following relation is obtained:

$$G = -\frac{1}{B}\left(\frac{dU}{da}\right)_{\delta} = -\frac{\delta}{2B}\left(\frac{dP}{da}\right)_{\delta} \tag{2.7}$$

For convenience, compliance can be introduced at this point. which is defined by:

$$C = \frac{\delta}{P} \tag{2.8}$$

By substituting the compliance in Equation 2.6 and 2.7, the following equation is obtained for G for both load and displacement control:

$$G = \frac{P^2}{2B}\frac{dC}{da} \tag{2.9}$$

As graphically illustrated in Figure 2.1 and 2.3, the following relation exists:

$$\left(\frac{dU}{da}\right)_{P} = -\left(\frac{dU}{da}\right)_{\delta} \tag{2.10}$$

In a load-controlled test, a crack extension, da, results in a net increase in strain energy. For a displacement-controlled test, the strain energy decreases as $dF = 0$:

$$(dU)_p = Pd\delta - \frac{Pd\delta}{2} = \frac{Pd\delta}{2} \tag{2.11}$$

$$(dU)_{\delta} = \frac{dP\delta}{2} \tag{2.12}$$

The absolute values of both energies differ by the amount $dPd\delta/2$, as can be seen in Figures 2.1 and 2.3. This value is negligible and thus, for an increment of crack growth at a given P and δ, holds:

$$(dU)_P = -(dU)_{\delta} \tag{2.13}$$

Using this approach, the strain energy release rate can also be determined for a DCB specimen using beam theory.

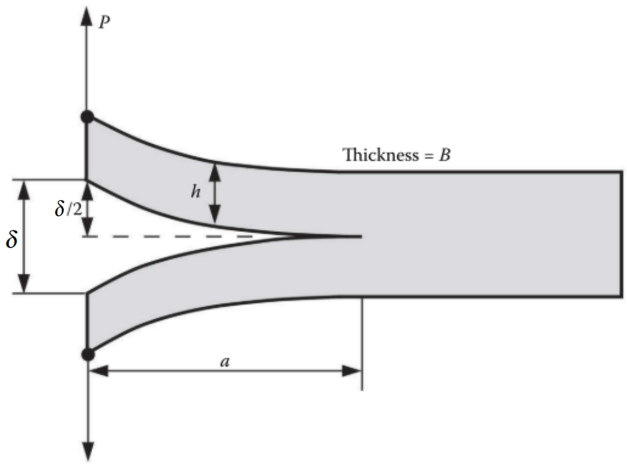

Figure 2.3: DCB specimens and dimensions [13]

$$\frac{\delta}{2} = \frac{Pa^3}{3EI} \tag{2.14}$$

in which:

$$I = \frac{Bh^3}{12} \tag{2.15}$$

and

$$C = \frac{\delta}{P} = \frac{2a^3}{3EI} \tag{2.16}$$

When C is substituted into Equation 2.9, the relation for G of a DCB specimen is obtained using Irwin's energy approach[13]:

$$G = \frac{P^2a^2}{BEI} = \frac{12P^2a^2}{B^2h^3E} \tag{2.17}$$

2.1.2 Fracture mechanics prediction models

For the last decades, fatigue crack growth has drawn a lot of attention. A large number of papers have been published to develop prediction models for this phenomenon. Methods based on fracture mechanics concepts of stress intensity factor (SIF) K and strain energy release rate ($SERR$) G are widely used to investigate the crack growth mechanism. The use of fracture mechanics in the prediction models is derived from the success of Paris and colleagues in predicting fatigue crack growth in metals [11]. An overview of these early findings by Paris is given by Jones et al. [14]. In the next section, the Paris relation is explained.

2.1.3 Paris relation

The concept of SIF is often used in fracture mechanics to create prediction models to describe the quasi-static crack growth as well as the crack growth under fatigue loading. The SIF is used to determine the stress field around a crack tip. Paris first found a relation between the SIF and the rate of fatigue crack growth, da/dN, in metals. Hence, the crack growth could now be determined by calculating the SIF using the basic form of the Paris relations, which are given by equation (2.18).

$$\frac{da}{dN} = C(\Delta K)^n$$
$$\frac{da}{dN} = C\,(K_{max})^n \tag{2.18}$$

To determine the Paris relation for composite materials, more often the $SERR$ is used instead of the SIF. This preference arises due to the intricate nature of calculating the SIF around the crack tip in anisotropic materials. As a result, the Paris relations based on the $SERR$, or G, are commonly employed to analyze fatigue delamination growth in composite materials or adhesively bonded structures. The fundamental forms of this relation are expressed by equation (2.19). It should be noted that these two parameters are equivalent and using either one does not provide more or different information as the SIF and the $SERR$ are related by the Young's modulus [11]. The $SERR$ can be used in the form of ΔG or G_{max}.

$$\frac{da}{dN} = C(\Delta G)^n$$
$$\frac{da}{dN} = C\,(G_{max})^n \tag{2.19}$$

The equations utilized to describe delamination growth in composites are based on equations used to model crack growth in metals. Paris et al. initially proposed in 1961 that the rate of crack growth per cycle, da/dN, could be correlated with ΔK and/or the maximum stress intensity factor K_{max} as described in Equation 2.18. Subsequently, Forman et al. expanded the Paris equation to accommodate K_{max} approaching its fracture toughness K_c. Hartman and Schijve suggested in 1970 that da/dN should be dependent on the amount by which ΔK exceeds the fatigue threshold ΔK_{th}, i.e. da/dN depends on $\Delta K - \Delta K_{th}$ [14]. However, tests conducted in the 1990s using composite/aluminium laminates revealed different da/dN versus G_{max} curves depending on the different residual stresses that were present in the laminates [15]. Also, Murri showed in his study the scatter that was obtained in FCG rates for composites [16]. In this study, 39 DCB specimens were tested of which the da/dN versus G_{max} curves were analysed. The material of these specimens where IM7/8552 CFRP. Subsequent studies indicated that relating da/dN to either G_{max} or ΔG is indeed erroneous [17, 18]. Later it was found that the logical extension of Paris' FCG law for metals to delamination growth in composites is to express da/dN as a function of $\sqrt{G_{max}}$ or $\Delta\sqrt{G}$, where $\Delta\sqrt{G}$ is defined as $\sqrt{G_{max}} - \sqrt{G_{min}}$, with G_{min} representing the minimum value of the energy release rate in a cycle of fatigue loading [10, 14, 17, 19, 20]. However, the scatter obtained in the measured test data of Murri [16], remained. Jones et al showed subsequently that for tests on both IM977-3 and IM7/8552, the scatter could be captured by the Hartman-Schijve variant of the Nasgro equation [10]. After which, for each material, the various curves now all fell onto a single, linear, 'master' relation when the FCG rate is plotted versus a function of the energy release rate.

During DCB testing in Mode I, retardation of crack growth occurs as the delamination grows. The retardation occurring can be attributed to the fiber-bridging that typically occurs behind the advancing crack tip. However, to characterise and compare composite materials and to determine design allowables for the specific material, test data should exhibit no, or only very minimal retardation. In the research of Jones et al., a way to determine test data in which no or little retardation is present is described by using a variant of the Hartman-Schijve approach. This way of data reduction also takes into account the typical scatter that arises during experimental work. Hence, using this methodology, a valid, upper-bound FCG-rate curve can be obtained to determine design and lifing allowables [10]. In the next section, Fiber bridging is explained. Later in this chapter is shown how the 'upper-bound' curve is obtained and how design allowables can be determined.

2.2 Fiber bridging

Fiber bridging is an important mechanism during delamination growth in composite laminates. In this phenomenon, intact fibers span across the faces of a crack. When a crack propagates, not all fibers at the crack plane break. Some fibers stay intact and stretch across the crack, effectively 'bridging' the gap. In Figure 2.4 fiber bridging can be seen. Due to the bridging fibers, the fracture toughness can increase by restraining the crack opening and hence inhibit the growth of delamination. Fiber bridging occurs both under quasi-static and fatigue loading. [21]

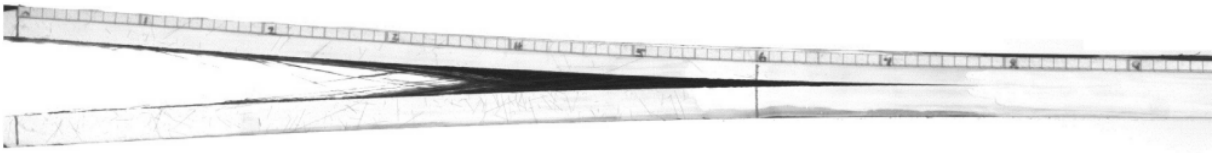

Figure 2.4: Bridging fibers in a DCB specimen in fatigue delamination growth [22]

On the other hand, fatigue tests on composite components of aircraft parts showed no, or little, retardation of the fatigue crack growth (FCG) rate as delamination/impact damage grows. This leads to a major difference in measured values during a DCB test, in which extensive fiber-bridging occurs, which leads to significant retardation of the FCG rate [12]. In both ISO 15024 [5] and ASTM D6115-97 [7] is stated that fiber bridging is an artefact of the DCB testing method and hence does not reflect how lead delaminations, i.e. the fastest growing delaminations in which no or little retardation occurs, behave. The behaviour of a lead delamination would determine the life of a composite structure. Hence, the challenge is to develop tools that are able to determine the 'retardation-free' fatigue behaviour of a material in the form of a da/dN versus $\Delta\sqrt{G}$ or $\sqrt{G_{max}}$ curve, which exhibits the fastest possible growth rate [10]. Yao proposed a concept of fatigue fracture toughness analysis to describe the steady fatigue delamination growth, in which little or no fiber bridging occurs [21]. In this way, all energy dissipation in the growth of steady delamination is concentrated on the new crack generation.

2.2.1 Fiber bridging during quasi-static testing

During quasi-static delamination, the interlaminar fracture toughness (IFT) experiences a gradual increase from an initial low value until it reaches a plateau value as the crack extends. This phenomenon is attributed to the presence of fiber bridging. As the crack propagates, the bridging fibers actively reduce the Stress Intensity Factor (SIF), leading to the establishment of a plateau. This plateau signifies that at a specific delamination length, fiber bridging has reached its full development and stabilizes as further delamination occurs [21]. This phenomenon has led several researchers to express the apparent toughness, G_{CR}, as a function of the delamination length [10]. This is done using the following expression:

$$\begin{aligned} \mathrm{G_{CR}} &= \mathrm{G_{C0}} + \mathrm{B}\,(\mathrm{a} - \mathrm{a_0}) \quad && \text{for } \mathrm{a} < \mathrm{a_s} \\ &= \mathrm{G_{RSS}} && \text{for } \mathrm{a} > \mathrm{a_s} \end{aligned} \tag{2.20}$$

Since this expression is valid for Mode I, the subscript 'I' is omitted for clarity. In this expression, a_0 is the initial delamination length, i.e. the length of the insert film, G_{C0} is the initiation value at which the onset of crack growth occurs, B is a constant, G_{RSS} is the steady state value of G_{CR} and a_s is the delamination length at which this asymptotic value is achieved. During quasi-static testing, first, a pre-crack is made to obtain a sharp crack tip before the actual test is started.

This is done to avoid the test starting from the relatively blunt insert film, which typically has a polymer-matrix-rich region in front of it. However, this procedure may already lead to over-estimation of the value of G_{IC0} due to fiber bridging. Hence, the pre-crack should be neither too long nor too short, as is also stated in ISO15024 [5].

2.2.2 Fiber bridging during fatigue testing

Yao et al. tested a few specimens under fatigue loading with a load ratio of $R = 0.1$ and 0.5 [12]. The stress ratio is defined as the ratio between the maximum and minimum force of a fatigue loading cycle. Since the cyclic loading is displacement-controlled, the crack will eventually stop growing or at least reach a very low FCG rate. A new test sequence can be started by increasing the displacement values and continuing the cyclic loading with these higher displacement values. In this way, more fatigue resistance curves can be obtained from one test specimen. When the crack resistance curves were plotted, it was evident that bridging had a significant influence on these curves. The $\Delta\sqrt{G}$ was plotted over the crack growth rate, da/dN, see Figure 2.5. The longer the crack length, the further the curves shift from left to right. Hence, at a given $\Delta\sqrt{G}$, the crack growth rate is lower in a longer crack, compared to the crack growth rate in a short crack. Hence, because of the longer crack length, more bridging fibers will be present behind the crack tip.

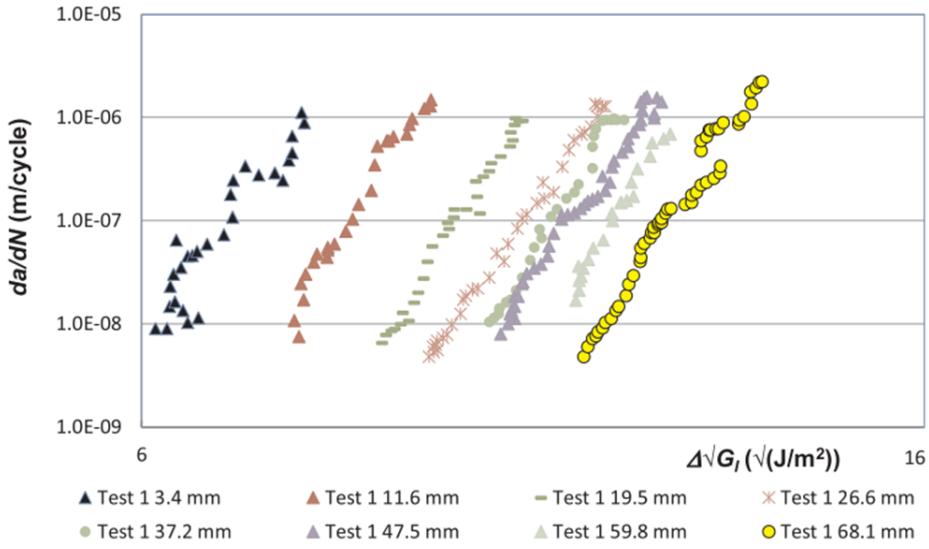

Figure 2.5: Fatigue resistance curves with different pre-crack lengths [12]

2.2.3 Effect of the pre-crack length on the test data

In Figure 2.5, the fatigue resistance curves of tests of Yao et al. are shown. The material for this test is unidirectional C-Epoxy prepreg of M30CS/DT120. As depicted by Figure 2.5, with the increase of pre-crack length, $(a_p - a_0)$, where a_p is the delamination length after pre-cracking and a_0 is the delamination length created by an insert within the laminate, the resistance curves shift to the right and converge to a single curve at the right of the graph. This curve shifting reflects the retardation on the FCG rate due to more extensive fiber bridging once the pre-crack length is increased.

2.2.4 Effect of the thickness of the CFRP specimens on the test data

In several studies [12, 19], the effect of specimen thickness on the fatigue behaviour is tested. For all the thicknesses tested, the same phenomenon of the shifting fatigue resistance curves

was observed due to fiber bridging as the value of $a_p - a_0$ increased. However, it was observed that the thickness of the specimen had no significant effect on the position of these curves.

2.2.5 Effect of the R-ratio on the test data

In the paper of Yao et al. [12], the influence of the R-ratio (load ratio) on the fatigue resistance curves is tested. Again, the curves shifted to the right of the plot due to retardation of the FCG rate as the value of $a_p - a_0$ increased. It was observed that the fatigue resistance of the composite is inferior if a higher R-ratio was applied, resulting in fatigue resistance curves starting more on the left of the graph. Hence, the crack subjected to a higher R-ratio grows at a faster rate, or put another way, when a higher R-ratio is applied, a higher value of da/dN is recorded for a given value of $\Delta\sqrt{G}$.

2.2.6 Effect of the layup on the test data

Yao et al. also looked into the influence of the lay-up orientation on fatigue delamination growth. for this study, multidirectional DCB specimens were manufactured with a lay-up sequence of $[(\pm 45/0_{12}/\mp 45)//(\pm 45/0_{12}/\mp 45)]$. When pre-crack length is short, there appears to be no significant difference between the multidirectional and the unidirectional specimens in the fatigue resistance curves. However, at the longer pre-crack lengths, the multidirectional showed more fiber-bridging. Hence, fiber bridging develops more rapidly and is more extensive in multidirectional specimens, resulting in a fatigue resistance curve shifting more to the right [12].

2.3 'Upper-bound' FCG curve

2.3.1 Introduction

Previous studies on real components and structures showed that no, or only little retardation occurs in the lead delaminations that arise in components with mis-drilled holes, ply drop-offs, impact damage, and manufacturing defects, etc. under fatigue loading [10]. in Mode I DCB testing, on the other hand, the retardation of the FCG arising from fiber bridging is invariably observed and cannot readily be prevented. Another problem that arises during tests is the relatively large inherent scatter that is observed. Scatter may arise due to, for example, variability in the material and manufacturing process, which leads to variability in the specimens. Another cause of scatter is experimental difficulties that occur when accurately measuring the crack tip location and/or the relatively low loads and displacements, especially when the FCG rate approaches the relatively low threshold value.

It is necessary to find a way to determine a delamination FCG curve that represents the fastest possible growth, i.e. which is free of retardation effects and which assesses the scatter that is observed with testing. However, experimental data reveals that retardation effects and a relatively high degree of inherent scatter cannot be easily avoided. Therefore, a methodology is needed to estimate an 'upper-bound' curve from the obtained DCB test data, such that it encompasses all previously obtained data and its scatter and provides a conservative FCG curve which accounts for retardation effects. This 'upper-bound' FCG curve can later be employed to develop, characterize, and compare different composite materials and also for designing and lifing in-service components using a 'slow growth' approach, as required by the FAA [10].

In Section 2.1.3, it was explained that delamination growth in composites was usually expressed as the increment in the energy release rate per cycle, ΔG, or the maximum value of the energy release rate in a cycle, G_{max}. Expressing the FCG curves in this way led to anomalous behaviour, namely, for a given ΔG, increasing the mean stress level reduces the FCG rate. Later, this is resolved by the logical extension of Paris' growth law to composites by expressing da/dN as

a function of $\sqrt{G_{max}}$ or $\Delta\sqrt{G}$. However, this formulation did not account for the retardation of the FCG rate and the large scatter obtained in the DCB testing data. To take care of these challenges, Jones et al. came up with a way to express da/dN with the Hartman-Schijve variant of the Nasgro equation [10].

2.3.2 The Hartman-Schijve approach

The ΔK, which is used for metals, in the Nasgro equation can be replaced by $\Delta\sqrt{G}$ because both terms are equivalent. When this is done, the Hartman-Schijve variant of the Nasgro equation is obtained:

$$\frac{da}{dN} = D\left[\frac{\Delta\sqrt{G} - \Delta\sqrt{G_{thr}}}{\sqrt{\left\{1 - \sqrt{G_{\max}}/\sqrt{A}\right\}}}\right]^n \tag{2.21}$$

where D, n and A are constants. The value of A can be either taken as the quasi-static value of the fracture energy, G_c, or fitted to the data. The term $\Delta\sqrt{G_{thr}}$ is the fatigue threshold, this is the value below which no significant FCG occurs. The term $\Delta\sqrt{G_{thr}}$ is defined by:

$$\Delta\sqrt{G_{thr}} = \sqrt{G_{thr_{max}}} - \sqrt{G_{thr_{min}}} \tag{2.22}$$

The value of $\Delta\sqrt{G_{thr}}$ can be determined by fitting equation 2.21 over the entire data. To achieve this, the measured experimental data may be replotted according to the Hartman-Schijve Equation (2.21) such that a single, linear, 'master' is obtained as shown in the recent work of Jones et al. [10] and Yao et al. [12]. The next step is to obtain a valid 'upper-bound' curve using this 'master' relationship. Using this 'upper-bound', i.e. 'worst case', FCG rate should exclude any retardation effects on the FCG rate and should take into account the inherent scatter observed in the DCB Mode I fatigue tests.

Jones and Kinloch recently presented a simple methodology to obtain the upper bound curve [23]. This methodology is shortly explained in this report. First, the master relationship has to be obtained. To do this, the data obtained by Yao et al. [12, 21, 22, 24–29] is used. This test data is from the 'M30SC/DT120' CFRP composite material specimens. To achieve a single, linear, 'master' relationship, a value of the fatigue threshold, $\Delta\sqrt{G_{thr}}$, and the values of the other constants, A, D and n are chosen with the lowest coefficient of determination, R^2 [23]. When this is done in the right way, the single, linear, 'master' relationship is obtained as illustrated in Figure 2.6. The linear relationship has a R^2 of 0.994 and a slope, n, of about two.

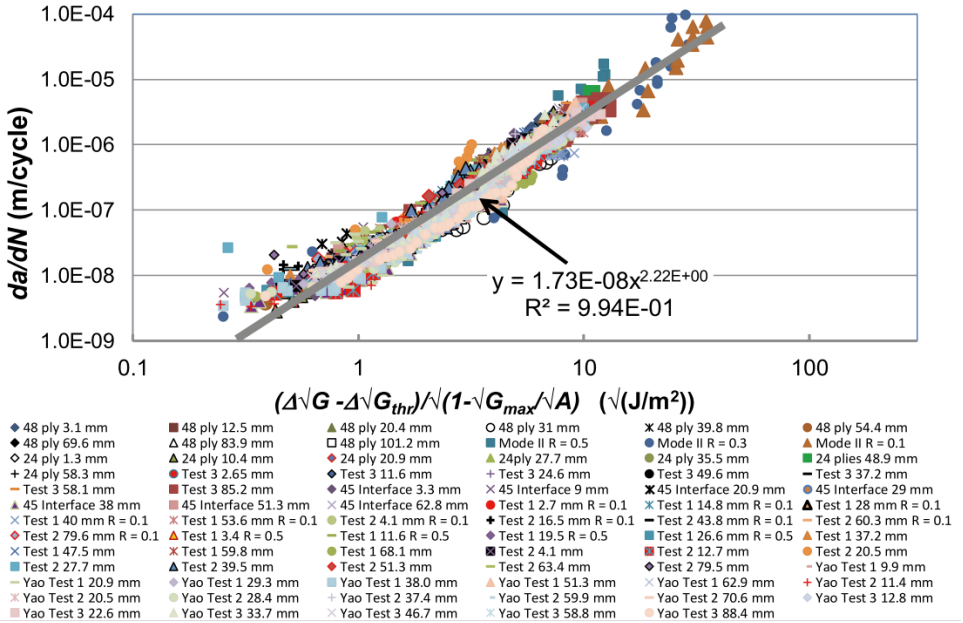

Figure 2.6: Single, linear, 'master' relation [23]

From the 'master' curve, a mean value of $\Delta\sqrt{G_{thr}}$ of $8.40\sqrt{(J/m^2)}$ is obtained with a standard deviation (sd) of $1.9\sqrt{(J/m^2)}$ as described by Yao et al. and Jones and Kinloch [12, 23]. The value of the constant, A, is taken to be equivalent to the quasi-static value of the Mode I initiation fracture energy, G_{c0}, for the material M30SC/DT120 CFRP, which has the value of $250 \pm 45 J/m^2$. Next, the number of standard deviations whereby the mean of both the terms $\Delta\sqrt{G_{thr}}$ and G_{c0} are reduced to obtain the 'upper-bound' curve needs to be considered. This can be either two or three standard deviations, depending on how demanding the intended application of the design is for a more conservative 'upper-bound' FCG rate curve. For equation 2.21, the values of D and n were found to be $1.73 * 10^{-8}$ and 2.22 respectively, using units for the y- and x-axis, see Figure 2.6. Now, all the parameters needed to calculate the 'upper-bound' curve are known, shown in Table 2.1.

Table 2.1: Parameters found to determine the 'upper-bound' curve

$\Delta\sqrt{G_{thr}}$ $\sqrt{J/m^2}$	$\Delta\sqrt{G_{thr}}$ sd $\sqrt{J/m^2}$	G_{c0} J/m^2	G_{c0} sd J/m^2	D	n
8.4	± 1.9	250	± 45	$1.73 * 10^{-8}$	2.22

In Figure 2.7, the 'upper-bound' curves for both a standard deviation of two ('means-2sd') and three ('mean-3sd') for $\Delta\sqrt{G_{thr}}$ and G_{c0} are shown. As can be seen in this Figure, both of these curves encompass and bound all the experimental data.

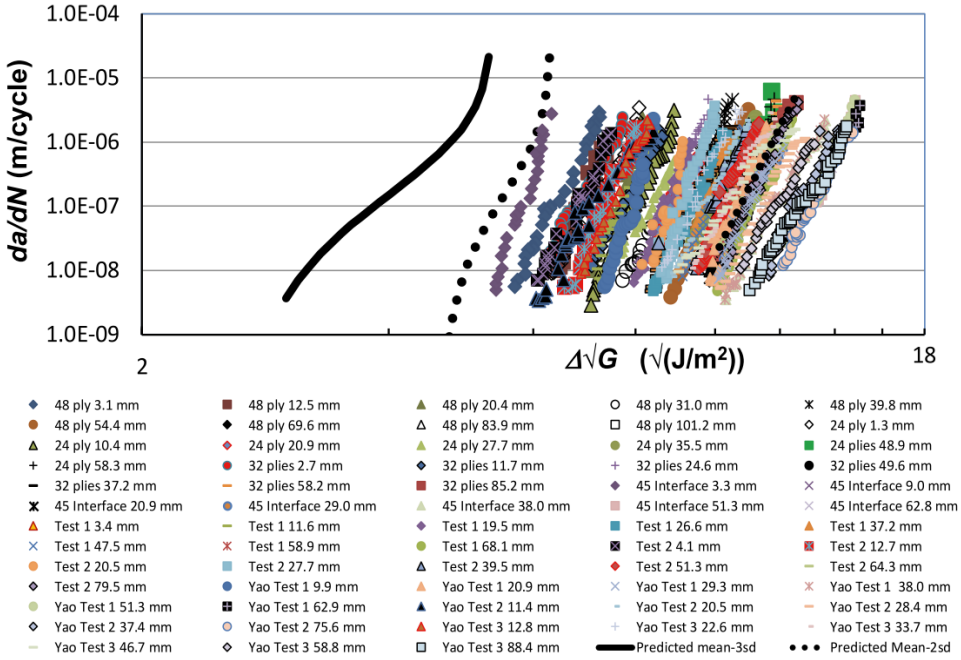

Figure 2.7: 'Upper-bound' curve [23]

This curve can be finally be used, with confidence, for material development, characterisation and comparison studies, and design and lifing studies.

2.4 Calculation of strain energy release rate

In this section, it is explained how the energy release rate is calculated for a DCB Specimen. In Section 2.1.1, a simplified LEFM version was shown to understand the definition of G, now the more in-depth definition is given to be able to calculate the energy release rate for the tests as described in ISO15024 [5]. The Energy release rate for Mode I, G_I, can be calculated in 3 different ways, following from Irwin's energy approach (Equation 2.9) [19]. The simplest method is called SBT method (Simple Beam Theory), The second method is the CBT method (Corrected Beam Theory) and the last one is the MCC-method (Modified Compliance Calibration) shown in Equation 2.23. The MCC method is used during this project, the other methods are explained in Appendix C. The Equation for the MCC method is:

$$G_I = \frac{3m}{2(2h)} \left(\frac{P}{B}\right)^2 \left(\frac{BC}{N}\right)^{2/3} F \tag{2.23}$$

in which m is the slope of the linear fit of $(BC/N)^{1/3}$ over $(a/2h)$ and F and N are a large displacement correction factor and a load-block correction factor respectively. The correction factors can be calculated by Equation 2.24 and 2.25

$$F = 1 - \frac{3}{10}\left(\frac{\delta}{a}\right)^2 - \frac{2}{3}\left(\frac{\delta l_1}{a^2}\right) \tag{2.24}$$

$$N = 1 - \left(\frac{l_2}{a}\right)^3 - \frac{9}{8}\left[1 - \left(\frac{l_2}{a}\right)^2\right]\frac{\delta l_1}{a^2} - \frac{9}{35}\left(\frac{\delta}{a}\right)^2 \tag{2.25}$$

where l_1 is the distance from the centre of the loading pin to the mid-plane of the specimen and l_2 is the distance from the loading pin centre to the edge of the load block as depicted in Figure 2.8.

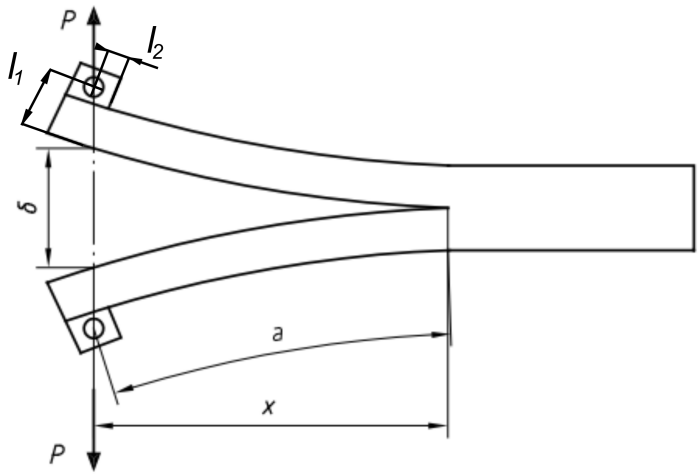

Figure 2.8: Delamination length measured along horizontal direction, x, and along the curved coordinate scale, a [5]

It is important to note that when delamination is measured alongside x in the horizontal direction, as shown in figure 2.8, delamination length x may be used instead of a. In this specific case, the large-displacement correction factor F is equal to 1, as described in ISO15024 [5]. However, when load blocks are used, the correction factor, N, still has to be calculated according to equation 2.25.

3 FUNCTIONAL BREAKDOWN

In this chapter, the protocol for the DCB fatigue test proposed by Alderliesten et al. [8] is thoroughly analysed. This protocol provides a detailed, step-by-step guide on conducting a DCB fatigue test. Following the analysis, the protocol is broken down into specific functions and requirements, which are essential for designing the automated test setup.

3.1 Protocol

This protocol specifies a method for the determination of delamination propagation curves as a function of the applied mode I strain energy release rate G_I for unidirectional fiber-reinforced plastic composites using the DCB (Double Cantilever Beam) specimen and test setup for fatigue loading. This method is described especially for UD (unidirectional) carbon-fiber and glass-fiber-reinforced thermoplastics and thermosets, which also holds for the quasi-static standards from ISO [5] and ASTM [6]. The test described in this protocol is performed under constant amplitude, cyclic displacement at constant frequency. A copy of this protocol can be found in Appendix A.

3.1.1 Apparatus

In the context of testing apparatus required, it is imperative that the machine adheres to a set of requirements. Firstly, the machine should be compliant with ISO5893 [30], which serves as a benchmark for its operational and measurement accuracy capabilities. For measuring the load during the tests, a calibrated load cell should be used. This load cell is required to have a maximum permissible error of $\pm 1\%$ of the indicated value. An analogous level of precision is required for the measurement of displacement, where the error in displacement measurement should not be greater than $\pm 1\%$ of the indicated value. The next section will provide a more detailed list of the requirements obtained from the protocol.

3.1.2 Test specimen

The specimens are made according to ISO15024 [5]. This standard makes use of specimens with load blocks (Figure 3.1a) or piano hinges (Figure 3.1b). It requires the insertion of a thin film (typically $13\mu m$) at mid-plane during lamination, leading to an initial crack length of a_0. Different from the ISO 15024 norm is the length of the insert between the plies of the specimen, such that the initial delamination length after pre-cracking is no more than $30mm$ from the load line instead of around $55mm$ for ISO15024. The load line is the vertical line between the centre of the holes in the load blocks at which the load is applied. For the piano hinges, the load line is the vertical line between the centre of the hinges. As can be seen in Figure 3.1, the delamination length, a, is measured from this line to the crack tip.

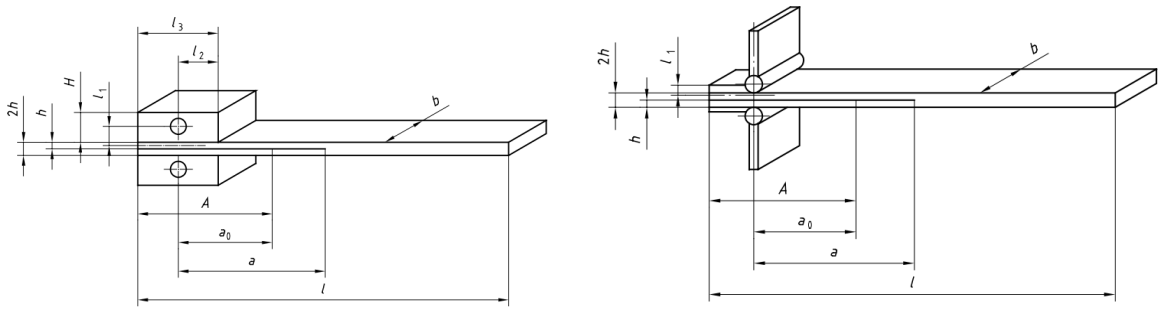

(a) Specimen with load blocks (b) Specimen with piano hinges

Figure 3.1: Different specimens [5]

The length of the specimen should be at least $200mm$, to be able to perform more test sequences on one specimen. The Protocol also states that the thickness of the specimen may be enhanced, compared to ISO15024, to decrease specimen compliance when this is needed. According to ISO15024, the thickness should be $3mm$ for carbon-fiber-reinforced composites and $5mm$ for glass-fiber-reinforced composites. The dimensions of the specimen should be checked according to ISO 15024, hence specimen width and specimen thickness should be measured at at least 3 evenly distributed points over the specimen length. To make the delamination length more visible, the side of the specimen could be coated with a brittle typewriter correction fluid.

3.1.3 Test procedure

This section provides a detailed visual and textual explanation of the testing procedure as outlined in the protocol of Alderliesten et al. [8]. Figure 3.2 presents a simplified flowchart of the testing procedure, while the comprehensive flowchart is available in Appendix B. The procedure is segmented into three primary phases: Test initialisation, Cyclic Loading, and Data Analysis. The specific steps within those three main phases are explained using a graphical representation in Figure 3.3.

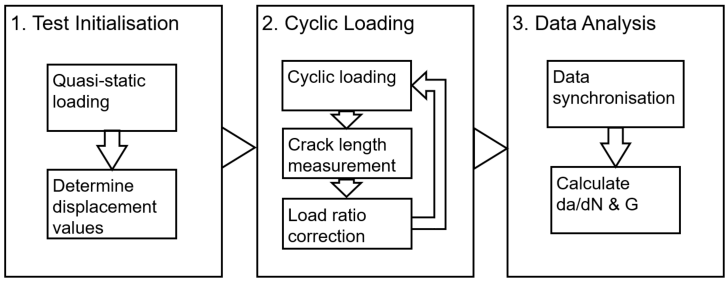

Figure 3.2: Simplified flowchart of the testing procedure for one testing sequence

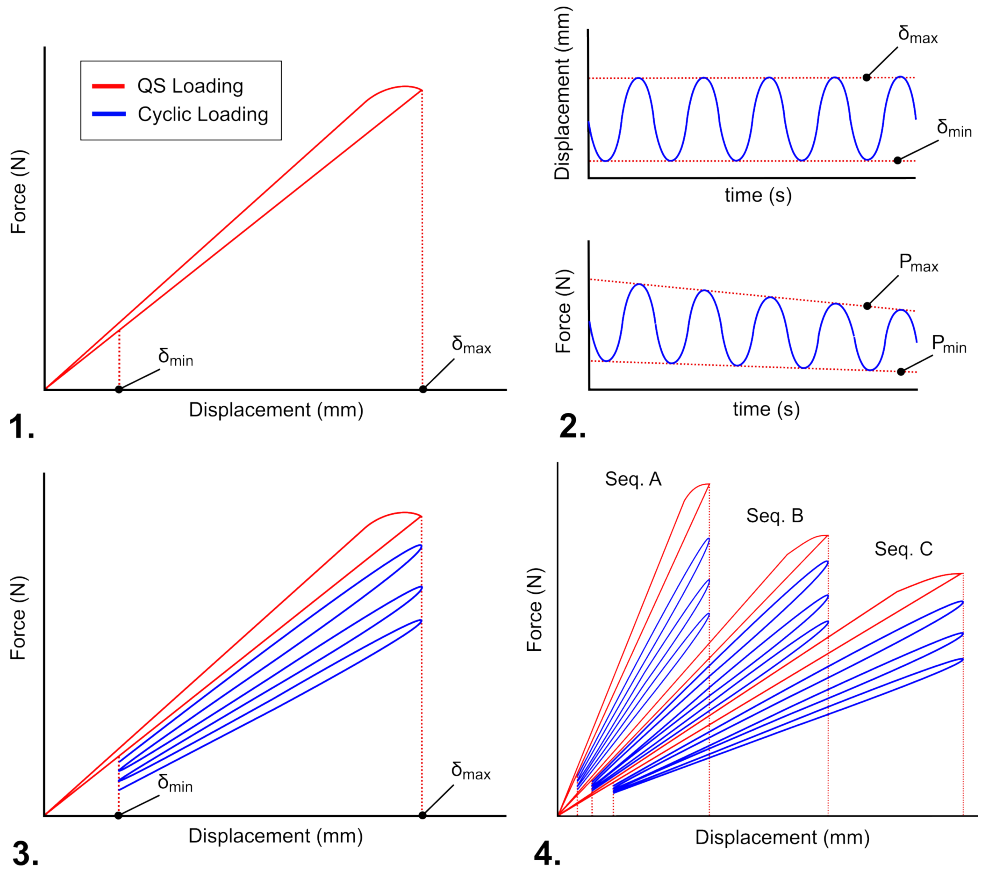

Figure 3.3: Force-displacement diagram of the test including 3 sequences

The first step is to create a natural crack tip and to determine the displacement values over which the fatigue test is performed. This is done using displacement-controlled, quasi-static loading in mode I, which is described in ISO 15024 [5]. The force-displacement curve of the quasi-static loading procedure is visualised in Figure 3.3.1. The loading is applied with a displacement rate of $1mm/min$ until crack propagation is observed, after which loading is stopped immediately, limiting the initial crack length to less than 3 mm. The displacement value at which loading is stopped is used as the maximum displacement for cyclic loading, δ_{max}. The force at δ_{max}, which is the maximum force of the loading cycle, P_{max}, is noted. Now, the specimen can be unloaded with a displacement rate of $5mm/min$. To determine δ_{min}, the desired load ratio is used, which is described by equation 3.1. When a load ratio of 0.1 is desired, the value of δ_{min} is obtained from the test data where a force is measured 10% of P_{max}. Now, both P_{min} and δ_{min} are also known.

$$R_P = P_{min}/P_{max} \tag{3.1}$$

With these values known, the cyclic loading can be started, which is shown as the blue lines in Figure 3.3. At predefined intervals of cycles, the cyclic loading is stopped and the delamination length is measured. As can be seen in Figure 3.3.2, due to crack growth, the forces, P_{max} and P_{min}, will decrease. To keep the load ratio constant (within 10%), the value of δ_{min} should be adapted during the cyclic test, while δ_{max} remains constant. The decrease in P_{max} and P_{min} is also observed in Figure 3.3.3. The test can now be continued until an FCG rate (Fatigue Crack Growth rate) of $10^{-8}m/cycle$ is reached. The FCG rate can be obtained using 2 methods. The

first method is the secant method described by Equation 3.2.

$$\frac{da}{dN} = \frac{a_{i+1} - a_i}{N_{i+1} - N_i} \tag{3.2}$$

However, if delamination length increments are small, this method gives significant scatter. The second method is to use the incremental polynomial method described in ASTM E647 [31]. In this method, a second-order polynomial is fitted through a number of obtained data points, by which consequently the average FCG rate can be determined using the tangential, i.e. derivative of the mid-point. Alderliesten suggests in his protocol to use 7 data points [8]. Since this method is not able to describe the FCG rates for the first and last pair of data points, as schematically shown in Figure 3.4, these rates have to be calculated using a polynomial fitted over 5 and 3 points. Subsequently, for the first and last two points, the secant method can be used to calculate the FCG rate. Once the threshold value of $10^{-8} m/cycle$ is measured, one sequence of the test is completed.

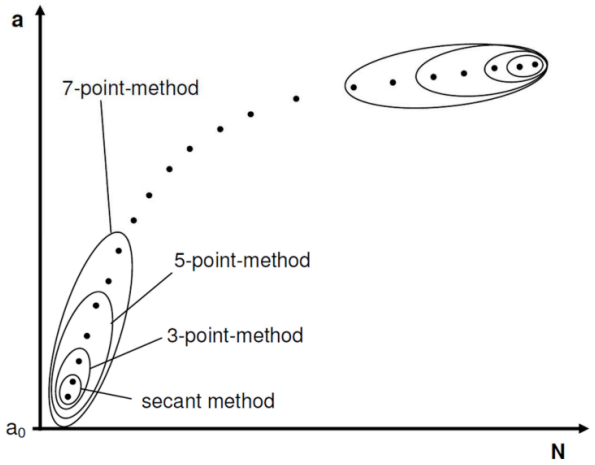

Figure 3.4: Schematic illustration of the determination of the FCG-rate using the incremental polynomial method [8]

To start a new sequence, the specimen is loaded quasi-statically again to determine new, higher, displacement values. The new δ_{max} is now obtained once nonlinearity is observed in the load-displacement curve, such that no or minimal delamination increment is obtained during test initialisation. The minimum displacement, δ_{min}, is obtained according to the chosen load ratio. The process of quasi-static and cyclic loading can be repeated until the load-line displacement becomes too high or when subsequent delamination resistance curves coincide with each other. The force-displacement diagram of three sequences is illustrated in Figure 3.3.4. Each step outlined in the protocol is represented in a block diagram, which is included in Appendix B.

3.1.4 Data acquisition

Throughout the testing sequence, pauses are implemented at predefined intervals for the purpose of data acquisition. This is done once every 100 cycles in the first 5000 cycles, once every 500 cycles for the following 15000 cycles, and finally, the measuring frequency can be lowered to at least once every 5000 cycles for the rest of the sequence. The measured data consists of:

- Delamination length, a.
- Minimum and maximum load, P_{min} and P_{max}.
- Minimum and maximum displacement, δ_{min} and δ_{max}.

- Number of cycles, N.

To measure the delamination length, two ways are suggested by the protocol. Either using an optical travelling microscope or using camera recordings. For the optical microscope holds that the magnification may not exceed 70x and the travel range must be at least 100 mm to capture several sequences on a specimen. The minimal readability must be 0.05 mm.

For the camera recordings, it is recommended that the camera and lighting position are fixed during the entire test, such that the entire delamination length is captured (100 mm) with a resolution that is able to measure 0.05 mm of delamination. When this is not achievable, the camera may be positioned closer to the specimen, such that at least one delamination length of one test sequence can be captured, i.e. a length of about 20 to 25 mm.

The load and displacement values can be taken directly from the testing machine or by using a separate extensometer, this should be done without stopping the test, though short stops at minimum and maximum load will have negligible effect on the test results.

3.2 Functions & requirements

According to the above-described protocol, the design of the test setup can be broken down into different functions:

Main function:

Automate fatigue DCB-test

Sub-functions:

- *Mechanical Loading*
- *Measuring Crack Length*
- *Test Control*
- *Data Analysis*

Each sub-function will be discussed in detail in the upcoming subsections. In the subsequent chapter, solutions will be proposed for each function and a singular concept will be selected for further development.

The requirements for the design, following from the protocol, are given per function. after each requirement, it is indicated if it is a Mandatory requirement, indicated with (M), a variable requirement, indicated with (V), or a Wish, indicated with (W).

3.2.1 Mechanical loading

The first function of the design is Mechanical Loading. The machine should be able to apply both quasi-static and cyclic loading to the specimen. A natural crack tip has to be created with quasi-static loading of the specimen. During this quasi-static loading, also the displacement values between which cyclic loading is performed have to be determined. After a natural, initial crack is created, a cyclic load is applied to the specimen. Due to this load, the crack in the specimen will propagate. The loading is displacement controlled, which means that the cyclic displacement amplitude should be constant for the first cycles. However, when the load ratio

deviates more than 10% from its desired value, δ_{min} should be adapted.

To transfer the load to the specimen, a specifically designed fixture is needed for the load blocks. It is important that the fixture allows the ends of the specimen to rotate freely to ensure the integrity of the test results. The fixture should also minimise friction and eliminate unnecessary play, thereby ensuring that the mechanical interaction between the fixture and the specimen does not introduce any additional variables that could influence the test results.

Requirements for mechanical loading:

- The machine is capable of applying cyclic displacements, of constant amplitude (which is reasonably large), at a constant frequency of $5Hz$. (M)
- Multiple sequences are performed per specimen. (M)
- The tensile testing machine complies with ISO5893 [30]. (M)
- The tensile testing machine is capable of maintaining constant amplitude and frequency, as specified in ISO5893 [30]. (M)
- Fixtures are used to introduce the load to the loading blocks or piano hinges, such that the specimen ends can rotate with minimal friction. (M)
- There is minimal play in the fixtures and the load blocks or piano hinges. (W)
- The load cell is calibrated and has a maximum permissible error of $\pm 1\%$ of the indicated value. (M)
- A load cell with a maximum capacity of $250N$ is used (or a load cell of higher capacity, calibrated to the maximum permissible error in the range up to $200N$). (M)
- The error in the displacement measurement is lower than $\pm 1\%$ of the indicated value. (M)
- The testing machine is capable of measuring the minimum and maximum loads and displacement for each cycle at the applied test frequency. (M)
- The testing machine is capable of performing a quasi-static loading rate of $1mm/min$ (and $5mm/min$ for unloading). (M)

3.2.2 Measuring crack length

During the test, the crack length has to be measured at specific intervals of cycles. When the desired number of cycles has elapsed, the machine is paused and a measurement is performed. There are also other ways of measuring the crack length without the need to pause the cyclic loading. Available options are described in the next chapter.

Requirements for crack length measurement:

- Delamination measurement is done either using an optical travelling microscope or camera recordings. (W)

  Microscope:

  - Magnification of the travelling microscope does not exceed 70x. (W)
  - The travel range of the microscope is at least $100mm$. (W)
  - The minimal measurable delamination length is $0.05mm$. (M)

Camera:

- The camera and lightning position are fixed throughout the entire test with multiple test sequences. (W)
- The entire delamination range of $100mm$ is in view. (W)
- The camera resolution must be sufficiently high to measure delamination up to $0.05mm$. (M)
- At least $20mm$, i.e. one sequence length, is in view (the camera may be placed closer to the specimen to improve image quality and to meet the level of accuracy). (M)

- Measuring delamination length should be done without stopping the test (short stops will have a negligible effect on the test). (W)
- Measurements are done at the recommended stop interval. (W)

3.2.3 Test control

Controlling the system presents multiple challenges. Firslty, the testing machine is required to execute numerous cycles until the threshold FCG rate is exceeded. Once the threshold value is surpassed, the test sequence can be stopped. Additionally, it is crucial to control the load ratio throughout the test. Strategies for managing this will be further detailed in the subsequent chapter.

Requirements for test control:

- Cyclic testing is performed until the threshold FCG rate is surpassed of $10^{-8}m/cycle$. (M)
- Testing is performed under displacement-controlled conditions with a load ratio of 0.1, 0.5 or 0.7. (M)
- The load ratio remains within $\pm 10\%$ of the desired value. (M)

3.2.4 Data analysis

The data collected by the setup requires thorough analysis and calculations to ultimately derive the energy release rate and the FCG rate. Certain calculations, especially those needed to ascertain the FCG rate, must be conducted in real-time during the experiment. All the data that is obtained during the test must be synchronised such that the machine data is combined with the right data of the delamination measurements. The calculation of the strain energy release rate, G, can be done afterwards.

Requirements for data analysis:

- da/dN is calculated by either using the incremental polynomial method. (M)
- The energy release rate is calculated using the Modified Compliance Calibration (MCC) method as described in ISO15024 [5]. (M)
- The data obtained should be plotted as delamination growth resistance curves, i.e. delamination growth rates, da/dN, should be plotted as a function of $\Delta\sqrt{G}$. (M)

4 CONCEPTUAL DESIGN

In this chapter, each function described in the previous chapter will be worked out to come up with a concept of the setup. For each function, different options will be explored and choices will be made. In the next chapter, these concepts will be brought together to obtain a final design.

4.1 Mechanical loading

Mechanical loading of the DCB specimen can be done in several ways. The most common ways, e.g. using a servo-hydraulic or servo-electric tensile testing machine, are elaborated in this section. These machines generally consist of an actuator, a force cell and a displacement transducer. The actuators are available in a variety of technologies and capacities.

4.1.1 Servo-hydraulic

A common method for subjecting the specimen to mechanical loading involves utilizing a servo-hydraulic tensile testing machine. Within the UT laboratory, an Instron servo-hydraulic machine is available. This machine possesses the capability to apply both quasi-static and cyclic loading to a specimen with a capacity of $100kN$. On this machine, a $2.5kN$ Load cell is also available. However, due to the servo-hydraulic system, it is found that the testing frequency for higher amplitude is very limited.

4.1.2 Servo-electric

Another way of loading the specimen with a constant displacement rate concerns the use of a servo-electric testing machine. These machines are capable of testing under accurate displacement and high frequency. These machines are a relatively new technique for testing material behaviour. However, tensile testing machines come in different shapes and sizes. The machine available at the UT lab is the Instron Electropuls E3000 (Figure 4.1). The Electropuls E3000 is a test instrument for dynamic and static testing of materials, which is all electric. Hence, actuation is fully done using electrical energy. This machine is capable of exerting displacement-controlled loads onto the specimen with high accuracy. The machine has a maximum dynamic and static load of $\pm 3000N$ and $\pm 2100N$ respectively and has a stroke of $60mm$, more specifications can be found in Appendix D. The Electropuls E3000 has a load cell pre-installed of $5kN$.

Figure 4.1: Instron Electropuls E3000

4.1.3 Conclusion

Given the availability of an Instron E3000 in the laboratory, it has been selected as the preferred machine for the experimental setup. The Electrical testing device allows for tests with significant amplitude and high frequency, which is restricted with the hydraulic device. Force measurement is carried out with the pre-installed $5kN$ force cell. Although a force cell with a lower capacity might have been more appropriate for this application, the current setup adequately meets the requirements outlined in the protocol by Alderliesten et al. [8], namely an accuracy of 0.5% down to $1/250th$ of the load cell full scale, i.e. 0.5% of $20N$, according to the datasheet in Appendix E.

4.2 Measuring crack length

To be able to automate the DCB test, a suitable way of measuring the crack length should be found. In this chapter, some potential methods of measurement are given.

4.2.1 Electrical resistance method

There are several ways of measuring crack length during DCB testing using Electrical resistance. The Electrical resistance method, or potential difference method (PD), has been used with the success of detecting cracks in fatigue crack studies [32]. This can be done both 'continuous' and 'discontinuous' [33]. The first one makes use of the electrical conductivity of the material itself or from sensor wires attached to the specimen in the length direction. Discontinuous ways are employed using a conductive grid (or conductive lines) across the crack plane.

Discontinuous methods

For discontinuous methods, fracture of the specimen results also in fracture of a conductive grid, placed on the side(s) of the specimen. When the crack front propagates, more conductive lines are broken, which results in a change of resistance. With this change, the location

of the crack tip is obtained. Creating a conductive grid can be done in several ways. Pegorin et al. proposed a way of crack monitoring using z-pins [34]. These pins, made either from composite or metal, are inserted into the material to reduce the through-thickness electrical resistance of composites, as shown in Figure 4.2. This can be used to detect delamination cracking. Since discontinuous methods require extensive specimen preparation and the accuracy of crack length measurement is limited to the increments of the distance of the grid, this way of measuring is not suitable for this assignment.

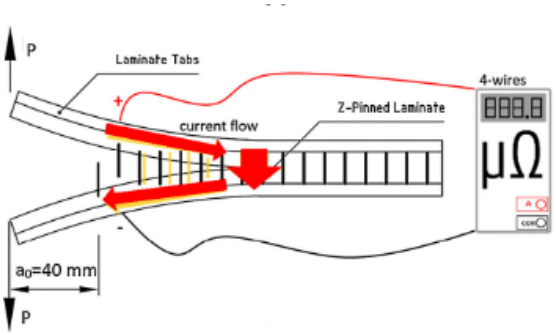

Figure 4.2: Discontinuous electrical resistance method using z-pins [34]

Continuous methods

J.A. van Kuijk et al. did research on measuring crack length using potential drop (PD) measurement on CCT specimens [35]. C. Fischer and F.J. Arendts investigated the continuous electrical crack length measurement method [36]. In this study, two wires were attached to each arm of the DCB specimen (Figure 4.3). Afterwards, the electrical resistance during testing is measured, which should increase when the crack length increases. Wan et al. tried to predict the crack length by integrating multi-walled carbon nanotubes (MWCNT) into composite material. However, fracture mechanisms present in the crack tip have a significant influence on the measured resistance, i.e.: plastic deformation, micro cracks and fiber bridging. Moreover, to obtain a function to relate the resistance to crack length for specific specimen geometry and material, experimental calibration is needed, which is labour-intensive.

For specimens of material that are non-conductive, a separate sensor or conductive layer can be bonded to the material. However, the bonding of the additional sensors or layers influences the measurement. Previous research showed that creating a uniform resistance layer on the specimen is difficult [33].

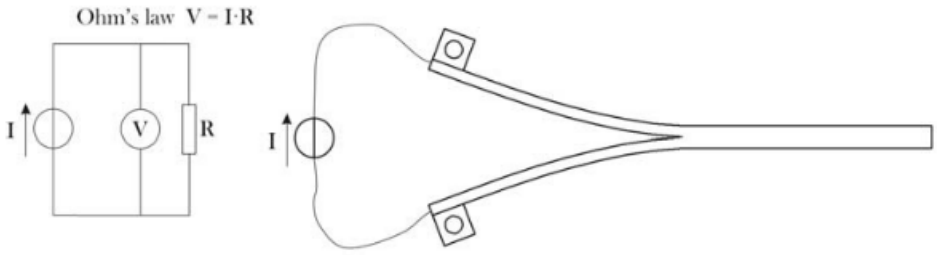

Figure 4.3: Continuous electrical resistance method [33]

4.2.2 Electromagnetic method

Another method of measuring crack length in a DCB specimen is the electromagnetic method. During the fracture of a specimen, the geometry and electromagnetic properties change. A. Obaid and S. Yarlagadda tested such a system [37]. In this research, the time-domain reflectometry (TDR) based technique is shown as an automated sensing method for crack propagation measurements. In this method, a signal and ground signal path are integrated into the specimen during manufacturing or bonded onto the specimen. By sending an electrical signal over the specimen and measuring the reflected signal, the change in geometry can be detected as the signal is reflected when a discontinuity is reached due to the change of impedance. This can be used to predict the location of the crack tip. The basic configuration is shown in Figure 4.4, where, on the right, the TDR oscilloscope is shown. This oscilloscope provides the input voltage and captures the reflected signal. The sensor can consist of any conductive material.

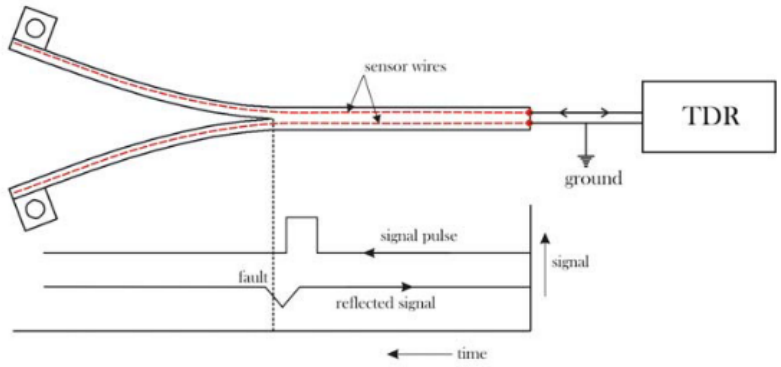

Figure 4.4: Electromagnetic method to measure crack length [33]

However, this method of measuring is particularly applicable for non-conductive materials and hence shows less good results for CFRPs. Therefore, this method of measurement is not suitable for this assignment.

4.2.3 Optical analysis

The most common way of measuring crack length is optical observation. Most of the time, this is done by an operator, but this can also be automated by using a camera and image analysis software. B. Krull et al. introduced a way of automatically measuring the crack length using optical analysis or ”Machine Vision” for translucent glass fiber-reinforced composite DCB specimens [38]. This setup only required a charge-coupled device (CCD) and light source added to a typical DCB test setup. Measurements are acquired by placing a fiber-optic light source under the transparent DCB specimen and monitoring crack propagation from a CCD that is mounted overhead the specimen. Testing of this setup showed reliable and accurate results and was inexpensive. A disadvantage of this way of measuring is that it is limited to translucent materials and hence not applicable for CFRPs.

Y. Zhao et al proposed a way of measuring crack length using digital image correlation (DIC) during fatigue testing of an Aluminium alloy [39]. This setup makes use of two algorithms, the first one corrects the shifted images due to the test that is stopped on different time instances. The latter one is used to detect the crack tip and measure crack length. The first algorithm makes use of detecting interest points, by which it recognises if the specimen is shifted also known as the speeded-up robust features (SURF) algorithm. First, it finds the coordinates of interest points of the original image. Then, the same interest points are obtained in the new image and coordinates are found. Now, it is known how much the specimen has shifted.

The crack tip can be located by identifying the discontinuous displacement field around the crack. When a fatigue crack occurs in the image, a discontinuous region is obtained by the DIC on the displacement field. Hence, the true crack tip can be obtained by determining the boundary end of the displacement field, as shown in figure 4.5.

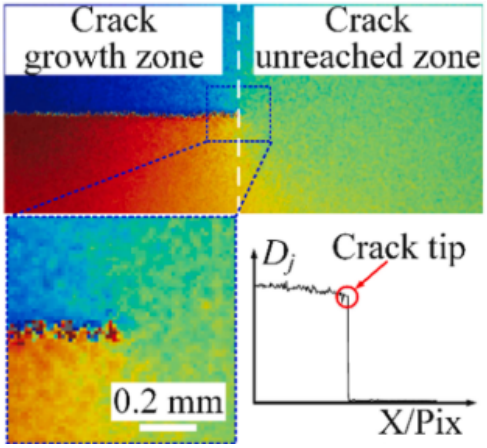

Figure 4.5: Digital Image Correlation [39]

A. Khudiakova et al. applied a similar method to quasi-static testing of a DCB specimen [40]. First, a speckle of black dots on a white background is created on the top and the side of the CF/PEEK specimen. This is done using correction fluid and black spray paint. The specimen was placed in a setup with two cameras, one camera facing the side of the specimen and the other facing the top at an angle of 60°. For the DIC, three reduction methods were used and compared. The first one, the strain method, defines the crack tip position by the high strain concentration observed in the vicinity of the crack tip. In the second method, the crack tip opening displacement (CTOD) method, the crack tip is localised by the coordinate of crack tip opening displacement along the crack plane. the last one, top surface analysis (TSA), was done for comparability. In this method, the position of the crack tip is also defined by a coordinate of CTOD but obtained from the top surface. The obtained crack lengths were in good agreement with measurements done according to the standardised test procedure, using a travelling optical microscope.

J. van de Zand also implemented optical analysis to automate a quasi-static DCB testing setup [33]. In this study, edge detection software was employed in conjunction with a CCD camera. The camera, mounted on an x-y moving table, was designed to track the movement of the crack tip, thereby enabling precise localisation of the crack during the testing process. Earlier research of Uhlig showed with a system, first presented at the Micro Materials conference Berlin in 2000, that Optical Crack Tracing (OCT) improved accuracy and reliability in determining fracture toughness in CT samples [33]. In this setup, the camera was stationary and positioned in front of the specimen. Images made by the camera were afterwards analysed by image analysis software which was able to detect crack tip location. The research showed reliable results, however low contrast between the crack and specimen may lead reduction in accuracy.

4.2.4 Strain-based method

Y. Zhao et al. showed a way to use spectral area to detect the crack location in a specimen by studying the deformation mechanism of fiber Bragg grating (FBG) reflection spectra. This study showed that indeed the spectral area can be used as a reliable damage feature to detect the crack location. However, to achieve these results, extensive calculation using extended finite element method (XFEM) and DIC is needed. Also, additional FBG sensors are needed.

Moreover, the achieved accuracy was low.

4.2.5 Conclusion

In this chapter, four methods of measuring crack length are discussed. For the current assignment, the most suitable option is the optical analysis. This method applies to most materials and does not require extensive specimen preparation. The available hardware and software also make this the best choice. In particular, the edge-detecting method is the most suitable option as this does not require third-party DIC software.

4.3 Control & data analysis

Control and communication can be done in various forms, one approach involves executing both the vision program and machine control using the same LabVIEW program. In this configuration, LabVIEW drivers provided by Instron facilitate the generation of waveforms and ramps using designated Virtual Instruments (VIs), which the machine can then execute. Employing this approach offers the possibility of fully automating the setup, starting with pre-cracking, determining displacement values, and subsequently initiating cyclic loading. However, after consultation with Instron, it was strongly advised against, as this approach disregards safety limits. Therefore, it is recommended to use the dedicated Instron control program, WaveMatrix. Using this program, the test sequence can be built by adding several steps with actions.

However, with the requirement to utilise two distinct software programs, establishing communication either between the two programs or between the machine and the LabVIEW program becomes necessary. This communication can be facilitated through a Data Acquisition (DAQ) system. In the lab of the University of Twente, the NI USB-6008 (8 AI (12-Bit, $10kS/s$), 2 AO ($150Hz$), 12 DIO USB Multifunction I/O) is available. This system features eight analog inputs with a 12-bit analog-to-digital converter (ADC), with a sampling rate of $10kS/s$ and two analog outputs with a maximum update rate of $150Hz$. Additionally, there are 12 digital input/output channels, which can be configured either as input or output channels to interface with for example sensors or other devices. The DAQ is connected to a computer via a USB interface.

5 DETAILED DESIGN & DEVELOPMENT

To enhance clarity and systematic understanding, the design has been subdivided into distinct subsystems. This chapter provides a detailed exploration of each subsystem, elucidating the decision-making process behind the chosen design elements.

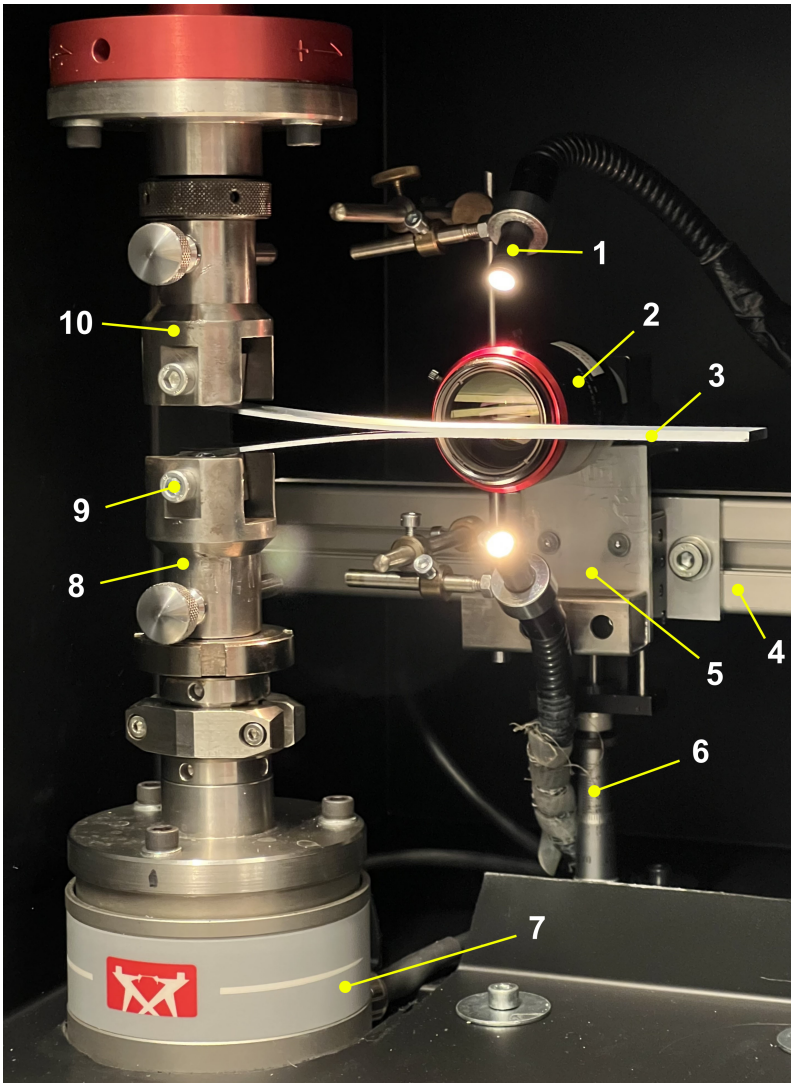

Figure 5.1: Overview of the setup

The complete measurement setup is shown in Figure 5.1, containing the following elements: Dual light source (optical fibers) **1**, camera + lens **2**, DCB specimen **3**, camera mounting frame **4**, camera sledge **5**, linear stage with micrometer **6**, load cell **7**, stationary 'fork' or crosshead **8**, bolt for removing the specimen from the fork **9**, and the moving 'fork' or crosshead **10**.

5.1 Overview

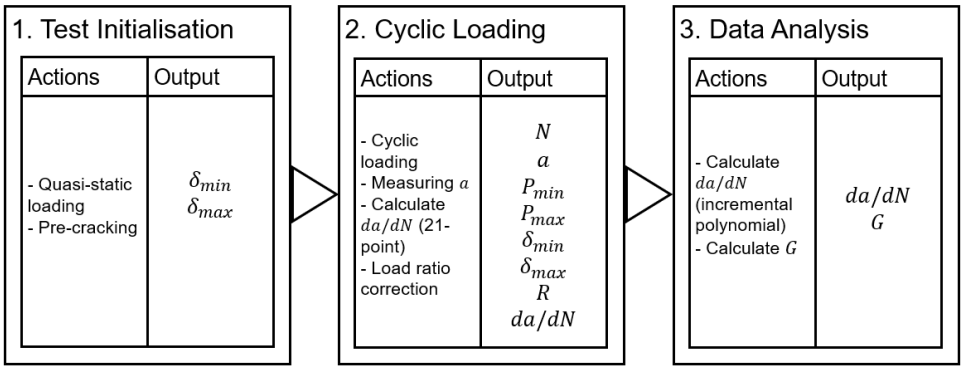

Figure 5.2: Different steps in the measurement procedure

The test procedure can be divided into three distinct steps, as illustrated in Figure 5.2: Test initialisation, cyclic loading and data analysis. In this schematic overview, the actions and outputs of each step are listed. In Appendix B a complete flowchart of the procedure is given.

5.2 Physical setup

5.2.1 Camera position

The camera position can be done in several ways namely; employing a static camera position to capture all the sequences in one frame, another way is to get one sequence in frame and the last option is to track the crack tip with a moving camera. These options will be elaborated on in this section. These 3 options are schematically represented in Figure 5.3.

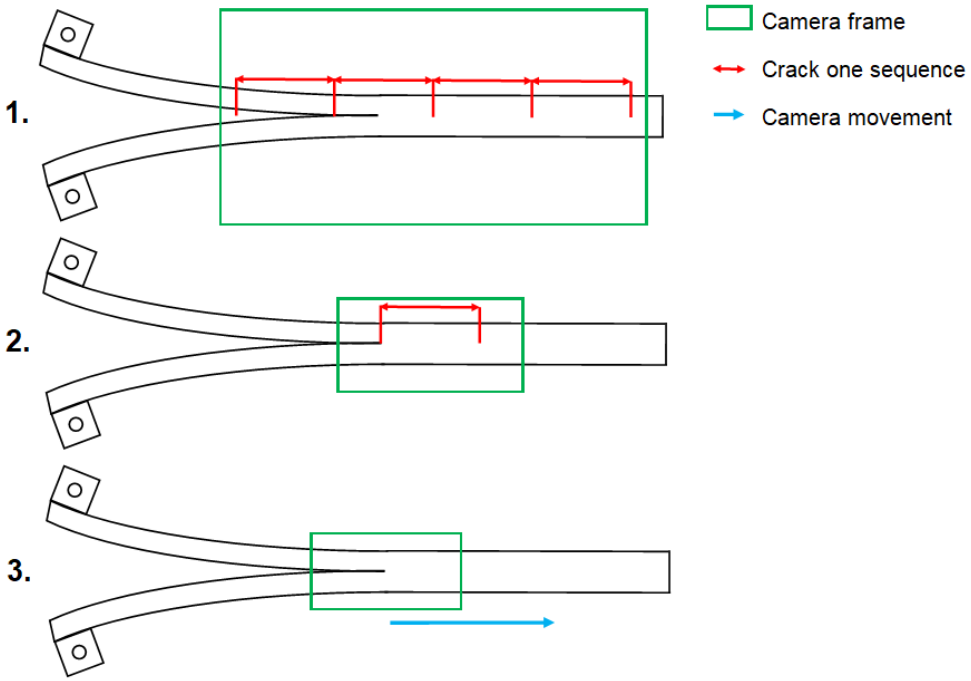

Figure 5.3: Options for camera position

1. **Capture all sequences:** The first concept is to fix the position of the camera to capture all

sequences within a single frame. The advantage of this setup is that there is a fixed zero point for all measurements, eliminating errors associated with moving the camera between sequences, i.e. each crack length can be measured from a fixed origin. A drawback of this approach is the necessity for high-resolution images to achieve accurate measurements. Additionally, the specimen length or the measurable delamination length is constrained by the fixed camera frame dimensions.

2. **Capture one sequence:** The second concept is to fix the position of the camera during one sequence of a test. After completing a sequence, the camera is relocated to capture the next sequence. This camera positioning method requires a lower resolution for accurate crack tip measurements. However, the drawback lies in the cumulative error associated with displacing the camera and setting a new origin for each sequence. Another advantage of this option is that the specimen length is less constrained. While the delamination length for a single sequence is limited to the frame, the camera can be moved over a considerable distance between sequences.

3. **Tracking crack tip:** In this approach, the camera tracks the crack length using actuators. Crack length can subsequently be determined by actuator displacement. The advantages of this concept include the absence of limitations on the length of delamination for a single sequence and the overall specimen length. Additionally, the camera can now be positioned at a short distance from the specimen surface, eliminating the need for a high-resolution camera. The setup introduces errors linked with tracking control and the system's complexity. Additionally, it necessitates the camera to move in both horizontal and vertical directions. This requirement for multi-directional camera movement complicates the design and may affect the accuracy and reliability of the measurements.

To choose between the concepts mentioned above, a few parameters of the camera and lens have to be known. The camera has to have the right resolution and refresh rate and the lens has to have the right focal length. When these parameters are known, the minimal camera resolution can be calculated. With this specified, the test can be designed with the use of the protocol of Alderliesten et al. One important aspect of the test is the minimal crack growth rate that has to be measured, i.e. $10^{-8} m/cycle$. This implies that the accuracy of the camera setup should be high enough and/or the test frequency should be sufficiently high to make sure that the test has a reasonable execution time. In the protocol from Alderliesten et al., it is prescribed that an entire delamination length is captured, i.e. 100 mm. It is also required that the camera has a resolution sufficient to measure delamination of $0.05mm$. Considering these specified requirements, it is possible to determine the minimum pixel frame required. For instance, the minimum number of pixels in the x-direction can be calculated as follows: with each pixel representing $0.05mm$, a $100mm$ span would require $100/0.05 = 2000 pixels$. However, this calculation is based on the assumption that the effects of lens distortion are disregarded. Subsequently, the assumption is made that, with this resolution and at this distance, the crack tip can be easily localised. However, experimenting with a prototype setup indicates that this is not the case, i.e. the crack tip is so thin that it requires a minimum pixel size. Hence, to ensure a high enough resolution to make a sufficiently accurate measurement, the second option, i.e. the capture of one sequence, is chosen for the final design.

As can be seen in Figure 5.1, the camera is placed close to the specimen, in this way a $\pm 35mm$ frame is captured. The camera can be moved in a 2D plane using the camera sledge (which can slide through a slot in the frame in the horizontal direction) and the linear stage (which can move in the vertical direction).

5.2.2 Contrast & light

For lighting of the specimen, a dual light source is used to enhance the contrast of the crack. This dual setup minimizes the visibility of surface roughness by eliminating shadows that would be present with a single light source. Minimizing the visibility of the surface roughness increases the visibility of where the crack tip location is. Additionally, to further improve the visibility of the crack tip, the sides of the specimen are coated with a thin layer of matte white spray paint.

To maintain consistent image contrast across varying lighting conditions, such as day and night, a box is constructed to shield the specimen from environmental light. The inside of the box is treated with a dark coating to enhance its light-blocking capabilities.

For further enhancing crack tip contrast, it is preferable to open the specimen as widely as possible, while still preventing any additional crack propagation. To ensure the stability of the crack and prevent propagation during a pause, the machine is stopped at the mean of the cyclic displacement range. Later, the opening displacement was increased to 75% of $\delta_{max} - \delta_{min}$ to further increase contrast near the crack tip.

5.2.3 Fixtures

Specialised fixtures are fabricated to secure the specimen in the machine, as illustrated in Figure 5.1. These fixtures, referred to as 'Forks', incorporate an axis that is held in place by a short bolt at the end. To remove the specimen from the machine, this bolt can be loosened. The load blocks fixed on the specimen are equipped with two bearings to minimize friction, which avoids unexpected forces and reduces wear during extensive testing. It is worth noting that the specimen is attached to the load blocks using a specialized tool designed to guarantee proper alignment. This tool is depicted in Figure 5.4. Employing this tool, the load blocks are adhered to the specimen. The parallel clamp is used to ensure parallel alignment with the specimen, ensuring effective adhesion during the glueing process.

5.2.4 Alignment

To minimize measurement error, precise alignment of the camera with the specimen is crucial. The alignment process involves placing a specimen in the machine and measuring the distance between the specimen and the frame at two points — namely, at the beginning and the tip of the specimen — using a calliper. If any disparity exists between these measured values, adjustments are made to the machine's rotation. This iterative procedure is repeated to minimize the discrepancy in the measured distances. As a result, repeated alignment of the machine for each new specimen tested is not seen as necessary.

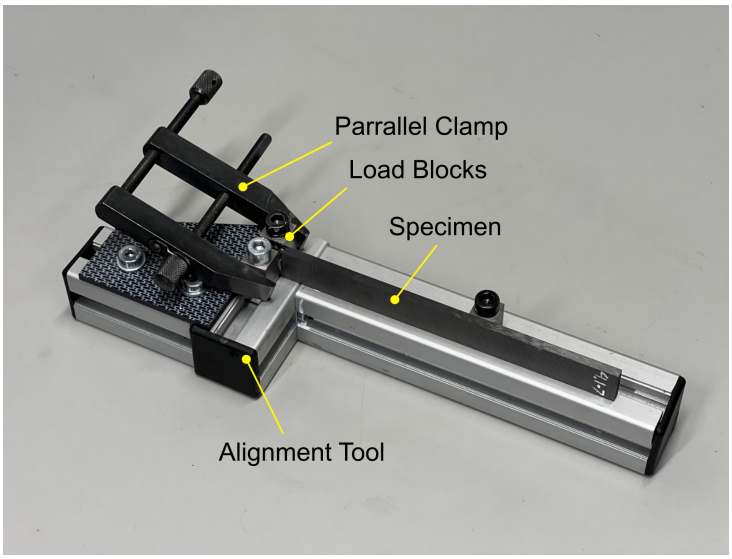

Figure 5.4: Alignment tool to glue load blocks to the specimen

5.3 Camera

The camera used for the setup is an IDS U3-3800CP-M-GL Rev.2.2 in combination with a Kowa LM25FC24M lens. The camera has a 1” CMOS Mono sensor with a resolution of 5536x3692 pixels. The lens has a focal length of 25mm. Detailed specifications of these components can be found in Appendix F. This chapter provides explanations of various crucial aspects relating to the camera and lens.

5.3.1 Camera settings

To obtain a high-quality image, it is crucial that the specimen is positioned inside the sharp focus region, also known as the depth of field (DOF). This region is the depth range in which the camera is able to capture a sharp image of an object. The opening of the diaphragm, also known as the aperture, has an influence on the DOF. A smaller aperture corresponds to a larger DOF [41]. Given the use of an adjustable light source, the aperture is minimized to ensure a sufficiently extensive DOF. Once these parameters are configured, the lens is focused to capture a sharp image of the specimen. With the camera now appropriately set, the next section describes the process of camera calibration.

5.3.2 Camera calibration

An important issue in computer vision is camera calibration. Accurate calibration of the camera with lens is especially crucial for applications that involve quantitative measurements such as dimensional measurements. Camera distortion arises primarily from two sources: the distortion in the lens itself and the internal misalignment of the camera and lens assembly, e.g. the camera sensor may not be orthogonal to the optical axis of the lens and the centre of the sensor array may not coincide with the optical principle point, i.e. the intersection of the optical axis and the image plane. The first aspect of camera calibration is to estimate the internal parameters of the camera. These parameters describe how the image coordinates of a point are derived, given the spatial position of the point with respect to the camera. The other aspect is the geometrical relation between the camera and the scene, the parameters that characterize this geometrical relation are called external parameters [42].

When an image is taken by the camera, this image contains lens distortion. This is a deviation from the ideal projection. Lens distortion is a form of optical aberration in which straight lines in the real world do not remain straight in an image. In Figure 5.5 examples of lens distortion can be seen, barrel distortion and pincushion distortion. [43]

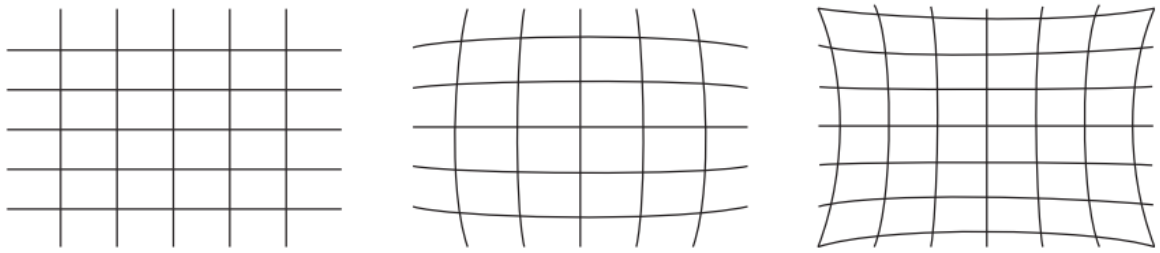

Figure 5.5: Different types of lens distortion on a rectangular grid (left): barrel distortion (centre) and pincushion distortion (right) [43]

To correct for this lens distortion, a software model can be used. LabVIEW has a function for this purpose. In the vision assistant of LabVIEW, it is possible to fit a polynomial distortion model to the incoming image. This form of geometric calibration uses a projective camera (pinhole) model of a camera, after which a distortion model describes the mathematical deviation of a camera from the pinhole model. This polynomial model is also known as the Brown-Conrady model. This model is defined in the form of a transformation of a point from undistorted coordinates, u_n, v_n, to distorted coordinates, u_d, v_d, see equation 5.1.

$$\begin{aligned} u_d &= u_n \left(1 + K_1 r^2 + K_2 r^4 + \cdots\right) + \left(P_2 \left(r^2 + 2u_n^2\right) + 2P_1 u_n v_n\right) \cdot \left(1 + P_3 r^2 + P_4 r^4 + \cdots\right), \\ v_d &= v_n \left(1 + K_1 r^2 + K_2 r^4 + \cdots\right) + \left(P_1 \left(r^2 + 2v_n^2\right) + 2P_2 u_n v_n\right) \cdot \left(1 + P_3 r^2 + P_4 r^4 + \cdots\right), \end{aligned} \tag{5.1}$$

In which $r = \sqrt{(u_n - u_c)^2 + (v_n - v_c)^2}$ and u_c, v_c are coordinates of the distortion center. In this equation, K_n are the radial distortion coefficients and P_n are the tangential distortion coefficients. The forms of distortion shown in Figure 5.5, can be corrected using the radial distortion coefficients. Tangential distortion occurs when the camera sensor is misaligned with the camera lens.

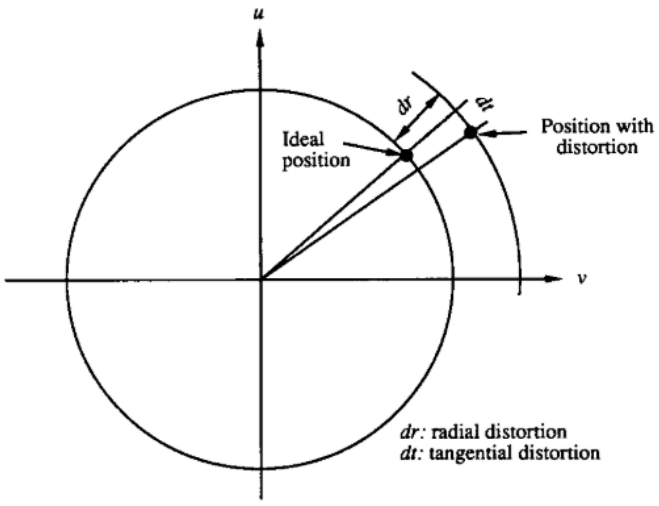

Figure 5.6: Radial and tangential distortion [42]

LabVIEW can determine both the radial and tangential distortion coefficients. The difference between radial and tangential distortion can be seen in Figure 5.6. To strive for consistent results and to reduce the effects of potential radial distortions, it is advisable to take an image with the crack positioned in the middle, thereby aiming for $u = 0$. This practice aims to enhance the consistency and accuracy of the measurement process. Other than distortion, the camera can also be calibrated for perspective error. This error occurs when the camera axis is not perpendicular to the object under inspection.

The distortion model is created using LabVIEW's Vision Assistant. To create a distortion model, an image made of a calibration grid has to be uploaded to the vision assistant. It is important that the image of the calibration grid is taken at the right distance with the right camera settings, therefore an insert is 3D-printed for the machine (of which the 2D-drawing can be found in Appendix G) and the dot pattern is printed on thick paper with $1.25mm$ distance between the dots. Using this tool, the camera can be easily calibrated. The insert can be seen in Figure 5.7a.

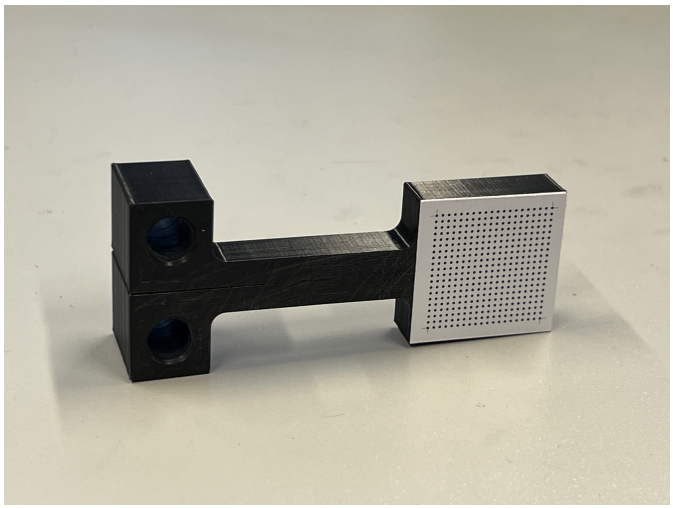

(a) 3D printed calibration insert

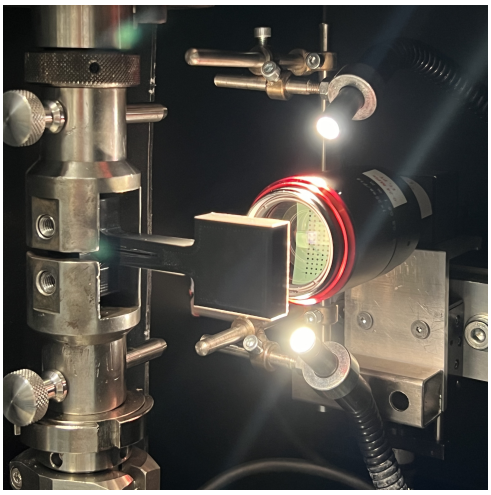

(b) Calibration insert in the machine

Figure 5.7: Camera calibration using a calibration grid

One or more images of the distortion grid can be uploaded in the LabVIEW Vision Assistant (more images may be used to fully cover the image frame of the camera). The dots on this grid are automatically recognised by the Vision Assistant. By obtaining the specific location of the dots, a distortion model can be created (figure 5.8). In this figure, each step done by the vision assistant is shown. In the first sub-figure, the original image of the calibration grid can be seen. In the second and third sub-figures, the fitted distortion model is indicated by the red arrows. These indicate where the dots should be in the real world. The barrel distortion is visualised by the coloured image in the third sub-figure. The colour scale identifies the amount of error, i.e. the lighter the colour, the bigger the error. It can be seen that the incoming image has barrel distortion, hence K_1 is negative. In the fourth sub-figure, the corrected image is shown. Each image made with the vision program automatically gets corrected with this model, such that the crack length can be measured correctly.

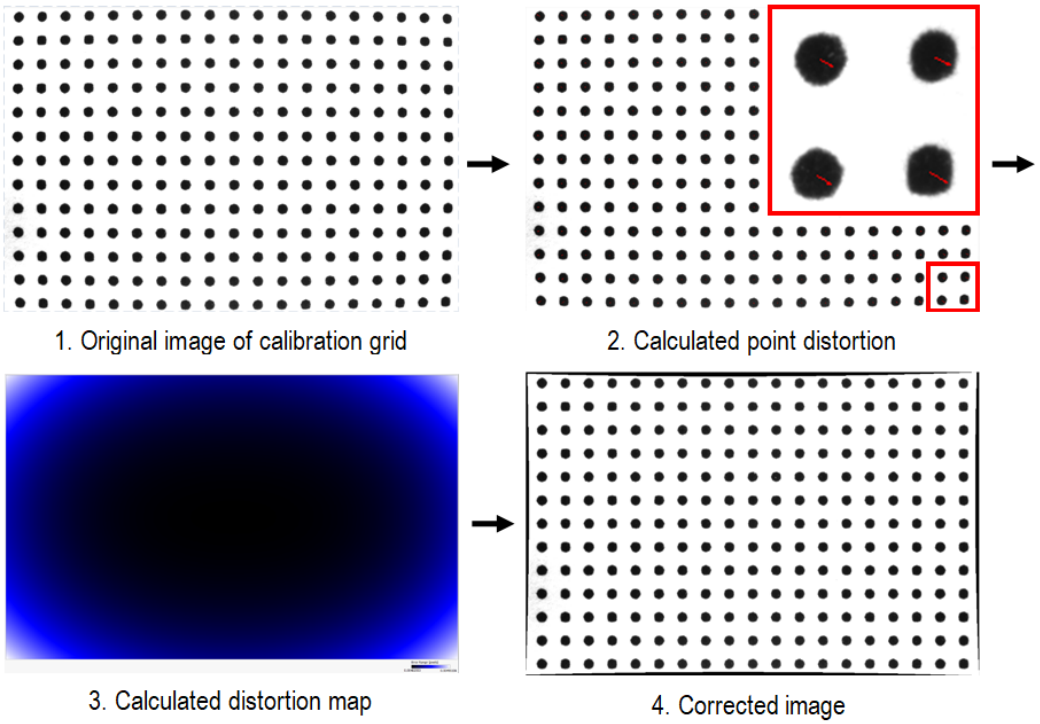

Figure 5.8: Lens distortion model

Since the distance between the dots of the image grid is known, a conversion from pixel coordinates of a point to real-world coordinates can be done using the designated LabVIEW function called: 'Convert Pixel to Real World'. This function uses the obtained distortion model to convert points in pixel coordinates to points in real-world coordinates.

5.3.3 Distortion model validation

To validate the accuracy of the distortion model, images were captured of a calibration glass across the entire width of the image, e.g. also images were taken with the glass on the far left and on the far right of the image. The configuration used for capturing these images is depicted in Figure 5.9a. One of the obtained images is shown in Figure 5.9b.

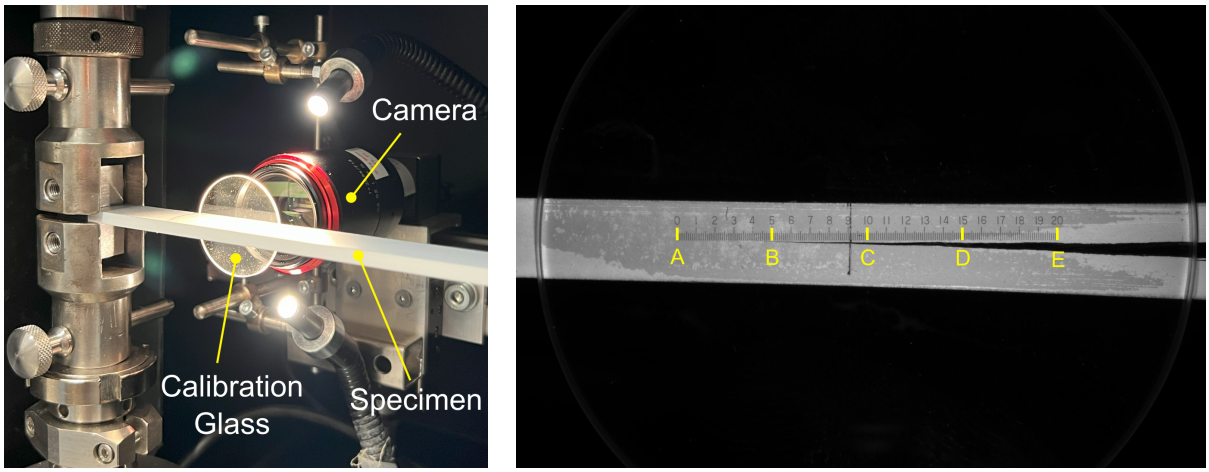

(a) Camera setup with calibration glass

(b) Image of calibration glass

Figure 5.9: Camera calibration using a calibration glass

The reference points are marked in yellow. The 'real world'-distance between the reference is $5mm$. Following the application of the distortion model for correction, the pixel coordinates of these points are identified. These pixel coordinates are then converted into real-world coordinates using the 'Convert Pixel to Real World' function in LabVIEW. This process is conducted with two separate images: one representing the left side of the image, denoted with the subscript 'L', and another for the right side, denoted with the subscript 'R'. After converting from pixel to real-world coordinates, the distance between the points should measure $5mm$. The outcomes of this validation process are presented in Table 5.1.

Table 5.1: Validation of distortion model

Point	Pixel Coordinate (pix)	Real world Coordinate (mm)	Real World Distance (mm)	Error (mm)
A_L	113	0.76	-	-
B_L	862	5.78	5.02	0.02
C_L	1610	10.80	5.02	0.02
D_L	2356	15.81	5.01	0.01
E_L	3099	20.79	4.98	-0.02
A_R	2442	16.38	-	-
B_R	3186	21.37	4.99	-0.01
C_R	3929	26.36	4.99	-0.01
D_R	4669	31.32	4.96	-0.04
E_R	5407	36.28	4.96	-0.04

Table 5.1 reveals that the image appears stretched on the left side and compressed on the right, yet the resulting error is minimal. This discrepancy in the measurements could be due to residual perspective distortion, likely arising from a slight remaining misalignment in the camera setup. To further analyse this, the error can be plotted against the x-coordinate of the image, taking the left side of the image as the origin. This graphical representation, shown in Figure 5.10, suggests a linear relationship between the x-coordinate and the error, indicative of perspective distortion. By applying a linear regression to this relationship, it is possible to correct for the perspective error thereby enhancing the accuracy of the measurements.

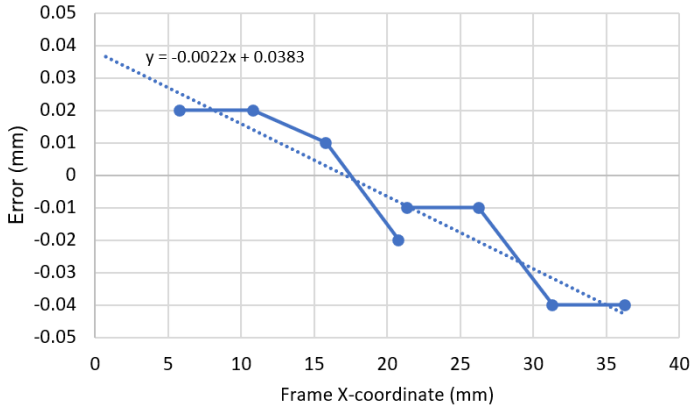

Figure 5.10: Residual perspective error

The linear relation for an estimation of the perspective error, ε_{pers}, can be expressed as a function of the x-coordinate of the image frame, x_{frame}, as:

$$\varepsilon_{pers} = -0.0022 x_{frame} + 0.0383 \tag{5.2}$$

Hence to obtain the correct x-coordinate of the crack tip, the measured x-coordinate will be corrected in the following way:

$$x_{corrected} = x + \varepsilon_{pers} \tag{5.3}$$

Using Table 5.1, an estimation of the pixel length can be made, which can be calculated by:

$$\frac{\Delta L_{RW}}{\Delta L_{pix}} = \frac{36.28 - 0.76}{5407 - 113} = \frac{35.52}{5294} = 6.7 \mu m \tag{5.4}$$

In which ΔL_{RW} is the distance in mm and ΔL_{pix} is the distance in pixels. Since the distortion is not linear, this only gives an estimation of the average pixel length.

5.4 Vision software

With the incoming image now corrected for distortion, a procedure to recognise the crack tip and evaluate its position can be developed. The program that is accountable for this operation is written in LabVIEW. In this section, the steps performed by the program are explained.

When the LabVIEW program is started, the user is first asked to select a region of interest (ROI) around the area where the crack will propagate, this initial manually selected ROI is visually represented as the orange rectangle in Figure 5.12. Once this selection is confirmed, the program enters a loop, awaiting a signal from the Instron E3000 to capture an image.

Once a signal is received, the camera takes an image. This image serves as input for the rest of the LabVIEW program. Using the ROI defined by the operator, an initial estimation of the crack tip is done. This is done using the ”IMAQ Rake 3” function from LabVIEW. Using this ”rake” function, edges can be found along a set of vertical lines defined inside a rectangular region, which is in this case the manually selected ROI. This function determines edges based on their contrast and slope. The principle behind this function is shown in Figure 5.11.

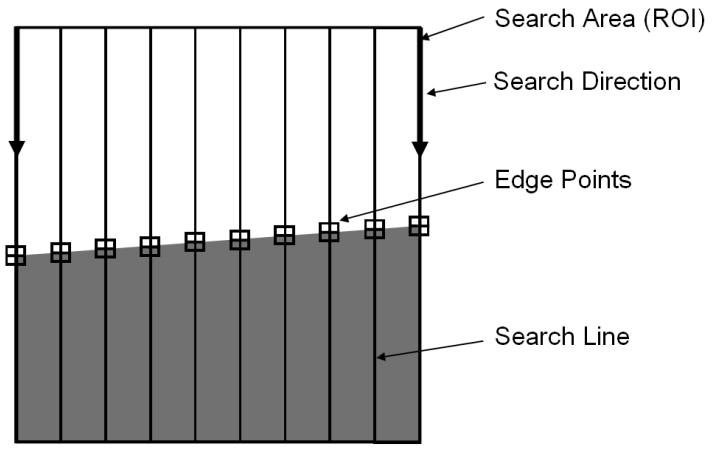

Figure 5.11: Schematic representation of LabVIEW’s Rake function

There are several options within LabVIEW for defining parameters used in computing edge gradient information for edge detection. Among these, ”Minimum Edge Strength” and ”Width” are particularly significant for this use case. The Minimum Edge Strength parameter specifies the minimal gradient magnitude of the contrast, necessary for an edge to be identified. The Width

parameter specifies the number of pixels averaged perpendicular to the search line direction to detect the edge, hence this parameter ensures that a detected edge has a minimum amount of pixels in the horizontal direction.

To mitigate the impact of potential contaminants on the side of the specimen (for example, broken fibers adhering to the specimen) or external factors like damages, scratches, or surface roughness that could lead to inaccurate crack tip detection, an iterative approach to refine the determination of the crack tip location is employed. In each iteration, the values for both Minimum Edge Strength and Width are adjusted. To initially get a rough estimation of the crack tip location, a relatively high value is set for both parameters. This leads to the program obtaining the first estimation of the crack tip (point 1 in Figure 5.12). Although this may not accurately determine the crack tip location, it provides the program with a preliminary estimation of its location.

Subsequently, a new iteration is started within an automatically generated ROI, represented by the yellow rectangle in the figure. This ROI has smaller, pre-defined dimensions. For this iteration, the values for both Minimum Edge Strength and Width are lowered, resulting in the detection of point 2. In the final iteration, another automatically generated ROI is introduced, with further reduced dimensions. This ROI is indicated by the green rectangle in the figure. With a further reduction in both parameters, an accurate approximation of the crack tip is achieved, denoted as point 3 in Figure 5.12. The measure of accuracy is discussed in the chapter accuracy.

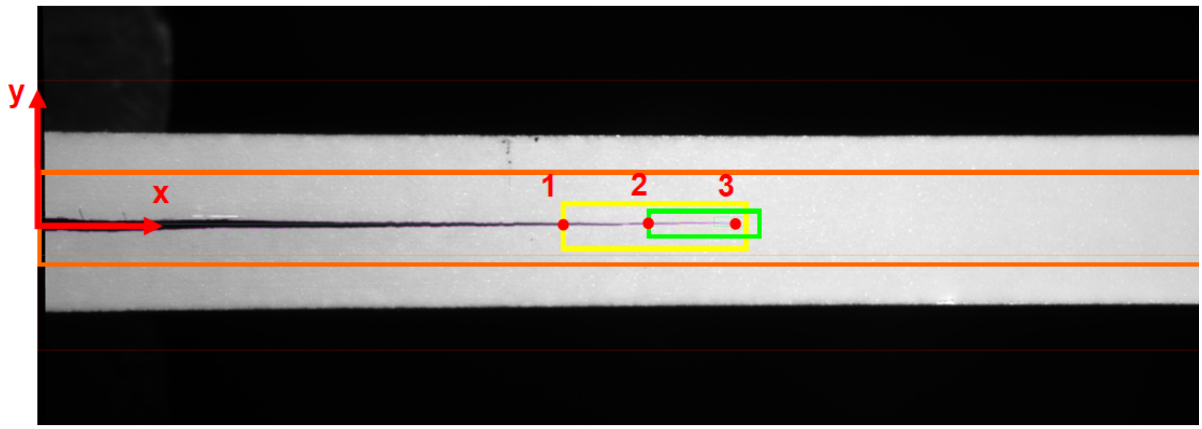

Figure 5.12: Schematic representation of vision algorithm

The origin of the vision coordinate system is positioned on the left side of the corrected image. Hence the crack length is defined as the distance, x, in pixels between the origin and the obtained crack tip position. To obtain the crack length in millimeters, another function within LabVIEW can be used. As shown in the previous section, the LabVIEW function 'Convert Pixel to Real World' is used to convert pixel coordinates to 'real world'-coordinates. When this is all done correctly, the Image in Figure 5.13 is obtained.

As previously discussed in Section 2.4, the delamination length is measured by the horizontal distance, x. Consequently, there is no requirement for large displacement correction, i.e. $F = 1$ in Equation 2.23 [5]. This allows for the use of x as a direct substitute for a for the calculation of the energy release rate, G. Furthermore, it is assumed that the increment in delamination length, da, in the calculation of the FCG-rate, da/dN, corresponds directly to the measurement taken over the x-coordinate, i.e. dx/dN. In Appendix K, a geometrical calculation is performed to assess the difference between x and a. The results from this calculation demonstrate that the discrepancy between dx and da is indeed minimal and can be regarded as negligible. For the

sake of consistency and clarity throughout this report, the FCG rate will continue to be denoted as da/dN.

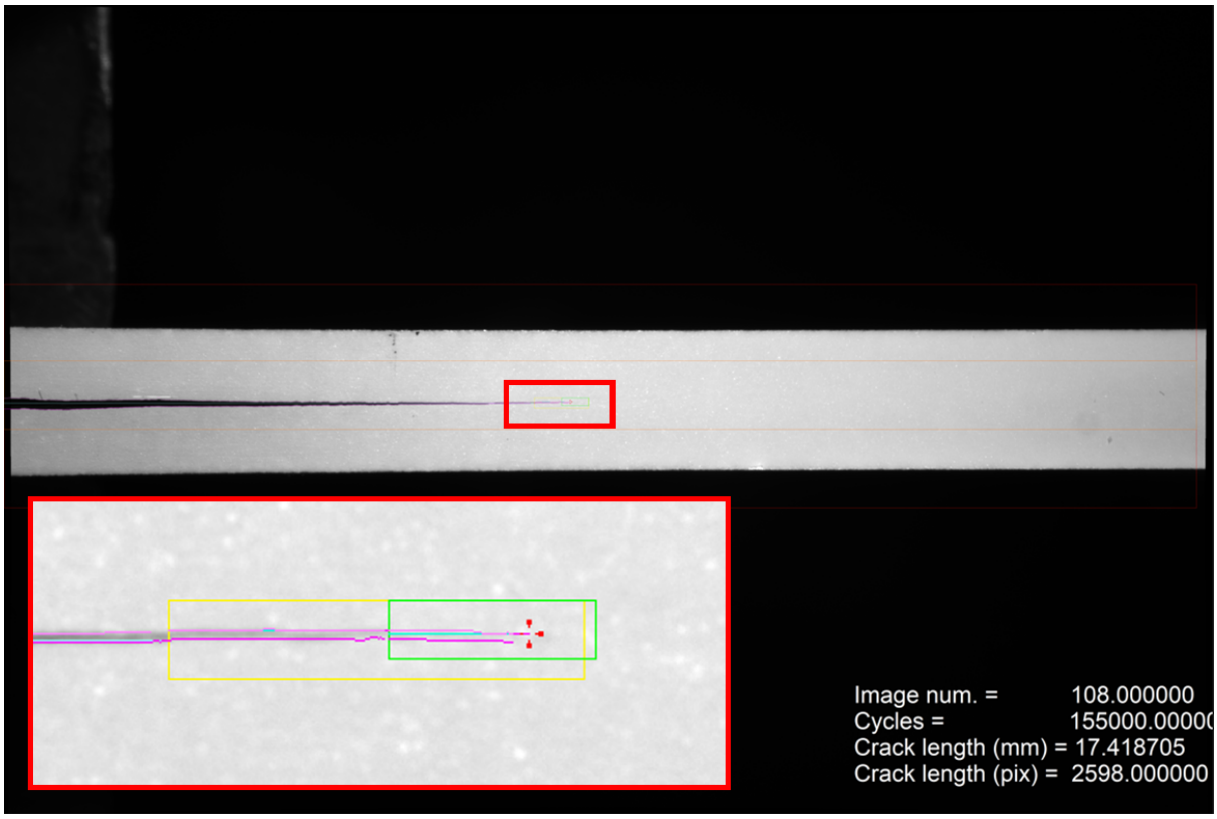

Figure 5.13: Image taken by the vision program with added close-up

In the bottom left corner of Figure 5.13, a close-up is shown of the image processed by the vision program. The detected edges are indicated by purple lines. The location of the crack tip is indicated by the red arrows. In the bottom right corner, the data obtained for this measurement is shown. The accuracy of the prescribed procedure is evaluated in the next chapter.

5.5 Machine control

WaveMatrix is the software that controls the machine. This software program is developed by Instron and is designed to control and operate the Electropuls E3000 cyclic testing system. WaveMatrix provides an interface that allows the control and configure the testing parameters of the Electropuls E3000. With this software, a test sequence can be made. The testing parameters are input for WaveMatrix. Using this program, all cycle intervals are planned with the desired displacement values following the pre-loading procedure. The program itself has a max cycle number of 5,000,000 cycles pre-programmed. However, these will not be completed, since the test is automatically aborted when the threshold value for the FCG-rate is surpassed.

Figure 5.14: Test sequence in WaveMatrix

A typical test sequence is depicted in Figure 5.14, outlining the planned actions for each step. The arrows in steps 1,2,4,6 and 8 indicate a ramp waveform. Using the ramp waveform, the machine is set to the desired displacement and rotation. In step 3, the machine is set to 75% of δ_{max} and a $5V$ analog signal is sent to the vision program to take an image. In step 4, the machine is moved back to the mean position of the cyclic displacement. In step 5, the cyclic waveform is started. This first waveform consists of 100 cycles, after which the machine is stopped at the mean of the cyclic displacement. Step 6 moves the machine back to the 75% location to take another image. A grey arrow is shown above steps 5,6,7 and 8, indicating a loop, i.e. steps 5,6,7 and 8 are performed 50 times. On the grey dots, a second and third loop are programmed. In this way, the desired image interval can be set. In rows 3 and 4 of the scheme, the generated analog output can be set. These signals are also used to communicate with the LabVIEW program to control indicators on the user interface of the vision program and to count the number of cycles performed, as will be explained further in Section 5.6.

5.5.1 Load ratio control

As described in Chapter 3, it is important to keep the load ratio, i.e. $R_P = P_{min}/P_{max}$ in a window of $\pm 10\%$ of the desired value. This can be done manually, as described in the protocol. In this way, the operator has to keep an eye on the load ratio during the test and adjust δ_{min} when necessary. Another way is to automate the adjustment of δ_{min} using the advanced control package and the calculations package within WaveMatrix. First, the load ratio has to be calculated using the calculations package, this program makes use of a user subroutine written using the C programming language. With this code, the maximum load and minimum load measured within a cycle can be extracted and divided, hence a real-time load ratio can be calculated and

displayed on the test panel. This load ratio serves as input for the advanced control package, which subsequently controls the load ratio by adjusting δ_{min}. First, it is observed how the load ratio changes when no correction is done. This can be seen in Figure 5.15. If no correction is done, the load ratio will vary between 0.12 and 0.02 for an expected load ratio of 0.1, hence giving a 80% deviation in the worst case.

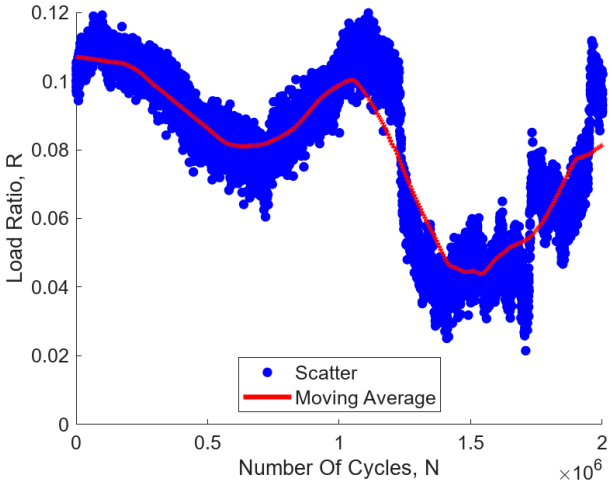

Figure 5.15: Change of load ratio during $1 * 10^6$ cycles

In Figure 5.16 the zoomed-in graph for the first 350,000 cycles can be seen of both the uncorrected and the corrected load ratio of two different sequences. In Figure 5.16a, it can be seen that there is a downward trend in the ratio, whereas in Figure 5.16b, the corrected load ratio is controlled in a window of 5%.

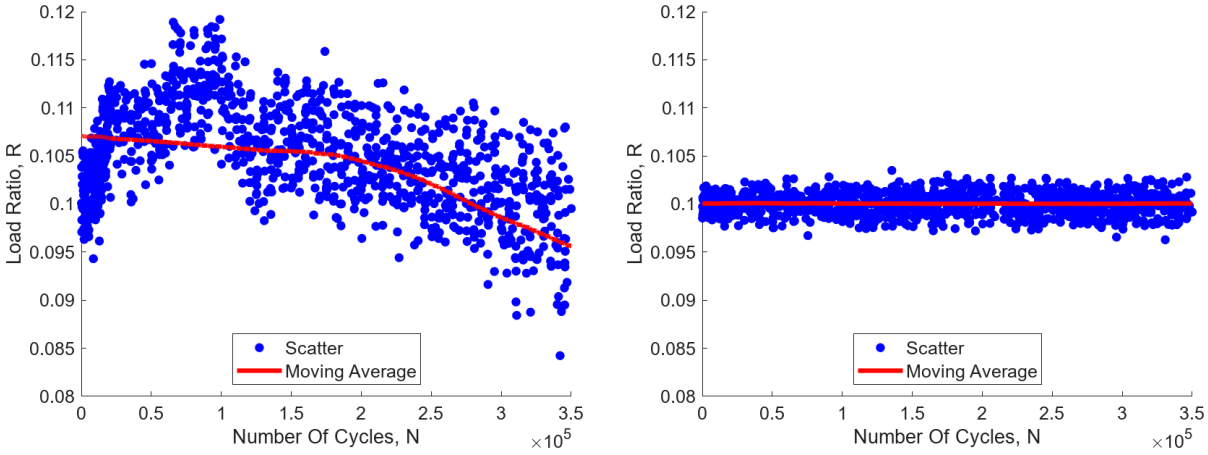

(a) Load Ratio without correction

(b) Load Ratio with correction

Figure 5.16: Load ratio control

5.5.2 Safety

Another crucial aspect of the program involves implementing safety measures. For instance, if the load blocks become detached from the specimen, the machine has to stop. This is achieved through the utilization of limits that can be configured on the sensors. A loose specimen has the potential to cause damage to the machine. During testing, the load cell constantly monitors a tensile force. When the specimen comes in between the grips of the cyclic testing machine, a compression force is observed, this force is limited to $-20N$. When the force exceeds this limit, the machine stops immediately and an automated error message is sent to the operator

via email. Further details regarding communication with the operator are elucidated later in Section 5.6.1. Additionally, there are displacement limits on both vertical displacement and rotation to prevent overloading the load cell and frame during low power or manual control mode. The machine is also stopped automatically when these limits are exceeded due to any other unexpected cause.

5.6 Communication & data analysis

5.6.1 Communication

The communication within the system can be divided into two categories, i.e. communication between different hardware components and software and communication with the operator. Both are described in this section.

Setup communication

The system uses multiple hardware and software. For the setup, two computers are in use. The first computer controls the Instron testing machine with the WaveMatrix software. This computer is directly connected, via an Ethernet card, to the Instron 8800MT controller which subsequently controls the machine itself. The computer, on which LabVIEW is running, communicates with the Vision camera and with the Instron controller via a DAQ system. An overview of the hardware components is depicted in Figure 5.17.

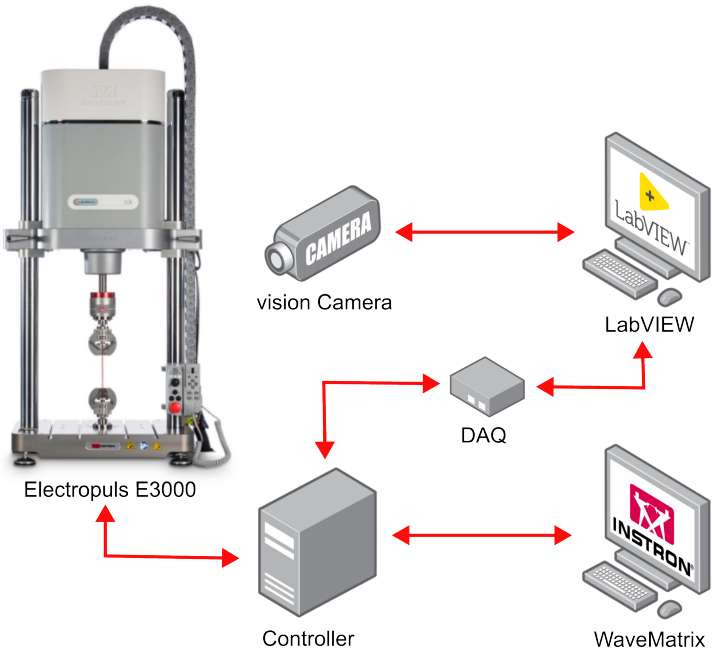

Figure 5.17: Overview of the communication between components

The LabVIEW PC is in charge of the vision program, which automatically measures the crack length with its vision program. It is important that the vision program exactly knows when to generate an image and measure crack length, in order to synchronise this event, communication between either the two computers or between the machine and the LabVIEW computer is needed. The latter one is used in this specific case. Communication between the fatigue testing machine and the LabVIEW computer is done using a DAQ, which can be plugged into the computer using a USB connection. This DAQ can receive and generate analog signals. The 8800MT controller is capable of generating an analog when steps in the program sequences

are started, as explained in Section 5.5. This signal is received by the DAQ, which can subsequently trigger the LabVIEW program to take an image. The LabVIEW computer constantly checks, via the DAQ, for a change in this analog signal. When a threshold value is surpassed, the program initiates the capture of an image and proceeds to measure the crack length.

By counting the incoming signals, the number of performed cycles is calculated by the LabVIEW computer. By linking the number of cycles performed to the measured delamination length, the data can later be synchronised with the data obtained by the Instron machine. The synchronisation of data obtained by both computers will be further explained in Section 5.6.2.

With both values known for the applied number of cycles, N, and the delamination length, a, the FCG-rate, da/dN, is calculated using a polynomial fitting method discussed in Section 3.1.3. When the calculated FCG rate exceeds the minimum rate of $10^{-8} m/cycle$, an analog signal is generated by the DAQ and sent to the Instron Controller such that the test is stopped. To make the vision program less sensitive for scatter in the measured delamination length and hence ensure that enough cycles are performed before the test is ended, a polynomial is fitted over 21 points instead of 7.

Operator communication

With the implementation of a fully automated setup, the operator now has the flexibility to engage in other tasks. However, since testing scenarios are susceptible to unforeseen issues, it becomes crucial to notify the operator when such events occur. Notification is facilitated through two channels: email and a real-time dashboard. If an error arises in the LabVIEW program during testing, an error message is automatically generated, which is then sent to the operator via email. If an error arises in WaveMatrix, or the machine stops due to an unforeseen issue, the LabVIEW program is also able to notify the operator. This functionality is implemented using a counter in the LabVIEW program that tracks the time elapsed since the last signal was received from the machine controller. When this duration exceeds a predetermined threshold - the interval within which a new trigger signal is typically expected - the program automatically sends an email notification to the operator. These functionalities enable the operator to respond quickly, minimizing the machine's non-operational time. Another critical point is the conclusion of the test, as it cannot always be pre-planned due to the difference in material in reaching the threshold value for the FCG rate. Consequently, once this threshold is achieved, an email notification is sent to the operator.

Figure 5.18: Online operator dashboard

An alternative method for closely tracking the test's status involves utilizing an online dashboard, as illustrated in Figure 5.18. This dashboard is continually updated in real-time with the most recent test data. The test data that is gathered during testing is constantly sent to an online database, with which this dashboard communicates. Consequently, the operator gains the ability to assess the test's conformity to expectations from any location. Additionally, the operator can ascertain whether the test is nearing completion and plan accordingly to either conclude the current test or initiate a new sequence in a timely manner.

5.6.2 Data analysis

Data is logged in WaveMatrix and LabVIEW, after which both synchronised data sets are combined and post-processed with Matlab to calculate da/dN and G for every crack length. Data processing is done using the two computers in parallel, where the WaveMatrix computer is responsible for gathering data measured by the Electropuls and load cell and the LabVIEW computer is responsible for measuring the crack length. Afterwards, the data can be gathered together and FCG rate and energy release rate can be calculated. An overview of the data flow is shown in Figure 5.19.

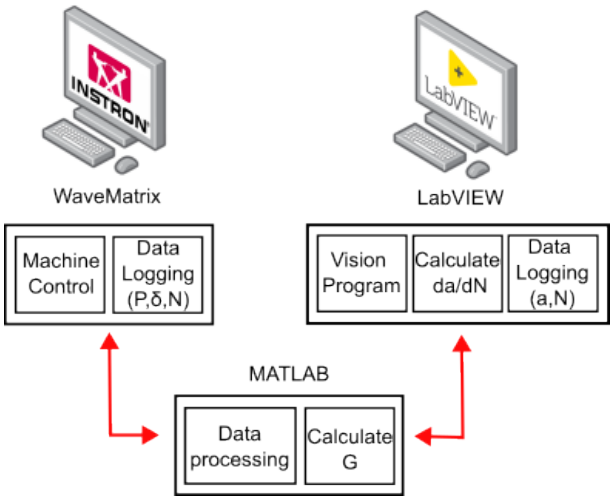

Figure 5.19: Overview of the information flow between computers

The WaveMatrix PC records measured data in a SVC file that contains various data, including the number of performed cycles, N. In the LabVIEW program, the number of performed cycles is determined by counting the incoming signals that trigger the image capture and multiplying this with the predetermined measuring interval. This calculated number of N is stored in the data file along with the measured delamination length. With the number of performed cycles for each data point now established, data from both computers can be merged. To facilitate this integration, a MATLAB program is developed. This MATLAB program is subsequently used to calculate both the energy release rate, G, and the FCG rate, da/dN. The FCG-rate calculation employs the 7-point incremental polynomial method as detailed in Section 3.1.3.

5.7 'Live Feed' program

In addition to the program described in this chapter, 'DCB Fatigue Tester', which captures an image upon receiving an incoming analog signal, another program has been developed to analyse live feed, named 'Live Tester'. This LabVIEW program is used during the pre-cracking process and the preparation for the fatigue test. During the pre-cracking (or quasi-static loading) process, this program is essential for monitoring if there is any increment in delamination length. The specimen loading can be stopped using the designated button, which sends a signal to the Instron machine and thereby reverses the specimen loading instantly. The possible increment in delamination resulting from pre-cracking can also be measured using this program.

Furthermore, it provides the flexibility to adjust the vision algorithm's parameters via the live feed, ensuring enhanced accuracy in the actual fatigue test.

In the live feed, a square is displayed in the centre of the image to facilitate camera alignment. By positioning the specimen within this square, proper alignment can be achieved. The camera's y-position is precisely adjusted using its linear stage. Additionally, the camera is positioned correctly on the x-axis to ensure the crack tip starts on the left side of the image. Once this is set up properly, the fatigue test can be started using the 'DCB Fatigue Tester' program.

5.8 User interface

The testing procedure employs two distinct LabVIEW programs. The first program is designed to capture an image as soon as it receives an incoming analog signal from the machine, called:

'DCB Fatigue Tester'. The user interface of this program is shown in Figure 5.20. The second program is developed to analyse live feed by the vision program, called: 'Live Tester', the user interface is displayed in Figure 5.21. The user interfaces of both programs are concisely explained in the following sections. For a more in-depth explanation of the user interfaces, reference can be made to the manual provided to the University of Twente. Appendix H provides images of all the different tabs of the programs.

5.8.1 'DCB Fatigue Tester'

Figure 5.20: 'DCB Fatigue Tester' user interface

The graphical user interface (GUI) of the 'DCB Fatigue Tester' is depicted in Figure 5.20. Some key functions of the user interface include:

1. **Incoming Image Display:** Shows the last obtained image of the specimen.
2. **Delamination Length vs. Image Number:** Visualizes the delamination length plotted over the number of images, i.e. every incoming data point is plotted with the same distance on the x-axis. Since the measurement frequency decreases, the plot shows no logarithmic behaviour.
3. **Fatigue Crack Growth (FCG) Rate:** Displays the FCG rate over the number of cycles, calculated using both the secant method and a 21-point polynomial fit. A higher number of data points is chosen for this fit (instead of 7 points), such that the test is not stopped too early due to a fluctuation in the measured data.
4. **Delamination Length vs. Number of Cycles:** visualises the delamination length plotted over the number of cycles. This plot shows logarithmic behaviour.
5. **Polynomial Fitting for FCG Rate:** graphs both the last obtained 21 data points and the 2nd order polynomial fitted, used for determining the average FCG rate.

5.8.2 'Live Tester'

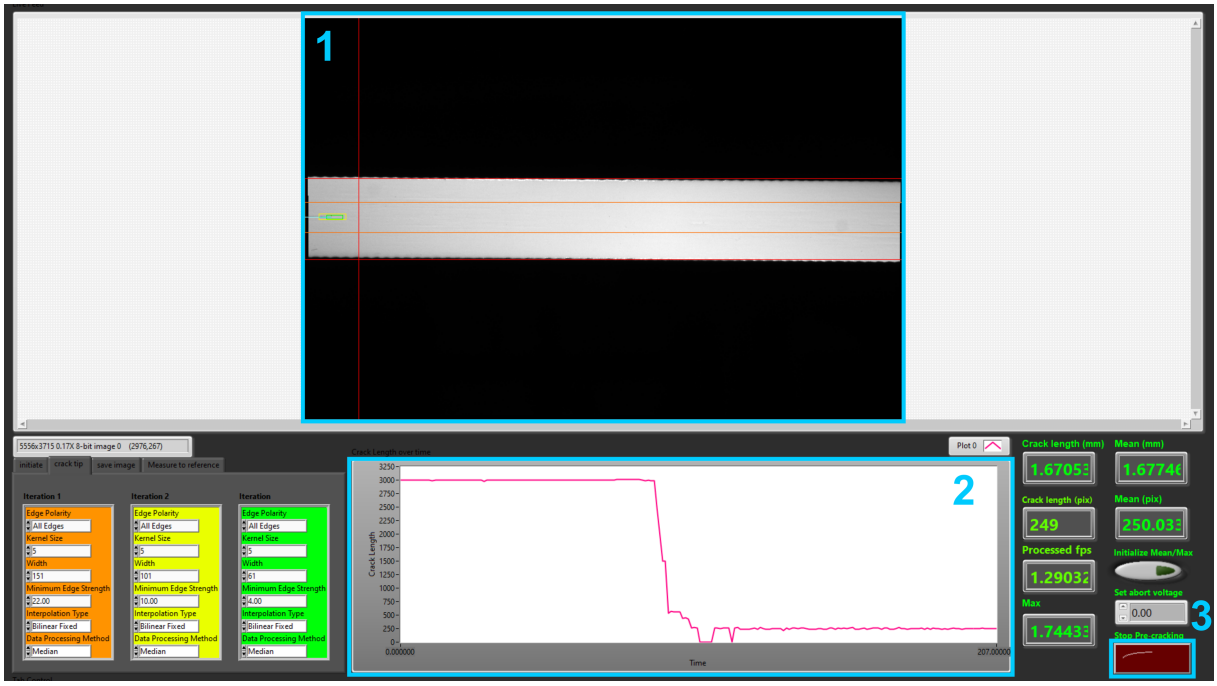

Figure 5.21: 'Live Tester' user interface

The GUI of the 'Live Tester' program is depicted in Figure 5.21. Some key functions of this program are:

1. **Live Camera Feed:** Displays the real-time video feed from the camera.
2. **Crack Length Plot:** Shows a graph of the detected crack length in pixels plotted over time.
3. **Abort Button for Pre-Cracking Loading:** A dedicated button to immediately stop the quasi-static loading during pre-cracking. Pressing this button sends an analog output signal to the testing machine to reverse the loading instantly.

5.9 Testing procedure

This section provides a concise, step-by-step guide for the testing procedure. A more detailed testing manual is provided to the University of Twente, enabling other operators to use the setup effectively.

1. **initial Delamination Measurement:**
    - Measure the initial delamination of the specimen using a microscope
2. **Pre-cracking:**
    - Place the specimen in the machine and start the 'Live Tester'.
    - Begin quasi-static loading the create the pre-crack. Monitor both the 'Live Tester' and the force-displacement curve (displayed on the WaveMatrix computer) for signs of crack propagation, aiming to keep the pre-crack length limited to a maximum of $3mm$.

- Stop the loading using the designated button in the 'Live Tester'.

3. **Post-Pre-Cracking Measurement:**
    - Remove the specimen from the machine.
    - Measure the delamination length after pre-cracking, a_p, using a microscope. This measurement is the starting point for Sequence A.
4. **Setting up Fatigue Test:**
    - Determine opening displacement for image capture.
    - Manually adjust the machine to the set opening displacement. Use the 'Live Tester' feed to position the camera, adjusting the linear slide for the y-direction and the camera sledge for the x-direction.
5. **Starting the Fatigue Test:**
    - Launch the 'DCB Fatigue Tester' program.
    - Follow the instructions in the dialogue box to correctly save data and manually select the ROI.
    - Start the machine, and the LabVIEW program will await an incoming signal to measure the delamination length.
6. **Quasi-Static Pre-Cracking for Next Sequence:**
    - Restart the 'Live Tester' and determine the average crack tip location.
    - Start the quasi-static pre-cracking. Once non-linearity appears in the force-displacement curve, stop the loading.
    - Return the machine to the last opening displacement and check for any increase in delamination length. If observed, add this increment to the last recorded delamination length, establishing the starting value for the next sequence.
7. **Repeat Fatigue Testing:**
    - Resume the fatigue testing process.
    - Continue this cycle until sufficient data is collected.

The total delamination length, as outlined in the procedure, is determined through the following summation:

$$a = a_p + \Delta a_A + \Delta a_{Bp} + \Delta a_B + \Delta a_{Cp} + \Delta a_C + ... + \Delta a_{np} + \Delta a_n \tag{5.5}$$

Where Δa represents the increase in delamination length during fatigue loading, and Δa_p denotes the increment in delamination length that occurs during the pre-cracking procedure.

6 DESIGN VALIDATION & INTEGRATION

6.1 Error analysis

Errors in measurements can be classified as either random or systematic. Random errors are statistical fluctuations, in either direction, in the measured data due to the limitations of the precision (i.e. repeatability) of the measurement device. In this specific case, the error made between iterations of the vision program can be categorised as such random error. The error made can be evaluated by statistical analysis, which is done in section 6.1.2. Subsequently, this error can be reduced by averaging over a number of measurements. Systematic errors are inaccuracies that are consistently in the same direction and reproducible [44]. The ability of the vision program to locate the crack tip, with the chosen hardware (camera + lens), has in this case a systematic error. This will be elaborated in section 6.1.1. A schematic representation of both errors is shown in Figure 6.1.

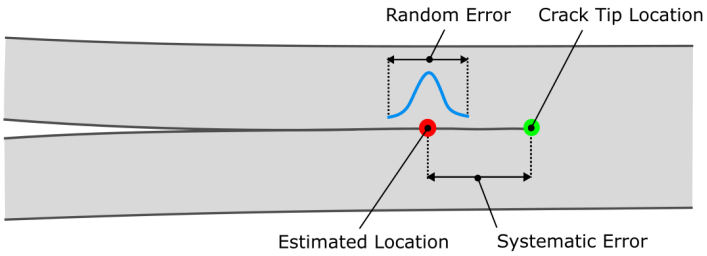

Figure 6.1: Random and systematic error

6.1.1 Systematic error

The ”International vocabulary of metrology” defines accuracy as the following: ”closeness of agreement between a measured quantity value and a true quantity value of a measurand” [45]. Accuracy is not a quantity expressed as a numerical value but an attribute of a measurement. A measurement is more accurate when it has a smaller measurement error, i.e. has less bias. High accuracy can be achieved by calibration and can be determined by repeatedly measuring a standard that has a known true value [45].

The accuracy and the systematic error of the test setup are determined by comparing the measurement done by the vision program to a measurement with a known value. the latter one is done using an optical microscope. The systematic error is expected to estimate the crack tip location in a lower x coordinate than where it actually is, since closer to the crack tip, the contrast of the crack tip will decrease and the resolution of the camera will be a limiting factor. To obtain the location of the crack tip, a reference point is needed. Therefore, a scratch is made in the coating with a scalpel knife. The location of this scratch can be easily obtained with the vision program and a crack length in pixels is found for this location. The same is done for the crack tip location. Both pixel coordinates are now input for the distortion model, by which real-world coordinates are obtained. Now the crack tip location in reference to the scratch is known. In

Figure 6.2, the distance between the scratch and the crack tip is shown.

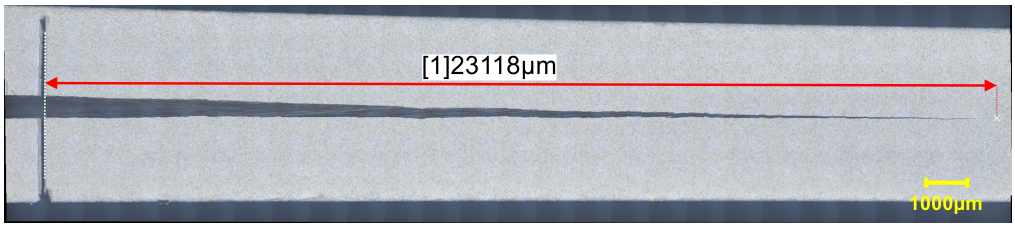

Figure 6.2: Determine accuracy using a scalpel knife scratch

Now the same is done using an optical microscope, featured with a crossline eyepiece reticle, and a linear stage with a micrometer. The micrometer is zeroed once the scratch is observed through the microscope. The linear stage is now turned until the crack tip is found, from the micrometer, the crack length can be obtained. This value is taken as the 'true value' even though there is also some error in obtaining the crack tip location using the optical microscope.

Since the images of the vision program are taken with the same displacement during the whole sequence, it is expected that the systematic error will increase later in the test. This is due to the fact that the crack opening reduces while the crack grows at constant maximum crosshead displacement. The collected data supports this expectation. In Table 6.1, the systematic errors found for the vision program are shown. The error at the end of a sequence, i.e. with a small crack opening, is indeed higher than at the start. The error made at the end is a factor of ± 2 higher.

Table 6.1: Systematic error in vision program

Mean Error Start	Mean error End	Mean Error Combinded
mm	mm	mm
-0.087	-0.170	-0.135

The systematic error can be compensated by a correction factor to reduce the bias. To compensate for the systematic error, a linear relation can be obtained between the systematic error and the delamination length. However, it is important to note that this represents an estimation of the error, derived from multiple sequences. The true error is likely variable, depending on the opening displacement, making it unique to each sequence. Consequently, it is challenging to generalize this error across different sequences. Therefore, the assumption is made that the systematic error is similar for each sequence. Since the initial delamination, a_p, is measured using a microscope, it is taken as the true starting value for sequence A. Hence the relation for the systematic boils down to:

$$\varepsilon_{sys} = 0.00453 a_{seq} \tag{6.1}$$

where a_{seq} is the delamination length for a specific sequence starting at zero for every new sequence. The systematic error can be compensated by the following equation:

$$a_{cor} = a - \varepsilon_{sys} \tag{6.2}$$

The correction for the error is carried out during data analysis in MATLAB. The delamination length measured at the end of a sequence is used as the starting point for the subsequent sequence as explained in section 5.9. It is important to note that this method of summing up delamination lengths leads to an accumulation of errors since the compensation applied is based on an estimation and does not precisely account for all the inaccuracies in measurement.

6.1.2 Random error

The precision of measurement is defined as the ”closeness of agreement between indications or measured quantity values obtained by replicate measurements on the same or similar objects under specified conditions” [45]. Hence, the more precise a measurement is, the less variability around its mean value it has.

To determine the precision and hence for this specific situation, the random error of the measurement setup, the machine is run for a few cycles with very small displacement values such that no crack growth is initiated. The machine is stopped 100 times and the vision program did 100 measurements, in this way, the random error of the measurement is observed. The results of this test can be seen in figure 6.3.

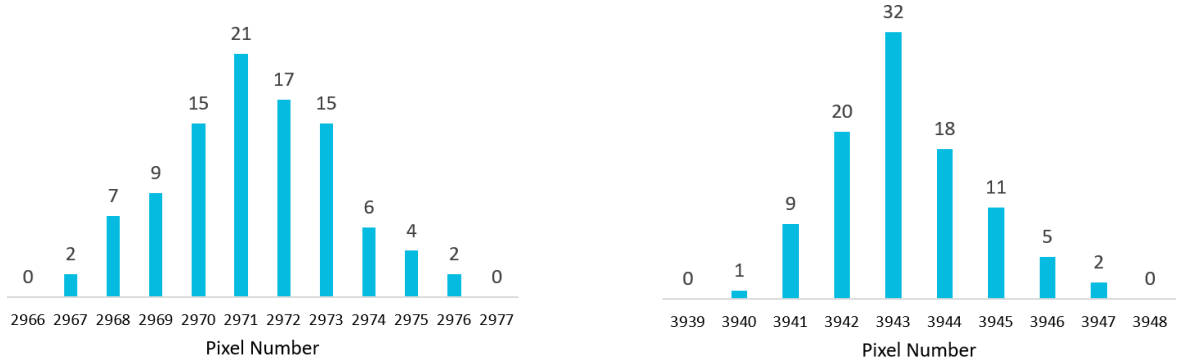

(a) Random error of C-Epoxy seq. D

(b) Random error of C-Epoxy seq. E

Figure 6.3: Radom error in measurement

In this figure, a histogram displays the pixel numbers obtained from two measurements. As can be seen, the standard deviation for a random error is not constant, this is probably due to the reason that a crack tip does not always form in a clear way. An example of such a branching crack is shown in Figure 6.4.

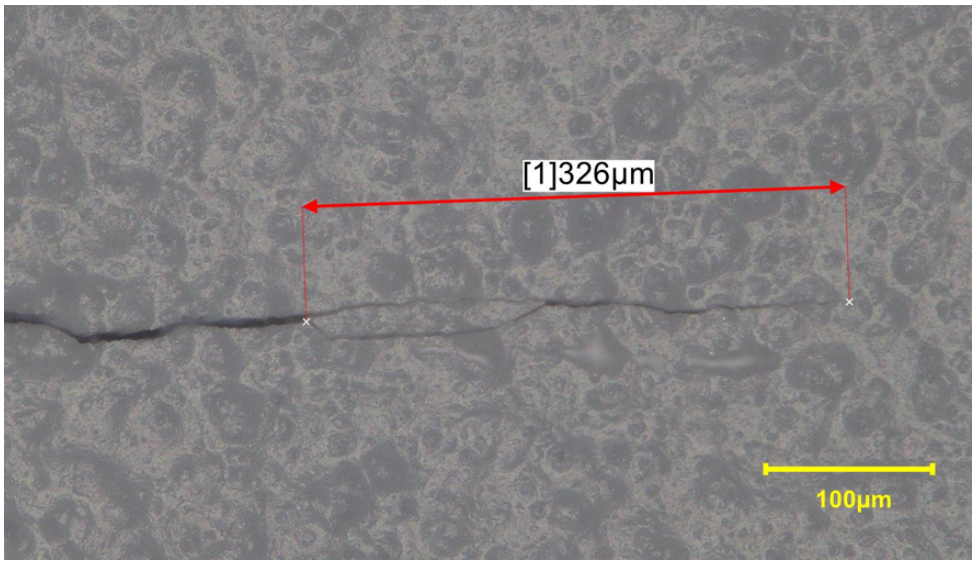

Figure 6.4: Unclear crack tip propagation

This measurement is done several times at the start and the end of the sequence. When the

standard deviation of these measurements is combined, a 'pooled standard deviation' in real-world coordinates is obtained to be $0.01313mm$.

6.1.3 Influence on results

Now the accuracy and precision of the measurement setup are established, it becomes essential to quantify their influence on the results. The ISO Guide to the Expression of Uncertainty in Measurement (GUM) [46], provides a method to estimate measurement uncertainty. The GUM method supposes a mathematical model that describes the functional relationship between the measurand and the influence quantities. The paper of Adams [47] is also used to estimate the measurement uncertainty. The method assumes that systematic effects are identified and compensated for, therefore only the random error is taken into account. For simplicity, the SBT formulation for the energy release rate, G, is recalled:

$$G_I = \frac{3P\delta}{2Ba} \tag{6.3}$$

For each parameter, the standard uncertainty and the sensitivity coefficients have to be evaluated. The standard uncertainty for the delamination length, a, is of 'Type A', i.e. the uncertainty is derived from statistical analysis of existing data. Hence, the standard uncertainty is taken to be the remaining random error of $0.01313mm$ (assuming that the systematic error is properly compensated). For parameters P, δ and B the uncertainties are obtained using a 'Type B uncertainty estimate', i.e. the magnitude of the uncertainty has to be obtained from data sheets, handbooks, etc. The load, P, can be determined within $\pm 0.1N$, which is obtained from the data sheet (Appendix D). Since the Electropuls complies with the ASTM E2309 [48], the maximum error for the displacement, δ, is 0.5% of the total stroke, i.e. $\pm 0.3mm$, assuming it passes the 'class A' classification. For the specimen width, B, which is measured using a micrometer, an error of $\pm 0.005mm$ is assumed. For the 'Type B' uncertainty estimates, a rectangular distribution is taken.

For each parameter, the values of the uncertainty contributors, u_i, and the sensitivity coefficients, c_i are given in Table 6.2. For the rest of the uncertainty calculation, the measurement data of the last performed cycle of sequence E is used. With these values, the combined standard uncertainty, u_c, can be determined using Equation 6.4. The details of this calculation can be found in Appendix I.

$$u_c = \sqrt{\sum_i c_i^2 u_i^2} \tag{6.4}$$

As can be seen in Table 6.2, the units of both parameters are such that when the product is taken, the uncertainty is expressed in the units of the energy release rate, G.

Table 6.2: Uncertainty of parameters

Parameter	Standard Uncertainty, u_i	Sensitivity Coefficient, c_i
P	$u_p = 0.05774N$	$c_p = 0.01177 \frac{\frac{J}{mm^2}}{N}$
δ	$u_\delta = 0.1732mm$	$c_\delta = 0.01468 \frac{J}{mm^3}$
B	$u_B = 0.002887mm$	$c_B = -0.02250 \frac{J}{mm^3}$
a	$u_a = 0.01313mm$	$c_a = -0.03289 \frac{J}{mm^3}$

Finally, the combined standard uncertainty of the SBT calculation of the energy release rate, G, is determined to be $449.94 \pm 3.7 J/m^2$ for the last measured cycle.

For the parameter da/dN, precision in measurement is crucial. In this context, there is no cumulative error from the previous sequence. The deviation due to the random error, significantly influences da/dN, particularly towards the end of a sequence when very low rates are being measured. To address this, a polynomial is fitted to the last seven obtained data points. Subsequently, a derivative is computed on this polynomial, allowing the determination of an average FCG rate. This approach helps mitigate errors introduced by the vision program, providing a more robust and accurate representation of the data.

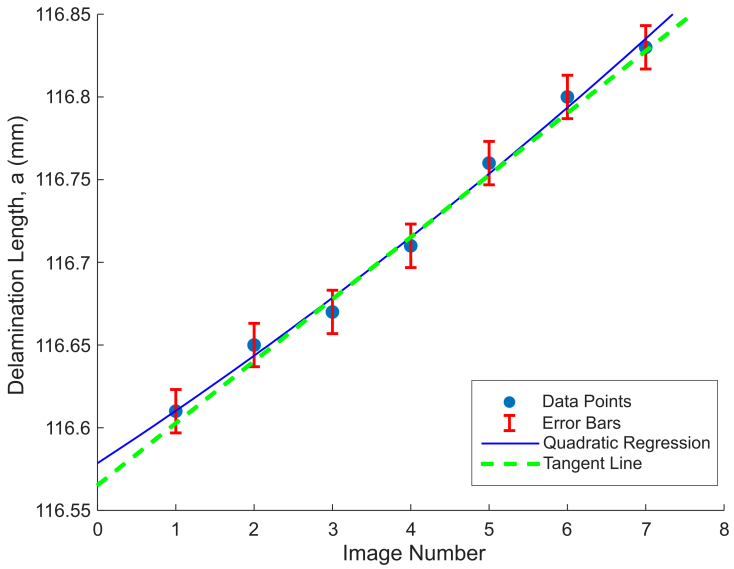

Figure 6.5: Error mitigation due to 7-point polynomial fit

In Figure 6.5, the 7-point polynomial fit can be seen. In light blue, the measured data points of the last 7 measurements of sequence E (C-Epoxy) can be seen. The red error bars indicate the magnitude of the random measurement error, i.e. a standard deviation of $0.01313mm$. The dark blue line is the second-order polynomial fitted through the obtained data points. Finally, the tangential line (in green) is plotted at the midpoint, by which the slope and hence, the average FCG rate is determined.

6.2 Results of the final design

In this section, the results obtained from the tests are shown. During testing, several specimens are used. The data shown in this chapter is experimental data coming from two different materials, namely a thermoplastic (TP) and thermoset (TS) material. The thermoplastic material is Toray Cetex TC1225 LMPAEK. The thermoset material is a Carbon fiber-epoxy namely: M30SC-150-DT 120-34 F from Delta Preg in Italy. The latter one is a specimen coming from the European Structural Integrity Society Technical Committee 4 (ESIS TC4) Round Robin test.

6.2.1 Influence of pre-cracking on FCG-curves

According to the protocol by Alderleisten et al. [8], the 'pre-cracking' phase, also referred to as the 'quasi-static loading procedure', which initiates a new sequence, should be stopped once non-linearity in the force-displacement curve is observed. However, adhering to this guideline for the C-LMPAEK specimens results in the curves depicted in Figure 6.6.

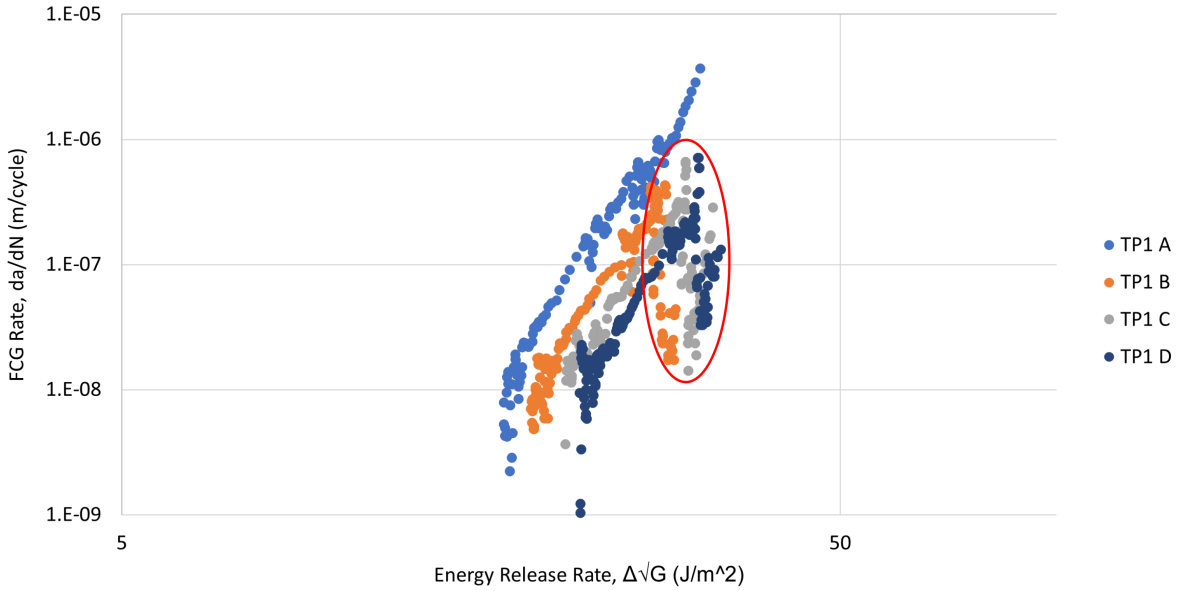

Figure 6.6: Fatigue resistance curves without delamination increment in the quasi-static loading procedure

The data for sequence A, where the crack has been extended for a few millimeters during pre-cracking, presents a linear plot. However, stopping the quasi-static loading process immediately after the observation of non-linearity for subsequent sequences results in the scatter highlighted in red in Figure 6.6. This shows the necessity of allowing the crack to grow by a small increment before fatigue cycling is started to achieve repeatable results. Consequently, in subsequent tests on C-LMPAEK, the crack was allowed to extend by a minimal increment, which was then measured and added to the total delamination length.

6.2.2 Results for C-LMPAEK & C-Epoxy

First, the curves of the delamination length and the FCG rate over the Number of cycles are shown for the first sequence of both materials.

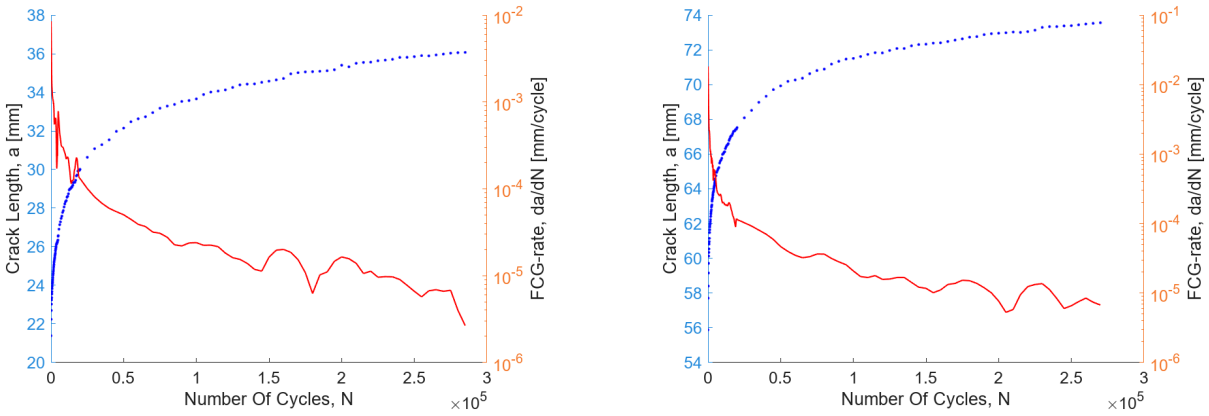

(a) C-LMPAEK Sequence A

(b) C-Epoxy Sequence A

Figure 6.7: Measured delamination length and FCG-rate over performed cycles

Using the plot in Figure 6.8, the slope, m, as used in the MCC-method (Equation 2.23), can be determined. With this value, the energy release rate, G, can be calculated.

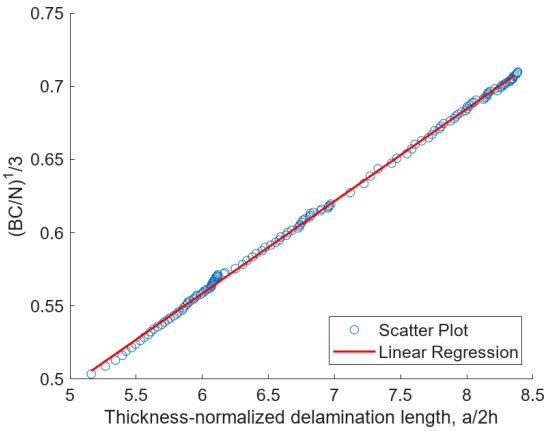

(a) slope m=0.06 C-LMPAEK seq. A

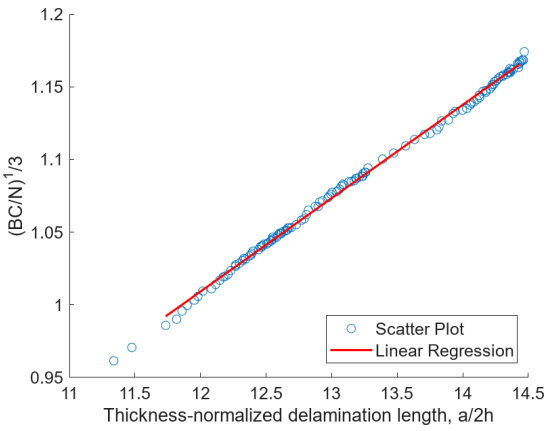

(b) slope m=0.06 C-Epoxy seq. A

Figure 6.8: Plot to determine slope, m

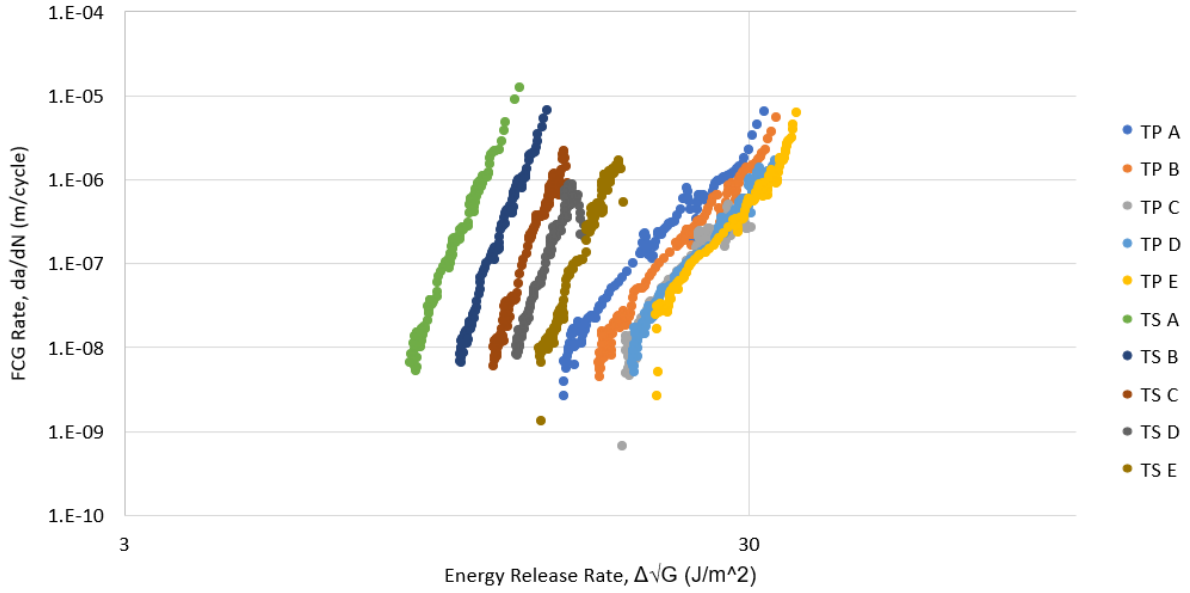

Figure 6.9: Combined FCG curves for both C-Epoxy (TS) and C-LMPAEK (TP)

In Figure 6.9, the plot illustrates all sequences conducted on the LMPAEK and C-Epoxy specimens. The plot exhibits the expected behaviour, with the curves shifting to the right, indicating the influence of fiber bridging. Furthermore, for C-LMPAEK, a clear convergence of the curves on the right side is observed, consistent with patterns identified in existing data. To make this phenomenon visually more clear for the C-Epoxy, more test sequences should be performed.

In Figure 6.9 can be seen that, especially for the curves of Sequence C for C-LMPAEK (TP) and Sequence D for C-Epoxy (TS), scatter is obtained in the beginning of the sequence. This phenomenon is likely attributed to a premature stop in the quasi-static loading procedure.

In Figure 6.12, the fiber bridging that is visually observed at the end of the C-Epoxy test is shown. This image is made using backlighting.

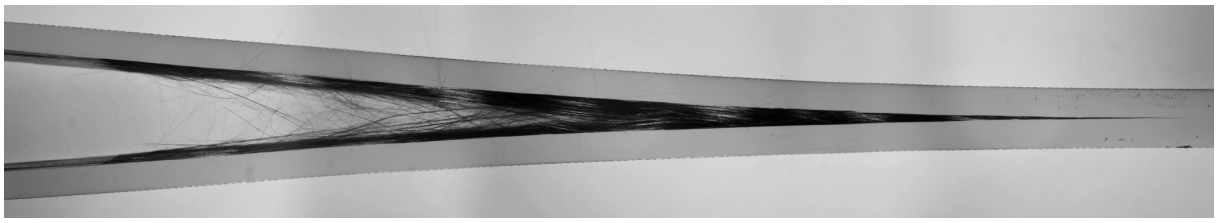

Figure 6.10: Fiber bridging after completion of the test on the C-Epoxy specimen

Next, the single, linear master relation can be obtained for both materials by re-plotting Figure 6.9 using Equation 2.21 in terms of da/dN versus $\left[\frac{\Delta\sqrt{G}-\Delta\sqrt{G_{thr}}}{\sqrt{1-\sqrt{G_{max}}/\sqrt{A}}}\right]$. To establish these linear relationships, specific values for A and $\Delta\sqrt{G_{thr}}$ are chosen. The values chosen for this purpose are given in Appendix J.

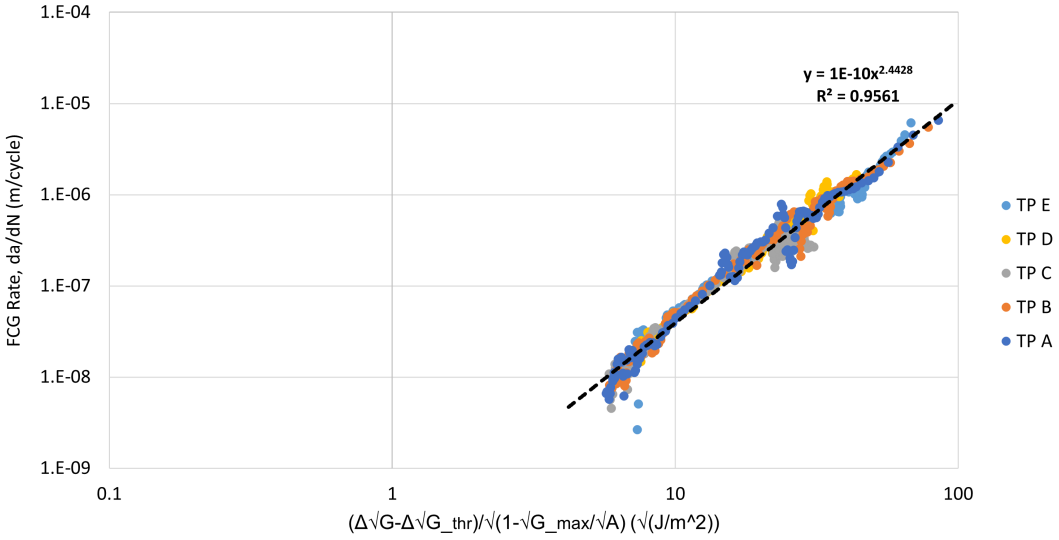

Figure 6.11: Single, linear 'master' relation for C-LMPAEK specimen

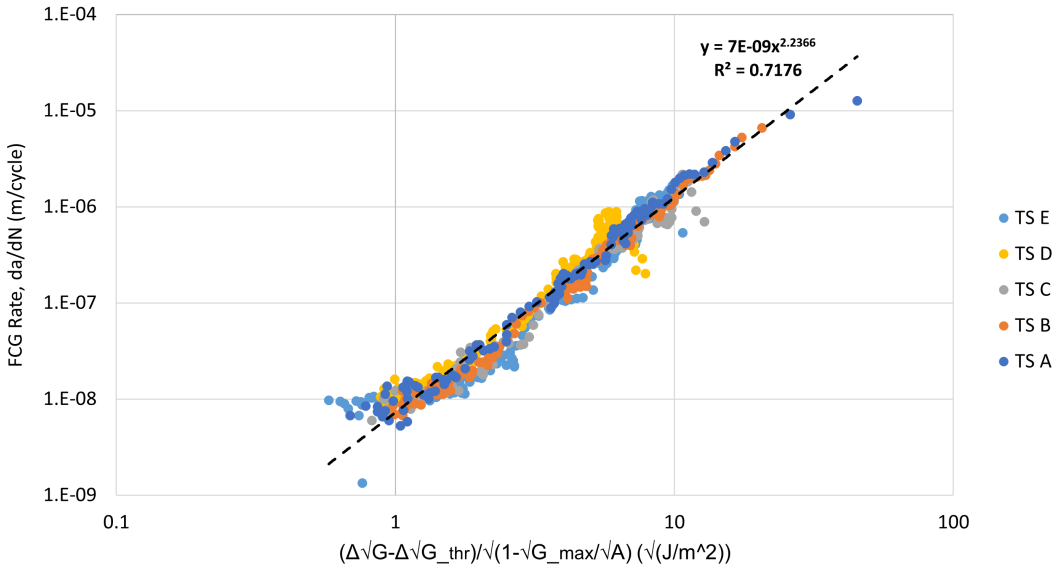

Figure 6.12: Single, linear 'master' relation for C-Epoxy specimen

Since, a lot of tests are already performed on the M30SC/DT120 material by Yao et al. [12, 21, 22, 24–29], as explained in section 2.3.2, these values are used to plot valid 'upper-bound' curves of both 'mean-2sd' and 'mean-3sd'. The values used as input for Equation 2.21 to obtain both 'upper-bound' curves are listed in Table 6.3.

Table 6.3: Upper-bound parameters

Term	Value
D	$1.73 * 10^{-8}$
n	2.22
$\Delta\sqrt{G_{thr}}$ - 2 standard deviations	$4.6\sqrt{J/m^2}$
G_{c0} - 2 standard deviations (where G_{c0} = A_0)	$160 J/m^2$
$\Delta\sqrt{G_{thr}}$ - 3 standard deviations	$2.7\sqrt{J/m^2}$
G_{c0} - 3 standard deviations (where G_{c0} = A_0)	$115 J/m^2$

When these values are inserted in Equation 2.21, the 'upper-bound' curves in Figure 6.13 is obtained. The obtained 'upper-bound' curves encompass and bound the experimental data.

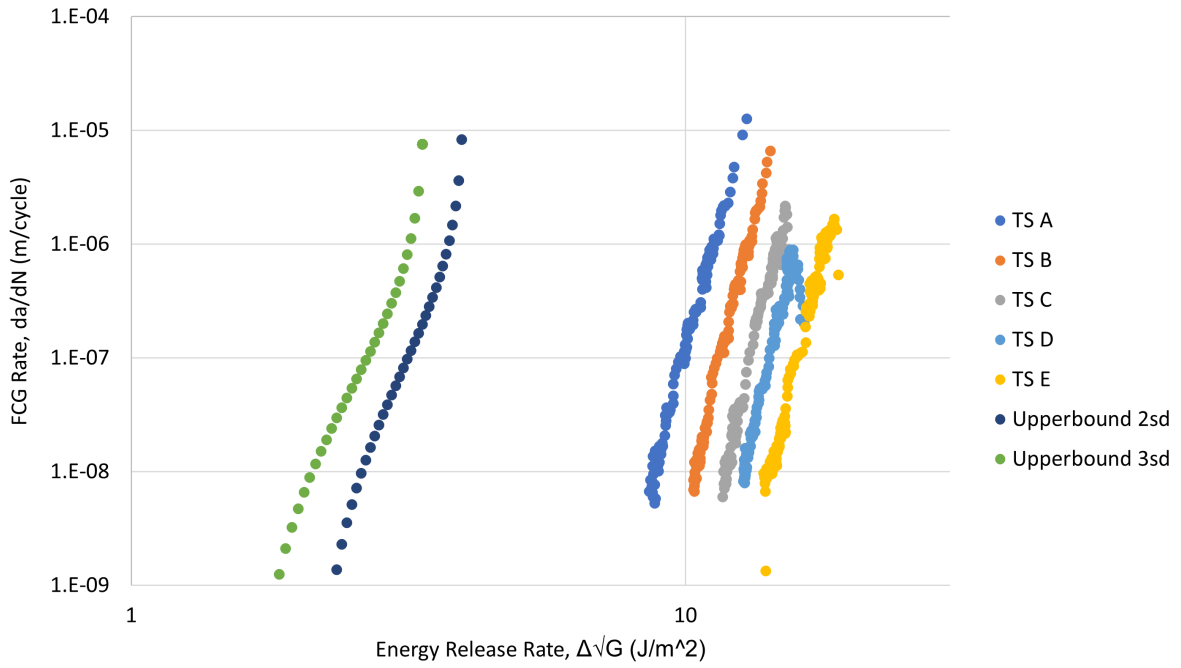

Figure 6.13: Fiber bridging after completion of the test on the C-Epoxy specimen

To obtain a valid 'upper-bound' curve for the LMPAEK material, more tests have to be performed to determine valid values for the input parameters for the 'upper-bound' curve. However, if both linear master relations are plotted in one figure, it is evident that higher mean values for A and $\Delta\sqrt{G_{thr}}$ will be obtained, see Figure 6.14. In Table J.1 in Appendix J, it is shown that indeed higher values for A and $\Delta\sqrt{G_{thr}}$ are used to obtain the linear master relation for C-LMPAEK.

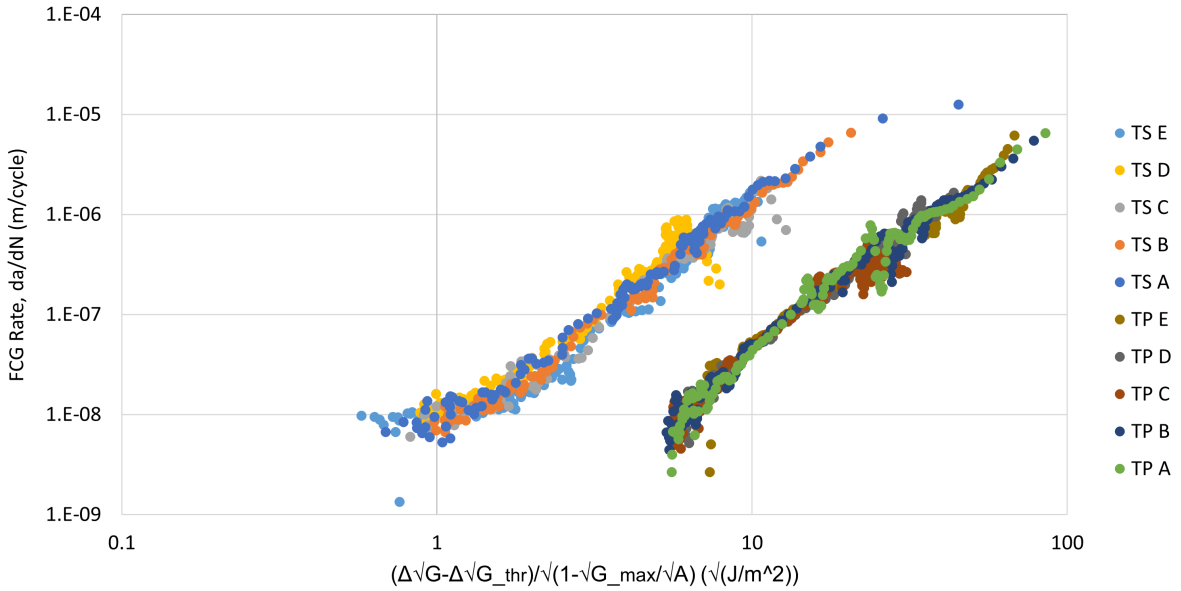

Figure 6.14: Both 'master' relations plotted in one Figure

The force-displacement curves of all sequences can be plotted in one Figure, this is done in Figure 6.15. As can be seen, a similar plot is obtained as Figure 3.3 in Section 3.1.3.

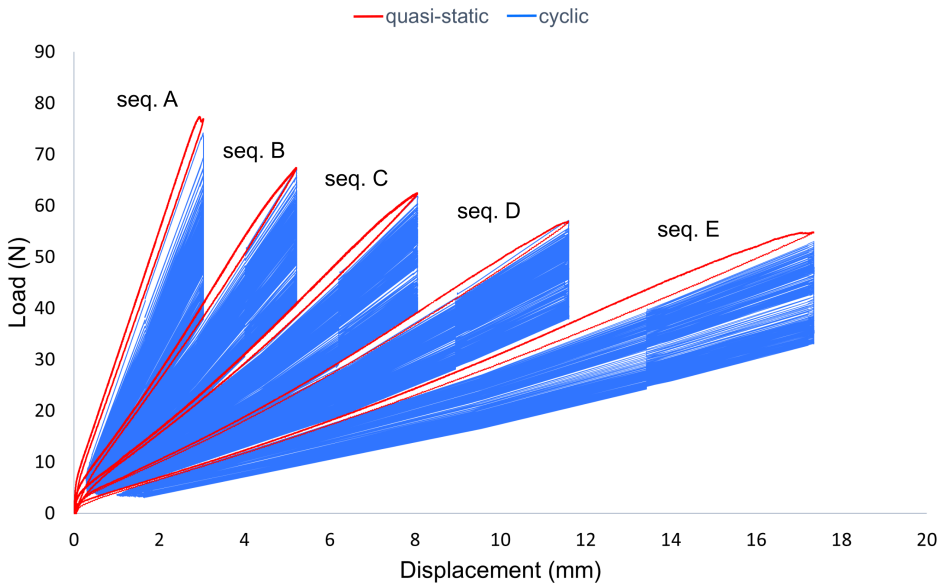

Figure 6.15: The measured force-displacement data from the Instron of all sequences

6.3 Fractography

6.3.1 C-scan

To visualise the geometry of the crack tip within the specimen and to demonstrate what measurement is actually taken, a C-scan was conducted of the LMPAEK specimen. As depicted in Figure 6.16, it is evident that the crack front does not form a straight line across the specimen's width. There is a notable difference in delamination length, approximately $\pm 3mm$, between the sides and the middle of the specimen. This is a significant variation, especially in the context of the precision required for these measurements.

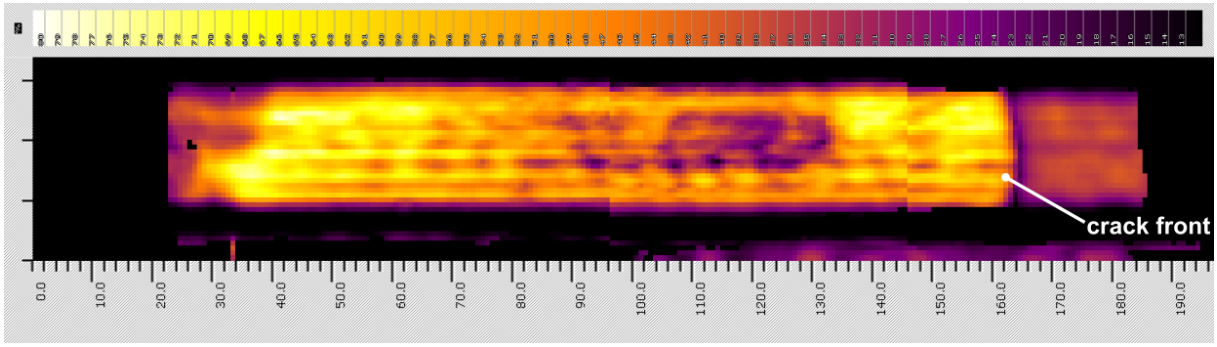

Figure 6.16: C-scan LM-PAEK specimen

6.3.2 SEM

In this section, SEM images of the fracture surfaces of both C-Epoxy (TS) and C-LMPAEK (TP) materials are Analysed. A distinct contrast is evident between the C-LMPAEK and C-Epoxy material. As shown in Figure 6.17, the C-Epoxy material exhibits, no or little plastic deformation, i.e. brittle behaviour. The images suggest that the progression of the crack predominantly occurred along the interface between the fiber and the matrix. The images also indicate poor fiber-matrix adhesion by the observable fiber pull-out and clean fibers.

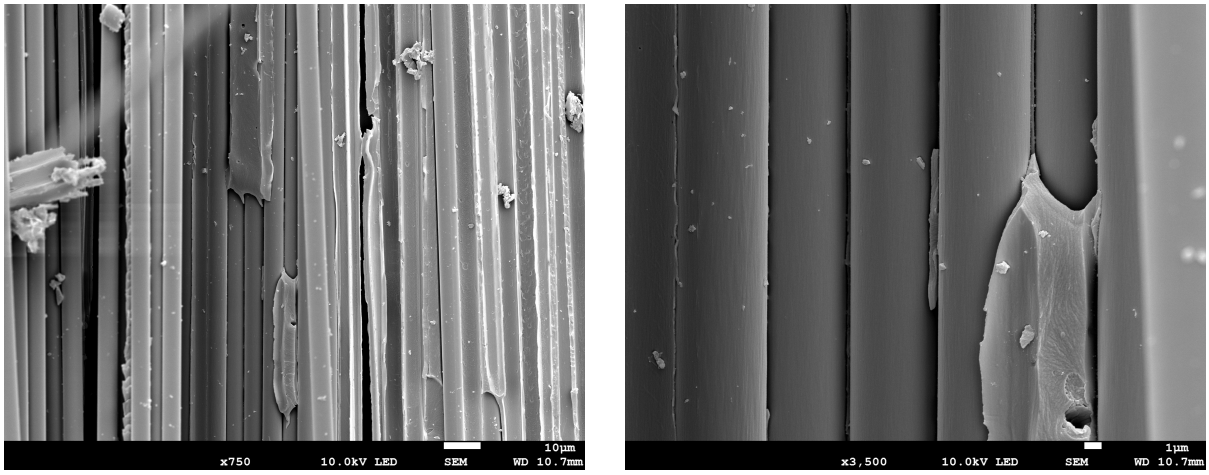

(a) Clean fibers, brittle behaviour (C-Epoxy)

(b) Close up (C-Epoxy)

Figure 6.17: SEM image of the fracture surface of the C-Epoxy material

In Figure 6.18, the C-LMPAEK material exhibits characteristics of ductile fracture. A transition in the fracture surface is observed, shifting from cyclic to quasi-static loading conditions. In the upper section of the image (cyclic loading), the fracture occurs through the matrix material, while in the lower section (quasi-static loading), the fracture path aligns with the fiber/matrix interface. This indicates the varied response of the material to different loading conditions.

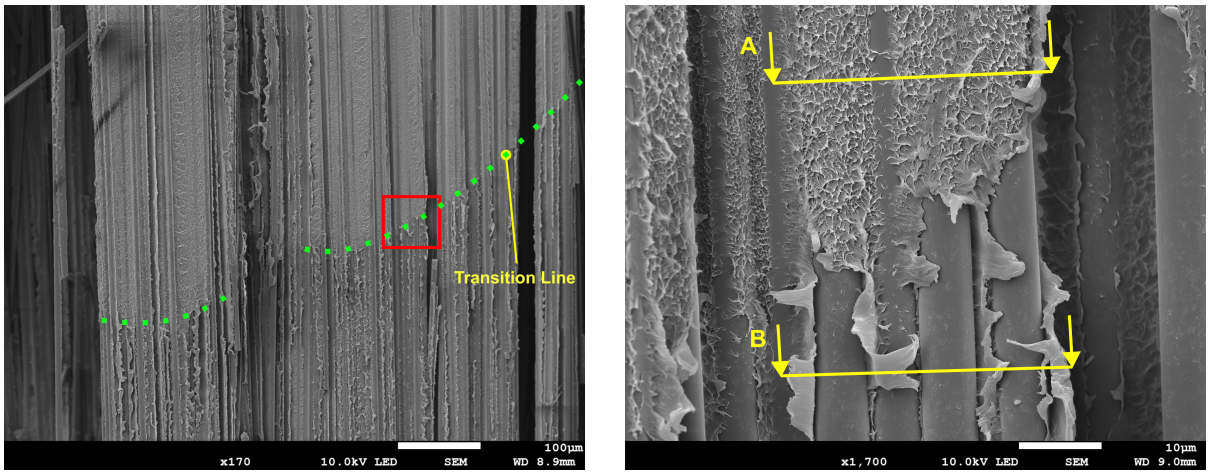

(a) Transition Line (C-LMPAEK) (b) Close up trasition line (C-LMPAEK)

Figure 6.18: SEM image of the fracture surface of the C-LMPAEK material

In Figure 6.19, a schematic representation is provided, illustrating the cross-sections as indicated in Figure 6.18b. The difference between the matrix fracture en the fiber/matrix fracture is here emphasised. In section A, smaller plastic deformation is observed than in section B. In section B, the fibers appear bare and a more significant material flow is observed, highlighting the contrast in the fracture behaviour between the two sections.

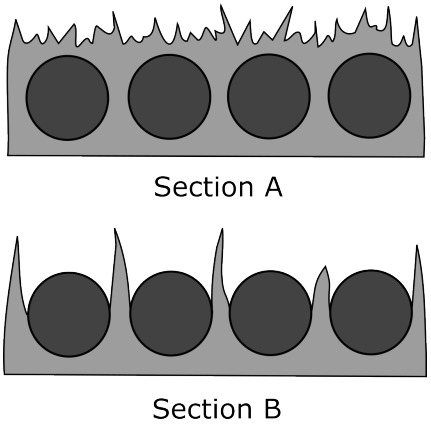

Figure 6.19: Schematic illustration of the cross-sections of cyclic and quasi-static loading areas

7 DISCUSSION

This chapter elaborates on the key findings during the development and testing of the final setup. The discussion also focuses on elements related to the interpretation of the protocol of Alderliesten et al. [8] and challenges that were encountered while conducting the initial experiments.

In this report, the design of an automated measurement system is shown in which the Protocol made by Alderliesten et al. [8], is implemented and automated to obtain Fatigue resistance curves of CFRPs. As shown in the previous chapter, it is possible to automate this process and obtain accurate, repeatable results. However, to determine the final accuracy obtained, more comparative studies have to be performed to make a proper comparison between the accuracy and repeatability of the automated setup against the current manual method described in the protocol. When it is assumed that the systematic error, or bias, is properly compensated, the remaining error of the setup is the random error obtained by the vision program, i.e. $\pm 0.01313mm$. Time was spent to compensate for this distortion using the LabVIEW vision assistant, but this has not increased accuracy so far. Therefore, the compensation which is done by the linear relation obtained in the data analysis afterwards, was chosen to be the most secure solution. However, more research has to be done to check if the bias and perspective error are properly compensated. On the other hand, this automated setup eliminates the operator bias completely, which may lead to significant error in determining the crack tip location.

To validate the measurements taken by the vision program, attempts were made using a digital microscope. However, it was later discovered that this microscope was not properly calibrated, leading to inaccuracies in the validation measurements. As a result, only a limited number of validation measurements could be conducted using an optical microscope. It is important to note that measurements taken with an optical microscope are subject to operator bias which can influence the accuracy of these validation results.

Another point of discussion is the use of the matte white spray paint which is used to enhance the contrast of the crack. Although signs of brittle behaviour of the spray paint was observed under the microscope, it is not assessed if the spray paint is indeed brittle enough to follow the exact crack tip and not crack in front or behind the crack tip location. This phenomenon might potentially lead to an increase in measurement bias. Consequently, it is advised to conduct experiments to determine whether this mechanism introduces any significant error in the measurements. Additionally, the thickness of the paint coating is not regulated. In the case of the M30SC/DT120 specimen, the sides appeared to be rougher compared to the TC1225 LMPAEK specimen, therefore a thicker coating was needed to obtain a flat surface. However, the coating thickness may also have an impact on the measurements.

As can observed in Figure 6.7, there are minor fluctuations in the measured delamination lengths. These variations could be attributed to either the material behaviour or inaccuracies in the crack tip location estimation by the vision program. As a consequence of these fluctuations, the FCG-rate curve, calculated using the 7-point method, also shows major variation. This can be reduced by increasing the number of measurement points and/or increasing the data points

over which the polynomial is fitted to calculate the average da/dN. Implementing these strategies should result in a smoother FCG rate curve. Since the procedure is now automated, this results in a minimal increase in test duration.

A deviation from the protocol is that the specimen is taken out of the fixture once during the testing process. This is necessary to accurately measure delamination length after pre-cracking for sequence A, a_p. This value is then used as a 'base' measurement in the program, to which the subsequent delamination increments, as measured by the vision program, are added. This step is strongly recommended because the vision program faces challenges in precisely determining the delamination increment resulting from the first pre-crack. This difficulty arises because the spray paint tends to accumulate at the edges of the initial delamination made by the insert film, due to surface tension.

Another challenge arising from the protocol is the instance when to stop the pre-cracking, also referred to as the 'quasi-static loading procedure', as explained in Section 6.2.1. Where for sequence A, where the crack is grown for a few millimeters, the curve is a straight line. However, when pre-cracking is stopped at non-linearity, for subsequent sequences, scatter is obtained in the FCG curve. This phenomenon is primarily observed in the C-LMPAEK specimens. However, the plot in Figure 6.9 illustrates that this is also the case for one sequence of the C-Epoxy specimen. the non-linear behaviour of the sequences is probably attributed to compliant behaviour without an increase in delamination. This shows the necessity to first let the crack grow for a small increment before the fatigue cycling is started.

8 CONCLUSION & RECOMMENDATIONS

8.1 Conclusion

The goal of this project was to automate the testing process described in the protocol of Alderliesten et al. [8] of the ESIS TC4 committee. The final setup features a camera system equipped with a vision algorithm developed in LabVIEW. Overall, the final design effectively conducts a Double Cantilever Beam (DCB) tests in accordance with the protocol.

One of the most significant achievements of this automated setup, using the automated optical analysis, is its substantial improvement in time efficiency over the conventional manual method of using a travelling microscope. Based on available data from other labs, a test sequence of $\pm 450,000$ cycles typically required 2-4 days, yielding a mere 8 optically measured data points. The automated setup significantly accelerates this process. With this setup, a test with the same number of cycles can be completed in approximately 24 hours, producing 167 optically measured data points. Furthermore, the involvement of an operator is significantly reduced to only the pre-cracking phase, which is roughly half an hour, thereby enhancing the overall efficiency of the testing procedure.

The implementation of optical analysis technology for measuring delamination length has proven to yield reliable results. The system was rigorously tested on two distinct materials, C-Epoxy (M30SC/DT120) and C-LMPAEK (TC1225 LMPAEK), demonstrating its versatility. The vision algorithm developed, which is enhanced by an iterative approach, exhibits a robust resistance to measurement errors due to surface aberrations or contaminants on the specimen. This technology applies to a broad range of materials without necessitating extensive specimen preparation. Additionally, the simplicity of the hardware setup required for this measuring technique ensures that the system can be easily replicated in other labs.

In terms of accuracy, the automated setup operates well within the required accuracy of $\pm 0.05mm$. Assuming that both the systematic error and the error in the distortion model are effectively compensated, the precision of crack length measurement using this setup can achieve a standard deviation of $\pm 0.01313mm$. However, it remains challenging to conclusively determine if this method offers improved accuracy over existing manual measurement techniques. To ascertain this, further measurement validations and adjustments are recommended to ensure that errors are indeed effectively compensated and that the accuracy and repeatability of the measurements are reliably quantified. Once the accuracy and repeatability are thoroughly assessed, these results can then be compared with those from the Round Robin test to confidently evaluate whether this automated system offers a more precise alternative to current manual methods. A significant advantage of this automated system is the elimination of operator bias from the test data, making it an ideal tool for comparing the performance of different materials.

By automating the load ratio control, the operator dependency is further reduced. Where first, the operator had to manually adjust the minimum displacement value, δ_{min}, for the cyclic loading at several time intervals. The setup now calculates the applied load ratio for every cycle and

adjusts δ_{min} accordingly. Through the integration of communication via email and the online dashboard, the operator has the flexibility to engage in other tasks while the fatigue test is running.

The procedure necessitates minor adjustments in the protocol to enhance accuracy, precision and reproducibility across different tests. Firstly, it is recommended to utilize a microscope for measuring the initial pre-crack increment for sequence A. This step ensures an accurate determination of the value of a_p, as it serves as the base value for subsequent measurements. Secondly, for more ductile materials such as C-LMPAEK, it is crucial to allow a slight extension of the crack during the quasi-static loading process, also referred to as the 'pre-cracking process', before initiating cyclic fatigue loading. This adjustment guarantees the onset of delamination from the beginning of the fatigue test, leading to a consistent linear Fatigue Crack Growth (FCG) curve rather than one with inherent scatter at the start. The increment due to this pre-cracking procedure must be measured and added to the total delamination length, this measurement can be facilitated by a specialised LabVIEW tool called 'Live Tester'. Given the likelihood of similar occurrences in other ductile materials, incorporating this 'pre-cracking' step into the protocol for all materials is advisable. Moreover, a clearer guideline for when to stop the quasi-static loading procedure would ensure more reliability in the test results across various materials.

8.2 Recommendations

In the course of this project, several areas have been identified that could benefit from further improvement or require additional attention. This section summarises these key points, providing a foundation for directions in future work.

- During testing of the first thermoplastic specimens, it was observed that, in some cases, the crack did not propagate effectively at the beginning of the fatigue sequence. It was observed that increasing the length of the pre-crack resolved this issue. A similar observation was done during one sequence of the M30SC/DT120 material, where the pre-cracking might have been stopped prematurely. Consequently, it is essential to more clearly define the point at which to stop pre-cracking in the protocol. This clarification will help ensure consistency and repeatability in the test data.
- Throughout this project, an assumption was made that da (the change in crack length) is equivalent to dx (the change in the horizontal direction) for calculating the FCG rate, da/dN. The protocol did not specifically address this conversion, and it is likely that other participants in the Round Robin test also used dx for their calculations. However, geometrically, there is a minor difference between these two values. While this difference is presumed to be negligible, confirming its insignificance requires a more detailed calculation. This calculation should also account for the compliant behaviour of the specimen, ensuring a comprehensive assessment of the impact of this discrepancy.
- Experimental observations suggest that radial and tangential distortions have been effectively compensated. However, to further enhance the accuracy of the distortion model, it is recommended to account for the remaining perspective error using LabVIEW. Currently, this perspective error is corrected during data analysis with the MATLAB code. Automating this could involve more in-depth research into the internal and external parameters of the camera. By only using the designated LabVIEW VI's instead of LabVIEW's Vision Assistant, the lens distortion parameters may be adjustable. Additionally, by eliminating the use of the Vision Assistant, the program's processing speed could be improved.
- To ascertain the accuracy of the vision program, further validation is advisable. One method involves using a calibrated digital microscope to measure the distance from a

reference point, e.g. a scratch on the coating, to the crack tip. This measurement can then be replicated by the vision program and the 'Pixel to Real World Coordinate' function from LabVIEW which is implemented in the 'Live Tester' program. In this way, the accuracy of the program can be more precisely determined and possible bias that is left in the system can be identified and corrected.

REFERENCES

[1] M J Suriani, Hannah Zalifah Rapi, R A Ilyas, Michal Petrů, Petr˚ Petrů, S M Sapuan, and Antonio Balart Gimeno. Delamination and Manufacturing Defects in Natural Fiber-Reinforced Hybrid Composite: A Review. *Polymers*, 2021.

[2] E. Oterkus, C. Diyaroglu, D. De Meo, and G. Allegri. Fracture modes, damage tolerance and failure mitigation in marine composites. *Marine Applications of Advanced Fibre-Reinforced Composites*, pages 79–102, 1 2016.

[3] O. Al-Khudairi, H. Hadavinia, A. Waggott, E. Lewis, and C. Little. Characterising mode I/mode II fatigue delamination growth in unidirectional fibre reinforced polymer laminates. *Materials and Design*, 66(PA):93–102, 2 2015.

[4] Brian L.V. Bak, Carlos Sarrado, Albert Turon, and Josep Costa. Delamination under fatigue loads in composite laminates: A review on the observed phenomenology and computational methods, 11 2014.

[5] ISO15024 - Fibre-reinforced plastic composites - Determination of mode I interlaminar fracture toughness GIC for UD reinforced materials. Technical report, 2001.

[6] ASTM D 5528 - 01 -Standard Test Method for Mode I Interlaminar Fracture Toughness of Unidirectional Fiber-Reinforced Polymer Matrix Composites 1. Technical report, 2001.

[7] ASTM D6115 - 97: Standard Test Method for Mode I Fatigue Delamination Growth Onset of Unidirectional Fiber-Reinforced Polymer Matrix Composites 1.

[8] René Alderliesten and Andreas J Brunner. Determination of Mode I Fatigue Delamination Propagation in Unidirectional Fibre-Reinforced Polymer Composites Test Protocol. Technical report.

[9] Matúš Turis and Oľga Ivánková. Using finite element analysis to obtain plastic zones in the vicinity of the crack edges, under mixed mode loading conditions. *MATEC Web of Conferences*, 310:00028, 2020.

[10] R. Jones, A. J. Kinloch, J. G. Michopoulos, A. J. Brunner, and N. Phan. Delamination growth in polymer-matrix fibre composites and the use of fracture mechanics data for material characterisation and life prediction. *Composite Structures*, 180:316–333, 11 2017.

[11] J. A. Pascoe, R. C. Alderliesten, and R. Benedictus. Methods for the prediction of fatigue delamination growth in composites and adhesive bonds - A critical review. *Engineering Fracture Mechanics*, 112-113:72–96, 11 2013.

[12] Liaojun Yao, R. C. Alderliesten, R. Jones, and A. J. Kinloch. Delamination fatigue growth in polymer-matrix fibre composites: A methodology for determining the design and lifing allowables. *Composite Structures*, 196:8–20, 7 2018.

[13] T.L. Anderson. *Fracture Mechanics: Fourth Edition Fundamentals and Applications*. 2017.

[14] R. Jones, S. Pitt, A. J. Bunner, and D. Hui. Application of the Hartman-Schijve equation to represent Mode I and Mode II fatigue delamination growth in composites. *Composite Structures*, 94(4):1343–1351, 3 2012.

[15] C T Lin and P W Kao. Fatigue delamination growth in carbon fibre-reinforced aluminium laminates. *Composites Part A*, 2:9–15, 1996.

[16] Gretchen B Murri. Evaluation of Delamination Onset and Growth Characterization Methods under Mode I Fatigue Loading. Technical report, Langley Research Center, Hampton, Virginia, 2013.

[17] R. Jones, A. J. Kinloch, and W. Hu. Cyclic-fatigue crack growth in composite and adhesively-bonded structures: The FAA slow crack growth approach to certification and the problem of similitude. *International Journal of Fatigue*, 88:10–18, 7 2016.

[18] Rafiullah Khan, Rene Alderliesten, Saeed Badshah, and Rinze Benedictus. Effect of stress ratio or mean stress on fatigue delamination growth in composites: Critical review, 6 2015.

[19] S. Stelzer, A. J. Brunner, A. Argüelles, N. Murphy, G. M. Cano, and G. Pinter. Mode I delamination fatigue crack growth in unidirectional fiber reinforced composites: Results from ESIS TC4 round-robins. *Engineering Fracture Mechanics*, 116:92–107, 1 2014.

[20] A. J. Brunner, N. Murphy, and G. Pinter. Development of a standardized procedure for the characterization of interlaminar delamination propagation in advanced composites under fatigue mode I loading conditions. *Engineering Fracture Mechanics*, 76(18):2678–2689, 12 2009.

[21] Liaojun Yao. *Mode I fatigue delamination growth in composite laminates with fibre bridging*. PhD thesis, Technische Universiteit Delft, Delft, 2015.

[22] Liaojun Yao, Yi Sun, Licheng Guo, Liyong Jia, and Meiying Zhao. A validation of a modified Paris relation for fatigue delamination growth in unidirectional composite laminates. *Composites Part B: Engineering*, 132:97–106, 1 2018.

[23] Rhys Jones and Anthony J. Kinloch. A way forward for industry to determine valid cyclic-fatigue relationships for polymer-matrix fibre composites. In *Procedia Structural Integrity*, volume 28, pages 26–38. Elsevier B.V., 2020.

[24] Liaojun Yao, René Alderliesten, Meiying Zhao, and Rinze Benedictus. Bridging effect on mode i fatigue delamination behavior in composite laminates. *Composites Part A: Applied Science and Manufacturing*, 63:103–109, 2014.

[25] Liaojun Yao, R. C. Alderliesten, Meiying Zhao, and R. Benedictus. Discussion on the use of the strain energy release rate for fatigue delamination characterization. *Composites Part A: Applied Science and Manufacturing*, 66:65–72, 2014.

[26] Liaojun Yao, R. C. Alderliesten, and R. Benedictus. The effect of fibre bridging on the Paris relation for mode I fatigue delamination growth in composites. *Composite Structures*, 140:125–135, 4 2016.

[27] Liaojun Yao, Yi Sun, Licheng Guo, Meiying Zhao, Liyong Jia, R. C. Alderliesten, and R. Benedictus. A modified Paris relation for fatigue delamination with fibre bridging in composite laminates. *Composite Structures*, 176:556–564, 9 2017.

[28] Liaojun Yao, Yi Sun, Licheng Guo, R. C. Alderliesten, R. Benedictus, Meiying Zhao, and Liyong Jia. Fibre bridging effect on the Paris relation of mode I fatigue delamination in composite laminates with different thicknesses. *International Journal of Fatigue*, 103:196–206, 10 2017.

[29] Liaojun Yao, R. C. Alderliesten, and R. Benedictus. Interpreting the stress ratio effect on delamination growth in composite laminates using the concept of fatigue fracture toughness. *Composites Part A: Applied Science and Manufacturing*, 78:135–142, 11 2015.

[30] ISO 5893 - Rubber and plastics test equipment: Tensile, flexural and compression types (constant rate of traverse): Specification. Technical report, 2019.

[31] ASTM E647 - 00: Standard Test Method for Measurement of Fatigue Crack Growth Rates 1. Technical report, 2000.

[32] Y. Si, J. P. Rouse, and C. J. Hyde. Potential difference methods for measuring crack growth: A review. *International Journal of Fatigue*, 136, 7 2020.

[33] J. van de Zand. Automated Double Cantilever Beam test system: Applied in fracture toughness determination of CF/PEI composites. Technical report, Universiteit Twente, 2010.

[34] F. Pegorin, K. Pingkarawat, and A. P. Mouritz. Electrical-based delamination crack monitoring in composites using z-pins. *Composites Part A: Applied Science and Manufacturing*, 104:120–128, 1 2018.

[35] Jesse J.A. van Kuijk, René C. Alderliesten, and Rinze Benedictus. Measuring crack growth and related opening and closing stresses using continuous potential drop recording. *Engineering Fracture Mechanics*, 252, 7 2021.

[36] Chr Fischer and F J Arendts. ELECTRICAL CRACK LENGTH MEASUREMENT AND TEMPERATURE DEPENDENCE OF THE MODE I FRACTURE TOUGHNESS OF CARBON FIBRE REINFORCED PLASTICS THE. *Composites Science and Technology*, 46:319–323, 1993.

[37] S Yarlagadda, Nat Hager, A Abuobaid, and M K Yoon. An Automated Technique for Measuring Crack Propagation during Mode I DCB Testing Armor protectected antennas View project Functionally Designed Ultra-lightweight Carbon Fiber Reinforced Thermoplastic Composites Door Assembly View project An Automated Technique for Measuring Crack Propagation during Mode I DCB Testing. Technical report.

[38] B. Krull, J. Patrick, K. Hart, S. White, and N. Sottos. Automatic Optical Crack Tracking for Double Cantilever Beam Specimens. *Experimental Techniques*, 5 2015.

[39] Yan Zhao, Dianyin Hu, Qicheng Liu, Rongqiao Wang, and Jianguang Bao. High resolution and real-time measurement of 2D fatigue crack propagation using an advanced digital image correlation. *Engineering Fracture Mechanics*, 268, 6 2022.

[40] A. Khudiakova, V. Grasser, C. Blumenthal, M. Wolfahrt, and G. Pinter. Automated monitoring of the crack propagation in mode I testing of thermoplastic composites by means of digital image correlation. *Polymer Testing*, 82, 2 2020.

[41] Sujit Kuthirummal, Hajime Nagahara, Changyin Zhou, and Shree K. Nayar. Flexible depth of field photography. *IEEE Transactions on Pattern Analysis and Machine Intelligence*, 33(1):58–71, 2011.

[42] Juyang Weng, Paul Cohen, and Marc Herniou. Camera Calibration with Distortion Models and Accuracy Evaluation. *IEEE TRANSACTIONS ON PATTERN ANALYSIS AND MACHINE INTELLIGENCE*, 14(10), 1992.

[43] Olgierd Stankiewicz, Gauthier Lafruit, and Marek Domański. Multiview video: Acquisition, processing, compression, and virtual view rendering. In *Academic Press Library in Signal Processing: Image and Video Processing and Analysis and Computer Vision*, volume 6, pages 3–74. Elsevier, 2018.

[44] Measurements and Error Analysis. Technical report, Advanced Instructional Systems, Inc. and University of North Carolina, 2011.

[45] Oleksandr Semeniuta. Analysis of Camera Calibration with Respect to Measurement Accuracy. In *Procedia CIRP*, volume 41, pages 765–770. Elsevier B.V., 2016.

[46] JCGM 100:2008 - Evaluation of measurement data — Guide to the expression of uncertainty in measurement. Technical report, 2008.

[47] Thomas M Adams. G104 - A2LA Guide for Estimation of Measurement Uncertainty In Testing. Technical report, 2002.

[48] ASTM E2309 - 20: Standard Practices for Verification of Displacement Measuring Systems and Devices Used in Material Testing Machines 1.

A PROTOCOL PROPOSED BY ALDERLIESTEN ET AL.

Determination of Mode I Fatigue Delamination Propagation in Unidirectional Fibre-Reinforced Polymer Composites

Test Protocol

René Alderliesten
Structural Integrity & Composites, Aerospace Materials and Structures, Faculty of Aerospace Engineering, Delft University of Technology, The Netherlands
Tel. +31(0)15 278 5492 / Fax +31(0)15 278 1151 / r.c.alderliesten@tudelft.nl

Andreas J. Brunner
Empa, Switzerland
Tel. +41 58 765 4493/ Fax +41 58 765 11 22 / andreas.brunner@empa.ch

Introduction

To characterise the mode-I (tensile opening) delamination behaviour of fibre reinforced polymer composites, standard test methods are available for determining the quasi-static fracture toughness (ISO 15024) and the fatigue delamination onset (ASTM D 6115). These standard test methods, however, do not cover the fatigue delamination propagation behaviour, which is required for the purpose of design and reliability assessment. Development of standard test methods appropriate for determination of design values is hindered, because of the contribution of large-scale fibre bridging, often observed in fatigue delamination testing of unidirectional laminates. The amount of fibre-bridging occurring in structural applications will depend on the laminate lay-up, but also, to some extent on the loading mode. For design, a "conservative" value is desirable, and hence, quantification of the effects of fibre-bridging on delamination propagation in unidirectional laminates would allow for estimating the intrinsic delamination resistance of this laminate. Together with consideration of the scatter, an intrinsic design limit could be established, satisfying the safety factor requirements defined in design guidelines.

The procedure presented here uses the Double Cantilever Beam (DCB) specimen in a tensile test machine capable of applying cyclic displacements of constant amplitude at a constant frequency in the range between 1 and 10 Hz and specifies an experimental procedure to quantify and exclude the contribution of large-scale fibre bridging in mode I fatigue fracture tests of unidirectionally fibre-reinforced plastic composites.

This test procedure comprises multiple sequences per specimen, to enable the derivation of a zero-bridging delamination resistance curve via regression through and translation of all data. This test procedure is a modification and extension of a former test procedure [1], but also incorporates an analysis based on a modified Hartman-Schijve equation for the determination of scatter in the fatigue fracture curves (essentially da/dN versus a "$\sqrt{\Delta G}$" related quantity instead of the "conventional" Paris-equation correlating da/dN with ΔK or ΔG).

The procedure is a development of that published by ESIS (the European Structural Integrity Society), Technical Committee 4, Polymers and Composites [2] who carried out the preliminary enabling research through a series of round-robin exercises conducted between 2009 and 2020.

NOTE: Special structural designs of fibre-reinforced composites with significant amounts of fibres aligned in a single direction may rely on fibre-bridging for ensuring structural integrity under cyclic service loads. One example for this are wind-rotor blades.

1. Scope

This International Standard specifies a method for the determination of delamination propagation curves (average delamination increment per cycle da/dN on a logarithmic scale) as a function of applied mode I strain energy release rate G_I (or a quantity proportional to $\sqrt{G_I}$, also on a logarithmic scale) for unidirectional fibre-reinforced plastic composites using the Double Cantilever Beam (DCB) specimen and test apparatus. It is applicable to unidirectional carbon-fibre and glass-fibre reinforced thermosets and thermoplastics. The scope is not necessarily limited to these fibres and lay-ups, but for laminates with other types of fibres or lay-ups, no recommendations for specimen dimensions and fibre volume content are currently available.

2. Normative references

The following documents, in whole or in part, are normatively referenced in this document and are indispensable for its application. For dated references, only the edition cited applies. For undated references, the latest edition of the referenced document (including any amendments) applies.

ISO 291, Plastics — Standard atmospheres for conditioning and testing
ISO 5893, Rubber and plastics test equipment — Tensile, flexural and compression types (constant rate of traverse) — Specification
ISO 15024, Fibre-reinforced plastic composites — Determination of mode I interlaminar fracture toughness, GIC, for unidirectionally reinforced materials

3. Symbols and abbreviated terms

a, a_0, a_p, Δa, (various delamination lengths) a measured delamination length or total crack length, distance between the load-line (intersection of the plane through the pin-hole centre of the load-block normal to the specimen width and the plane of delamination) and the tip of the delamination on the edge of the specimen (see Figure 1) / a_0 = initial delamination length, measured from the load-line to the tip of the insert film (see Figure 1) / a_p precrack length, the length between the load-line and the tip of the precrack formed in during the precracking step prior to any cyclic fatigue fracture measurements being taken / Δa delamination increment

A (fitting parameter Hartman-Schijve)

B (specimen width DCB, see ISO 15024)

C compliance δ/P of the specimen

C_{max} compliance of the specimen at maximum load

C_0 initial compliance of the specimen neglecting start-up effects, e.g. due to play in the specimen fixture

C (fitting parameter Paris) (*maybe change, since C is also used for Compliance and compliance correction*)

cycle smallest segment of a load-time or stress-time function which is repeated periodically(copied fromISO 15850)

D (fitting parameter Hartman Schijve)

DCB Double Cantilever Beam (specimen)

F (large displacement correction DCB, see ISO 15024)

G, GIC, Gthr, GImax, GImin (various energy release rates)

2h total thickness of the specimen (thickness of each specimen arm is h)

H height of the load-block

l_1 distance between the centre of the loading pin and the mid-plane of the specimen beam to which the load-block is attached (see Figure 5), i.e. equal to (H + h)/2 if the pin hole is through the centre of the block (*copied from ISO 15024*)

l_2 distance between the centre of the loading pin and the edge of the load block, measured towards the tip of the insert (starter film) or the tip of the mode I precrack (see Figure 5), i.e. equal to l3/2 if the pin hole is through the centre of the block (*copied from ISO 15024*)

l_3 length of the load-block (see Figure 5) (*copied from ISO 15024*)

L (total length of specimen DCB, defined as l in ISO 15024)

LEFM Linear Elastic Fracture Mechanics

m (fitting exponent Paris)
N (load block correction DCB, see ISO 15024) (maybe change, N is also used as number of cycles)
N number of cycles completed in fatigue fracture loading
NL, vis, 5%/MAX points (necessary or not?)
P, P_{max}, P_{min} (machine load, maximum and minimum load, respectively)
R (stress-ratio in load controlled cyclic fatigue fracture test) defined as P_{min}/P_{max}
R_d (displacement-ratio in displacement controlled fatigue fracture test)
R-curve (resistance curve)
β (fitting exponent Hartman-Schijve)
δ displacement of the cross-head of the testing machine (load-line displacement DCB)
ΔG, $\sqrt{\Delta G}$, (various G-related quantities) (do not use $\Delta\sqrt{G}$ notation, since it could be misunderstood in terms of dimensional analysis)
ΔK difference between maximum and minimum applied stress intensity factor (K_{max} and K_{min}, respectively)

4. Principle

This procedure specifies a method for the determination of delamination propagation curves (presented as average delamination length increment per applied cycle versus a quantity proportional to the square-root of the applied energy release rate in a double-logarithmic plot) under cyclic displacement of constant amplitude and at constant frequency using a Double Cantilever Beam (DCB) specimen. The aim of the method is to characterize delamination propagation and possibly propagation thresholds for unidirectional fibre-reinforced plastic composites. Since this lay-up will result in significant large-scale fibre-bridging in the test, a step-wise loading procedure is introduced that, by regression, allows for establishing a delamination propagation curve and its related scatter that is not affected by fibre-bridging for determination of a safe design limit.

5. Apparatus

5.1 Test machine

5.1.1 General

The tensile-testing machine shall comply with ISO 5893 and the requirements given ***in 5.1.2 to 5.1.5***.

5.1.2 Speed of testing

The test machine shall be capable of maintaining the cyclic constant amplitude and constant frequency displacement rate required ***in 9.2.1 and 9.3.1***, as specified in ISO 5893.

5.1.3 Fixture

The test machine shall be equipped with a fixture to introduce the load to the pins inserted into the load blocks or with grips to hold the piano hinges. In each case, rotation of the specimen end shall be allowed. The axis of the load-introduction fixtures shall be aligned with the loading axis of the test machine.

5.1.4 Load and displacement measurements

The load cell shall be calibrated and shall have a maximum permissible error of ± 1 % of the indicated value. For unidirectional carbon or glass fibre reinforced plastic composites, it is recommended to use a load cell of maximum capacity of 250 N or a load cell of higher capacity, calibrated to the

maximum permissible error in the range up to 200 N. The error in the displacement measurement, normally taken from cross--head movements corrected for any significant loading-train deflection, shall be no greater than ± 1 % of the indicated value. The load and displacement measurement recording shall be capable of recording minimum and maximum loads and displacements, respectively for each cycle at the applied test frequency.

6. Test Specimens

Double Cantilever Beam (DCB) specimens according to ISO 15024 with load blocks or piano hinges should be used (Figure 1). Differing from ISO 15024 the length of the insert should be shorter, so that the distance of the initial delamination after pre-cracking from the load line is not more than 30 mm. The specimen length should be at least 200 mm, to allow the generation of multiple curves per specimen. Moreover the thickness of the laminates may be enhanced compared to ISO 15024 in order to reduce specimen compliance. These modifications guarantee that the load line displacement values do not become too high. To make the delamination more visible during testing, it is recommended to polish the sides of DCB specimen with sand-paper and mark the location of the end of the insert, i.e. the location of delamination front, with the microscope. Subsequently, the sides of the specimens should be lightly coated with a water based, brittle white typewriter correction fluid. A strip of grid paper (with the precision of 1mm) is recommended to be pasted on the specimen side to aid in measuring the delamination propagation.

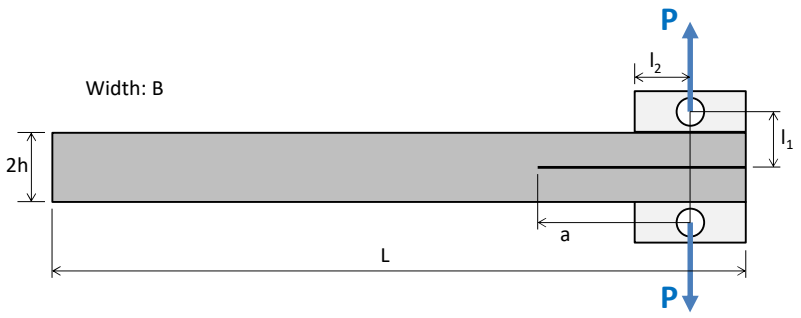

Figure 1 Double Cantilever Beam (DCB) specimen with load blocks

7. Test Procedure

The test under mode I loading should be performed at a frequency of maximum 5 Hz. Before carrying out the test, the specimen dimensions should be checked according to ISO 15024; width B and thickness 2h should be measured at least three evenly distributed points along the length.

When a delamination grows at a constant cyclic displacement, both the cyclic strain energy release rate G_I and the delamination growth rate, da/dN, will decrease in displacement control. Thus, the tests should be started at an initial G_{Imax} just less than the corresponding G_{Ic} of a given crack length (note that this value is not constant in case of fibre bridging). In order to determine the necessary displacement values and for the purpose of creating a natural crack front, the quasi-static mode I test for pre-cracking should be done as a G_{Ic} - test as described in ISO 15024 at a loading rate of 1 mm/min (for unloading a rate of 5 mm/min should be used); with the condition that loading is

stopped immediately once crack propagation is observed, limiting the initial crack length to less than 3 mm.

The displacement value at which pre-cracking stopped, can be taken as the d_{max} value for fatigue loading (Figure 2). The corresponding minimum displacement d_{min} follows from the selected displacement ratio $R_d = d_{min}/d_{max}$ which initially may be taken equal to the load ratio $R = P_{min}/P_{max}$. The minimum load or displacement after pre-cracking should be determined in the unloading cycle from the load displacement readings. After this the cyclic test should be started.

Because the displacement ratio R_d is not equal to the load ratio R it is recommended to read real time the maximum and minimum force throughout the first 250-300 cycles. If the load ratio R deviates more than 10% of the required load ratio, the minimum displacement can be adapted to maintain the required load ratio. Throughout the remainder of the test, the maximum and minimum load should be read at intervals to adjust the minimum displacement once the ratio deviates by more than 10%.

The fatigue tests should be continued until a crack growth rate of about 10^{-8} mm/cycle is reached. This can be achieved when terminating the test once there is no crack extension observed within 50000 to 100000 cycles.

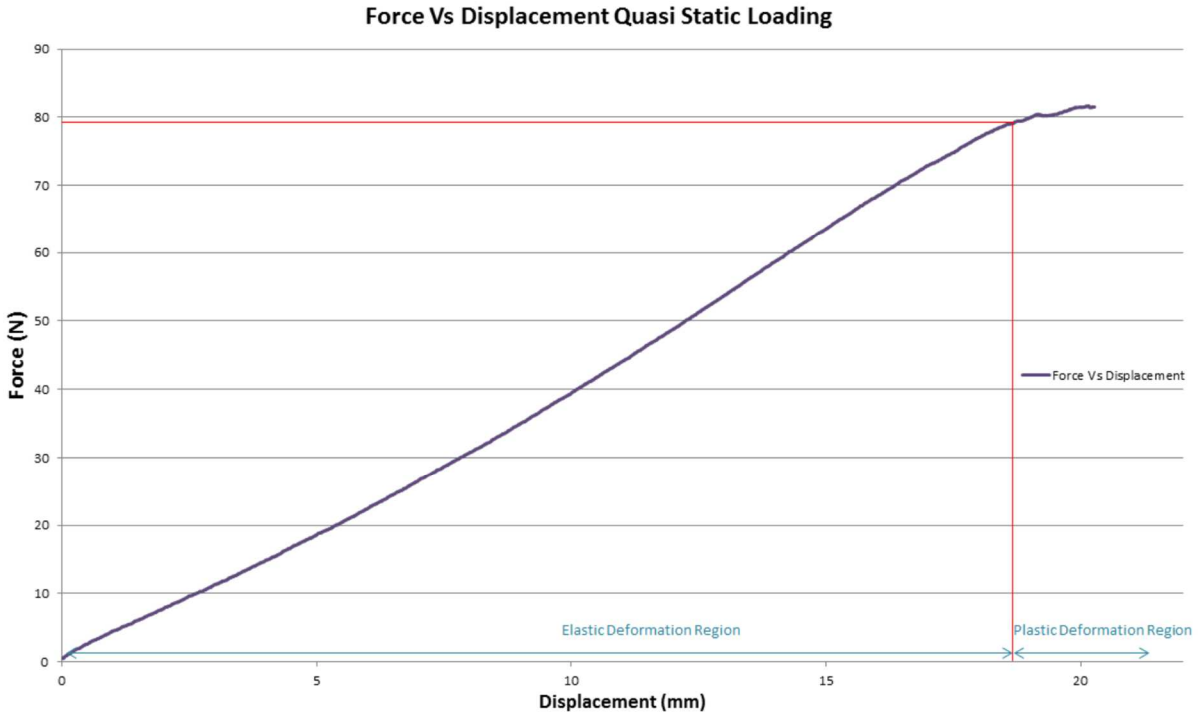

Figure 2 Determination of maximum displacement in force versus displacement from quasi-static loading: loading stops right after non-linearity in force displacement curve is observed avoiding quasi-static growth of the crack. Note that d_{min} should be taken from the load-displacement readings during unloading

Then the quasi-static loading procedure is repeated to determine the new maximum displacement value d_{max} (and corresponding d_{min} measured in the unloading cycle), with this condition that the loading is terminated immediately once non-linearity in the load-displacement curve is observed. One should avoid obvious crack extension under quasi-static loading. In order to avoid obvious crack extension during this process, the operator is recommended to zoom in and carefully monitor the upper part of the load-displacement. This makes it easier to determine whether the load-displacement curve becomes nonlinear.

Subsequently, the cyclic test is performed again until a crack growth rate of about 10^{-8} mm/cycle is reached. This sequence of quasi-loading and cyclic testing is repeated until the load line displacement values have become too high for the test machine, or when subsequent delamination resistance curves coincide with each other (Figure 5).

8. Data Acquisition

Take a set of data readings (minimum and maximum load, minimum and maximum load-line displacement, cycle counter) for each instant of reading delamination lengths. Delamination length reading may be done either using an optical microscope with a magnification of no greater than 70×, a travel range of 0 to 100mm (to accommodate the multiple sequences) and readable to 0.05mm, or using camera recordings. Camera recordings must be performed with camera position and lighting fixed throughout the entire test with multiple test sequences. The entire delamination range of 0 to 100mm must be in view, while the camera resolution must be sufficiently high to measure delamination to 0.05mm. If image quality and resolution must be improved to meet this level, one may consider placing the camera closer to the specimen, to have at least the entire delamination range of one test sequence in view, i.e. range of about 20 to 25 mm.

The load line displacement can be determined from the machine displacement or by using a separate extensometer. Reading delamination lengths should be done without stopping the test; short stops at minimum and maximum load, however, will have negligible effect on the test. These data points are also necessary for generating the calibration equation of the Modified Compliance Calibration (MCC) method.

The recommended stop interval in displacement controlled tests is every 100 cycles in the first 5000 cycles, 500 cycles in the following 15000 cycles, after which, the interval can be determined as 1000 or 2000 cycles, or even larger (but no more than 5000 cycles).

Additionally take sets of data readings after each set of a pre-determined number of cycles (e.g., 500 or 1000). With this data additional delamination lengths can be computed from the compliance data by using the calibration equation of the Modified Compliance Calibration (MCC), described in this document and more detailed in ISO 15024.

9. Data Analysis

9.1. Delamination growth rate, da/dN

There are two possible ways to determine delamination growth rates da/dN:

Method A: da/dN can be computed using a secant or point-to-point method: the slope of a straight line connecting two adjacent points on the delamination length, a, versus cycle number, N, curve is calculated with

$$\frac{da}{dN} = \frac{a_{i+1} - a_i}{N_{i+1} - N_i} \tag{1}$$

This approximation is reasonable if the delamination length increments are small. However, if delamination length increments are too small, this approximation gives significant scatter.

For the determination of the cyclic strain energy release rate the average delamination length, ā, is normally used with

$$\bar{a} = \frac{1}{2}(a_{i+1} + a_i) \tag{2}$$

Method B: dA/dN can be calculated according to a standardised method described in ASTM E647-15a:

This incremental polynomial method for computing da/dN involves fitting a second order polynomial (parabola) to sets of (2n+1) successive data points, where n is usually 1, 2, 3 or 4. The regression parameters are determined by the least squares method, that is minimisation of the square of deviations between observed and fitted values of delamination length. Since this method is not able to describe the delamination rates between the first and the last pair of data points, these have to be evaluated using the secant or point-to-point technique which simply involves calculating the slope of the straight line connecting two adjacent data points on the a vs. N curve as described above (method A).

For the second and the second to last set of data points the 3-point-method is used (m=1), that is, the regression polynomial is applied to the first and last three data points and evaluated for the medium point (i. e., the second or second to last).

Analogous, for the third and third to last data point m=2 (5-point-method) and for all further data m=3 (7-point-method). A schematic illustration of this incremental polynomial method is depicted in Fig. 3. The method to calculate da/dN is described in ASTM E647-15a. In Chapter 6 a macro written in a Microsoft Excel workbook is explained. This workbook should be used within this round-robin.

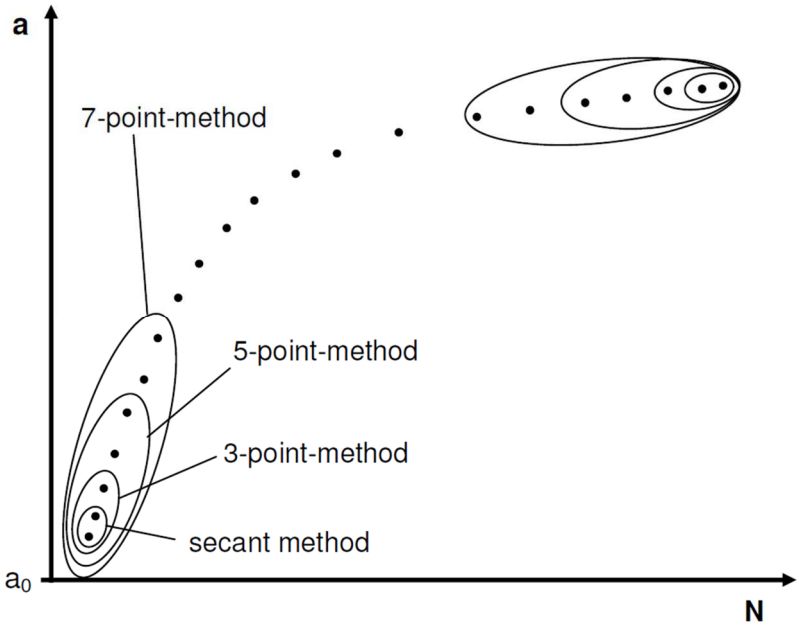

Figure 3 Schematic illustration of a typical a vs. N-graph (displacement control) for the determination of the cyclic interlaminar crack growth rate, da/dN

(logarithmic fitting of machine data – load P and displacement δ – for compliance based determination of delamination length increments)

9.2. Calculation of G_I

In general, the strain energy release rate for mode I, G_I, can be expressed according following equation:

$$G_I = \frac{1}{2B} P^2 \frac{dC}{da} \tag{3}$$

where B is the specimen width, P the applied load, C the specimen compliance and a the delamination length. By substituting P with the maximum and minimum load occurring in a fatigue cycle, the maximum and minimum strain energy release rates, G_{Imax} and G_{Imin}, can be determined. The cyclic strain energy release rate, $\Delta\sqrt{G_I}$, is then given by

$$\Delta\sqrt{G_I} = \left(\sqrt{G_{Imax}} - \sqrt{G_{Imin}}\right)^2 \tag{4}$$

G_I values should be calculated using the Modified Compliance Calibration (MCC) method as described in ISO 15024. One should note however that the calibration equation of the Modified Compliance Calibration (MCC) method should be applied using the load line displacements and loads measured at both the minimum and maximum of the cycle!

Establish the relation between the delamination length and the compliance by plotting the width-normalised cube root of compliance $(BC)^{1/3}$, or $(BC/N)^{1/3}$ if load blocks are used, as a function of the thickness normalised delamination length, a/2h (s. Fig. 4). The slope of this relation is defined as m.

The energy release rate is then given by:

$$G_I = \frac{3m}{2(2h)} \left(\frac{P}{B}\right)^2 \left(\frac{BC}{N}\right)^{2/3} F \tag{5}$$

where F (large displacement correction) and N (load block correction) are given by respectively

$$F = 1 - \frac{3}{10}\left(\frac{\delta}{a}\right)^2 - \frac{2}{3}\left(\frac{|\delta|_1}{a^2}\right) \tag{6}$$

and

$$N = 1 - \left(\frac{l_2}{a}\right)^3 - \frac{9}{8}\left[1 - \left(\frac{l_2}{a}\right)^2\right]\left(\frac{|\delta|_1}{a^2}\right) - \frac{9}{35}\left(\frac{\delta}{a}\right)^2 \tag{7}$$

Where δ is the load line displacement; l_1 and l_2 are defined in Figure 1.

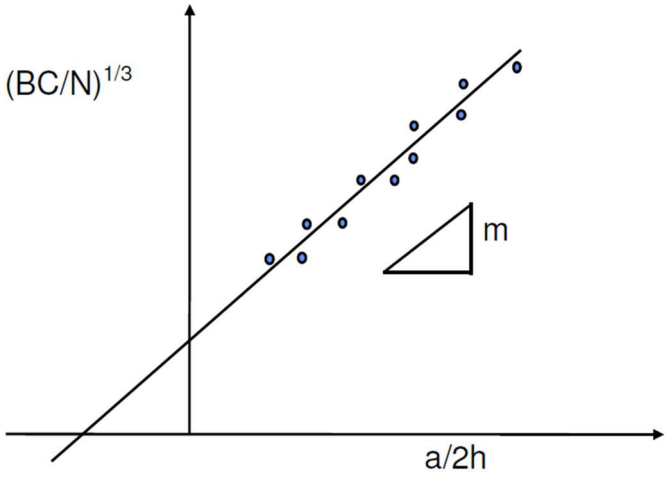

Figure 4 Schematic illustration of the linear fit used to determine the slope, m, for the MCC method

10. Data Presentation

10.1. Delamination growth resistance curves

Delamination growth rates, da/dN, should be plotted as a function of G_{Imax} or $\Delta\sqrt{G_I}$ (Figure 5). It is expected that after reaching equilibrium conditions the Paris Erdogan equation can be applied to the data sets:

$$\frac{da}{dN} = A \cdot (G_{Imax})^B \tag{8}$$

$$\frac{da}{dN} = A' \cdot \left(\Delta\sqrt{G_I}\right)^{B'} \tag{9}$$

where A, A', B and B' are constants, determined for each test sequence individually.

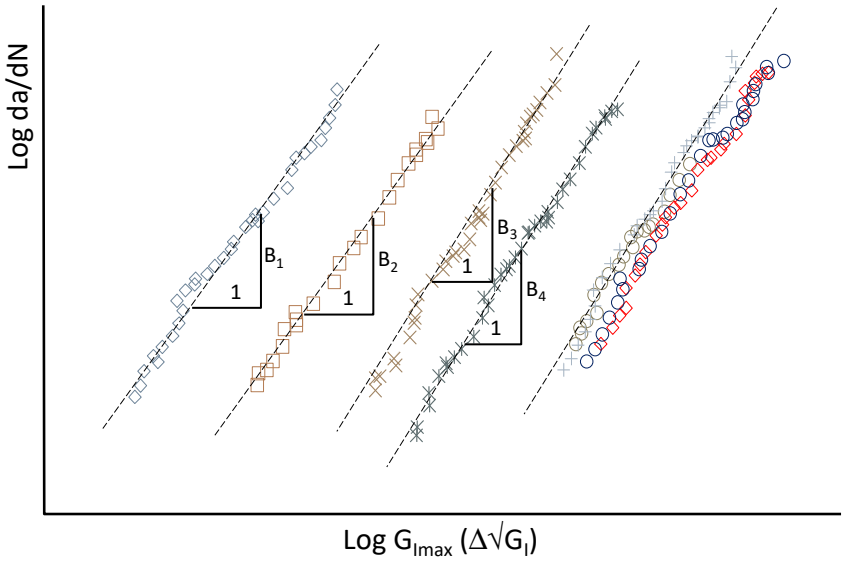

Figure 5 Schematic illustration of fatigue delamination propagation curves obtained from a single specimen

10.2. Regression

All data obtained from a single specimen should be tabulated in three columns with both $\Delta\sqrt{G_I}$ and da/dN linearized, i.e. {a-a_0 [mm]}, {log($\Delta\sqrt{G_I}$) [J/m^2]}, and {log(da/dN) [mm/cycle]}. The corresponding equation for regression then is

$$Log\left(\Delta\sqrt{G_I}\right)_{reg} = C_0 + C_1(a-a_0) + C_2 Log\left(\frac{da}{dN}\right) + C_3(a-a_0)^2 + C_4 Log\left(\frac{da}{dN}\right)^2 \qquad (10)$$

where C_i are the constants obtained through regression, and a-a_0 the crack length at the start of the first test, i.e. after pre-cracking from the Teflon insert.
After regression the zero-bridging delamination resistance curve can be determined with (a-a_0=0)

$$Log\left(\Delta\sqrt{G_I}\right)_{a-a_0=0} = C_0 + C_2 Log\left(\frac{da}{dN}\right) + C_4 Log\left(\frac{da}{dN}\right)^2 \qquad (11)$$

while all data including their scatter (i.e. the part in the bracket) can be translated to that zero-bridging curve using

$$Log\left(\Delta\sqrt{G_I}\right)_T = \left[Log\left(\Delta\sqrt{G_I}\right) - Log\left(\Delta\sqrt{G_I}\right)_{reg}\right] + Log\left(\Delta\sqrt{G_I}\right)_{a-a_0=0} \qquad (11)$$

where $\Delta\sqrt{G}$ without subscript *T* represent the values of measurement points, and where $\Delta\sqrt{G}$ with subscript a-a_0=0 represent the corresponding value at zero-bridging delamination without data scatter, and with subscript *reg* represent the values after linear regression, equation (10). The symbols with subscript *T* represent the values after translation.

11. Precision

12. Test report

[*specific instructions for ESIS TC4 round robin testing, limiting general test procedure parameter choices*]

12.1. Parameters for the Round Robin Tests

The test should be performed under mode I loading at a frequency of 5 Hz and a R-Ratio (P_{min}/P_{max}) of 0.1, 0.5 or 0.7 under displacement controlled conditions.

References

[1] Pinter, G., Stelzer, S, Determination of Mode I Fatigue Delamination Propagation in Unidirectionally Reinforced Materials, Test Protocol (Version ??)

B PROTOCOL BLOCK DIAGRAM

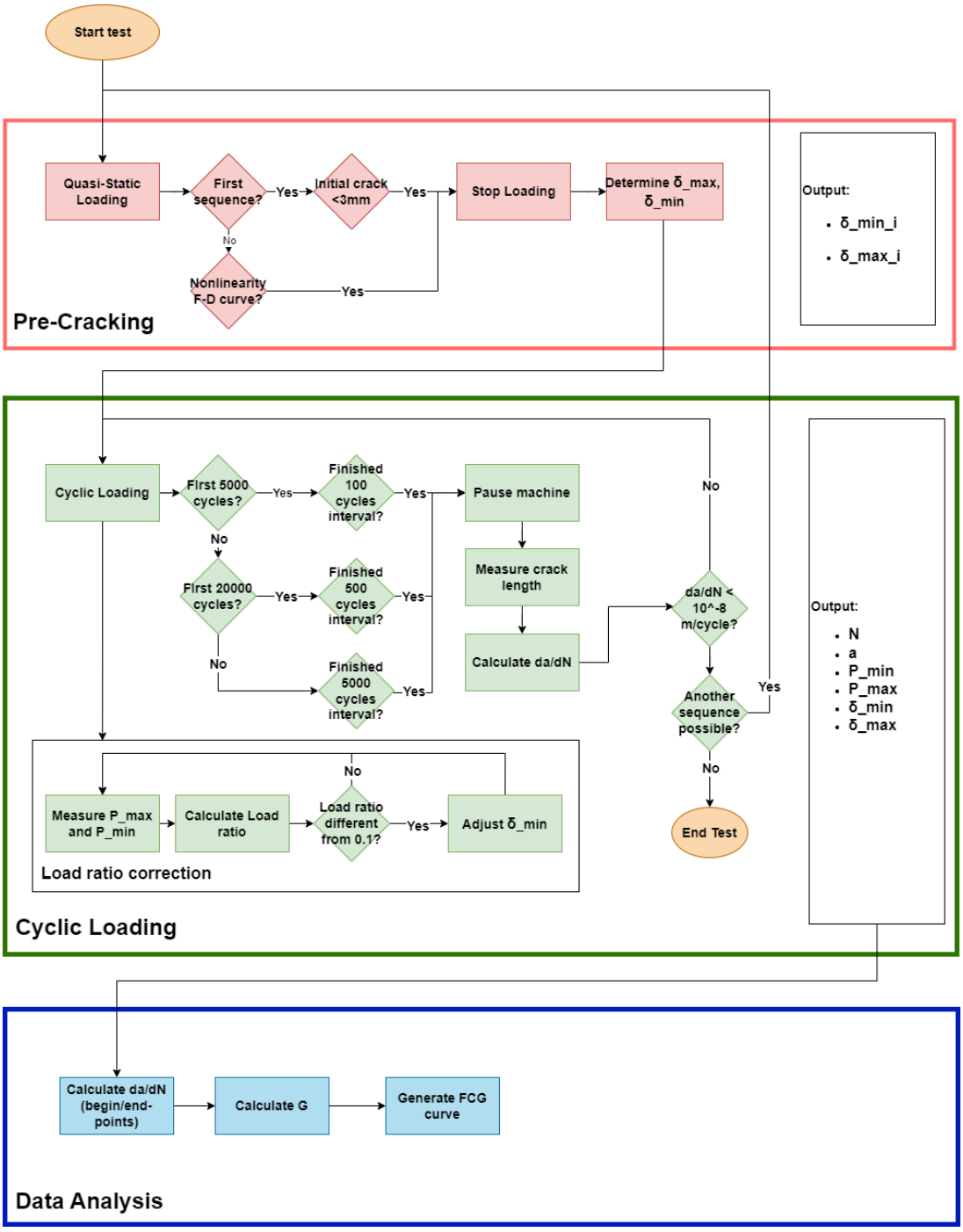

Figure B.1: Protocol Block Diagram

C DIFFERENT METHODS FOR CALCULATING G

In this Appendix is explained how the energy release rate, G, is calculated for a DCB Specimen. In Section 2.1.1, a simplified LEFM version was shown to understand the definition of G, now a more in-depth definition is given to be able to calculate the energy release rate for the tests. The Energy release rate for Mode I, G_I, can be calculated in 3 different ways. The simplest method is SBT, (simple beam theory), shown in Equation C.1:

$$G_I = \frac{3P\delta}{2Ba} \tag{C.1}$$

where P is the load, δ is the displacement, B is the specimen width, and a is the delamination length. The next method is the CBT method (corrected beam theory), see equation C.2:

$$G_I = \frac{3P\delta}{2B(a+|\Delta|)}\frac{F}{N} \tag{C.2}$$

in which Δ is a correction factor to take into account transverse shear and deformation beyond the crack tip [19] and F and N are a large displacement correction factor and a load-block correction factor respectively.
The last method is the MCC method (modified compliance calibration), see equation C.3:

$$G_I = \frac{3m}{2(2h)}\left(\frac{P}{B}\right)^2\left(\frac{BC}{N}\right)^{2/3}F \tag{C.3}$$

in which m is the slope of the linear fit of $(BC/N)^{1/3}$ over $(a/2h)$, C is the compliance and $2h$ is the specimen thickness.

The correction factors can be calculated by equation C.5 and equation C.4:

$$F = 1 - \frac{3}{10}\left(\frac{\delta}{a}\right)^2 - \frac{2}{3}\left(\frac{\delta l_1}{a^2}\right) \tag{C.4}$$

$$N = 1 - \left(\frac{l_2}{a}\right)^3 - \frac{9}{8}\left[1 - \left(\frac{l_2}{a}\right)^2\right]\frac{\delta l_1}{a^2} - \frac{9}{35}\left(\frac{\delta}{a}\right)^2 \tag{C.5}$$

where l_1 is the distance from the centre of the loading pin to the mid-plane of the specimen and l_2 is the distance from the loading pin centre to the edge of the load block. For additional details on these calculations, see ISO15024 [5] and the work of Stelzer et al. [19].

D DATA SHEET INSTRON ELECTROPULS E3000

ELECTROPULS® E3000 | LINEAR-TORSION ALL-ELECTRIC DYNAMIC TEST INSTRUMENT

The ElectroPuls® E3000 Linear-Torsion is a state-of-the-art, all-electric test instrument designed for dynamic and static testing on a wide range of materials and components. It includes Instron® advanced digital control electronics, bi-axial Dynacell™ load cell, Console software, and the very latest in testing technology – hassle-free tuning based on specimen stiffness, electrically operated crosshead lifts, a T-slot table for flexible test set ups and a host of other user-orientated features. Powered from a single-phase supply it requires no additional utilities for basic machine operation (for example, pneumatic air, hydraulics, or water).

FEATURES

- Oil-Free linear and rotary motor technology for clean conditions
- De-coupled linear/rotary actuators
- Designed for both dynamic and static testing on a variety of materials and components
- High dynamic performance, capable of performing at over 100 Hz
- ±3000 N dynamic linear load capacity and ±25 Nm dynamic torque capacity
- Electrically powered from single phase main supply, no need for hydraulic or pneumatic air supplies
- Temperature-controlled air-cooling system
- High-stiffness, precision-aligned twin column load frame with actuator in upper crosshead
- Versatile T-slot table for regular and irregular grips and specimens
- Compact instrument - frame requires less than 0.3 m² (3.2 ft²) of desk space

HARDWARE AND SOFTWARE INTERFACES DESIGNED TO PUT YOU IN CONTROL

- Console software control interface - engineered with Instron's knowledge of machine usability
- Rigidly mounted control pod with critical controls and emergency stop at your fingertips
- Electrically powered crosshead lift system with manual lever clamps for ease of test space adjustment
- System Status Indicator shows system conditions (off, on, emergency stop, and fault)

HIDDEN TECHNOLOGY DESIGNED TO IMPROVE YOUR TEST

- Patented, stiffness-based loop tuning system in both axes
- Unique actuator bearing system that maintains load string alignment when offset or lateral loads are induced by specimens or fixtures
- An optical encoder for precise digital extension control and a dedicated position channel for set up and end of test
- Digital two-axis control based on the industry's most advanced controller
- Dynacell advanced load cell technology for faster testing and reduction of inertial errors

A HIGH LEVEL OF VERSATILITY

- Readily adjustable test space to suit a wide variety of specimens, grips, fixtures, and accessories
- 60 mm (2.36 in) linear stroke, ±135° or ±16 revolutions, for a wide range of tests, as well as ease of specimen set up
- Twin column configuration provides easy access to the test area
- Compatible with WaveMatrix™2, Bluehill® Universal* and Application Specific software
- Compatible with a large range of grips, fixtures, chambers, saline baths, video extensometers, and other accessories

*Only supported in desktop mode

INSTRON®
The difference is measurable®

SPECIFICATIONS

Linear Dynamic Capacity	±3000 N (±675 lbf)
Linear Static Capacity	±2100 N (±472 lbf)
Torsional Dynamic	±25 Nm (±221 in-lb)
Torsional Static Capacity	±18 Nm (±157 in-lb)
Stroke	60 mm (2.36 in)
Rotation	±135˚ or ±16 revolutions; user configurable
Load and Torque Weighing Accuracy	±0.5 % of indicated load or torque, or ±0.005 % of load cell capacity, whichever is greater
Daylight Opening	861 mm (34 in) maximum with actuator at mid stroke
Configuration	Twin-column with actuator in upper crosshead
Mounting	Tabletop: Vertical
Lift and Locks	Electrically powered lifts with manual lever clamps
Load Cell	±5 kN ±25 Nm Dynacell™
Weight	250 kg (551 lb) [frame] 70 kg (154 lb) [controller]
Electrical Supply	200 VAC to 240 VAC 32A single phase 50/60 Hz
Cooling	Temperature-controlled air cooling
Operating Temperature	+10 to +30˚C (+50 to +86˚F)

INTERFACES

Actuator	3 x M6 on 75 mm PCD 3 x M6 on 57 mm PCD
T-Slot Table	M6 x 1 right hand central thread 3 x M6 holes on 75 mm PCD 3 x M6 holes on 57 mm PCD 6 x M10 holes on 100 mm PCD 3 x M10 holes on 125 mm PCD 4 x M10 holes on a 280 mm x 90 mm accessory rectangle 4 x M6 T-slots spaced 80 mm and 100 mm from centre

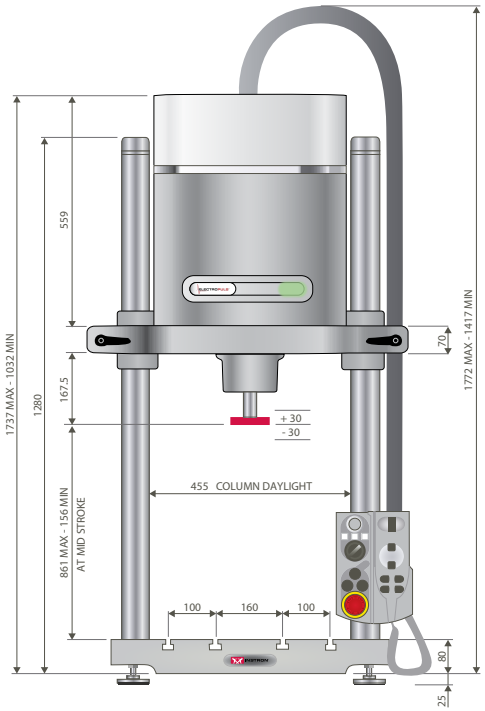

E3000 dimensions: front view

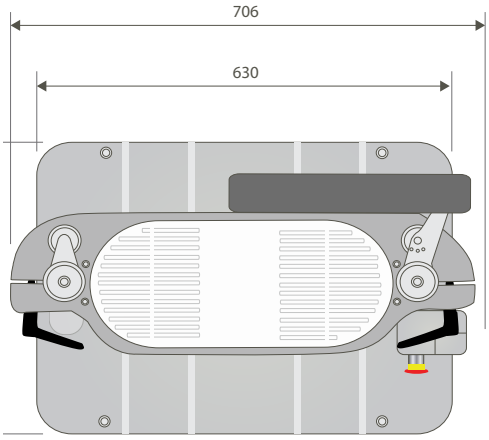

E3000 dimensions: plan view

ACCESSORIES

1300-304	Safety Screen for E3000 test instrument
1300-311	High stiffness table
2527-203	±1 kN (225 lbf) ±25 Nm (220 in-lb) Biaxial Dynacell
2742-205	±3 kN ±25 Nm Linear-Torsion Pneumatic Wedge-Action Grips
2742-206	±3 kN ±25 Nm Linear-Torsion Mechanical Wedge-Action Grips
2810-500	3-Point Bend Fixture
2810-505	4-Point Bend Fixture Conversion Kit
2840-030	20 kN Compression Platens
3117-082	ElectroPuls Pullrod kit
3119-605[1]	Environmental Chamber
2718-013	Pneumatic Grip Air Kit for Dynamic Systems

Notes: 1. Requires Pull-rods & Mounting Brackets

www.instron.com

INSTRON

Worldwide Headquarters
825 University Ave, Norwood, MA 02062-2643, USA
Tel: +1 800 564 8378 or +1 781 575 5000

European Headquarters
Coronation Road, High Wycombe, Bucks HP12 3SY, UK
Tel: +44 1494 464646

E DATA SHEET DYNAMIC LOAD CELL

DYNAMIC SYSTEMS LOADCELLS

250 N - 2,500 kN

Instron® load cells are a key part of a materials testing system. Among our competitors, Instron is the only global materials testing supplier that designs and manufactures its own load cells. This ensures that Instron load cells meet the unique requirements of materials testing such as; high accuracy over a wide measurement range, high stiffness, resistance to offset loads, accurate alignment and excellent zero stability.

During tests carried out on dynamic machines, elements of the system are subject to acceleration. As a result, in addition to the force applied to the specimen, the load cell also reads forces resulting from its own movement and the mass of the grips and fixtures attached to it.

The accelerometer in a Dynacell™ is right at the heart of the load cell, directly on the load axis. This removes the risk of errors in the acceleration reading resulting from off center loading. This way, the accelerometer is on the load line eliminating both amplitude and phase errors and automatic set-up takes less than one minute.

Dynacell 2527 Series 250 N - 2500 kN

The 2527 Series load cells are designed for use with Dynamic Testing Systems; offering exceptional performance with the ability to measure forces as low as 1/250th of the force capacity to an accuracy of 0.5% of reading. Automatic transducer recognition and electrical calibration, makes them easy to use. The load cells can withstand loads up to 150% of their force capacity without damage and 300% without mechanical failure. All Instron load cells are individually temperature-compensated and tested for accuracy and repeatability on calibration apparatus that is traceable to international standards, with a measurement uncertainty that does not exceed one-third of the permissible error of the load cell.

BENEFITS

- Force capacities from ±250 N to ±2500 kN (56 -562500 lbf)
- Torque capacities from ±25 Nm to ±2000 Nm (225 - 17702 in-lb)
- Suitable for a range of test types, including tension, compression, cyclic and reverse stress
- Automatic recognition with electronic serial number and electrical calibration allows for simple, error-free operation
- 300% of force capacity overload capability –reduces the possibility of damage
- Precision machining and construction along with high axial and lateral stiffness helps to maintain system alignment
- Low sensitivity to offset loads improves consistency of results
- Complies with all international force measurement standards, including BS1610 Part 1 1992 Grade 0.5, ASTM E4, ISO 7500-1 class 0.5, EN10002-2 class 0.5 and JIS B7721, B7733
- Fatigue life in excess of 109 full stress reversed cycles
- Highly accurate static load cell, with a measurement accuracy better than 0.25% of reading down to 1% of the load cell full scale. When used with 8800MT, an accuracy of 0.5% of reading down to 1/250th of the load cell full scale is easily achieved.

INSTRON®

The difference is measurable®

SPECIFICATIONS

Catalogue Number	Force Capacity		Torque Capacity		Mechanical Fitting (Frame)	Mechanical Fitting (Load String)	Effective Length		Diameter		Weight	
	kN	lbf	Nm	in-lb			mm	in	mm	in	kg	lb
2527-131	±0.25	56	-	-	3x M6 on 57 mm PCD	Central M6 x 1	42	1.65	75	2.95	1	2.2
2527-130	±1	225	-	-	3x M6 on 57 mm PCD	Central M6 x 1	42	1.65	75	2.95	1	2.2
2527-302	±1	225	±25	±225	3x M6 on 75 mm PCD	3x M6 on 75 mm PCD or 3x M6 on 57 mm PDC	68	2.68	94	3.7	1,3	2,87
2527-129	±2	450	-	-	3x M6 on 57 mm PCD	Central M6 x 1	42	1.65	75	2.95	1	2.2
2527-153	±5	1,125	-	-	3x M6 on 75 mm PCD	3x M6 on 75 mm PCD or 3x M6 on 57 mm PDC	68	2.68	94	3.7	2	4.4
2527-303	±5	1,125	±25	±225	3x M6 on 75 mm PCD	3x M6 on 75 mm PCD or 3x M6 on 57 mm PDC	68	2.68	94	3.7	2	4.4
2527-102	±10	2,250	-	-	6x M6 on 75 mm PCD	Central M20x1.5	71	2.8	107	4.2	4	8.8
2527-202	±10	2,250	±100	±880	6x M8 on 75 mm PCD	6x M8 on 75 mm PCD	86	3.38	94	3.7	2.5	5.5
2527-205	±25	5,620	±150	±1300	6x M8 on 75 mm PCD	6x M8 on 75 mm PCD	86	3.38	94	3.7	2.5	5.5
2527-101	±25	5,620	-	-	Central M20x1.5 or 6 x M10 on 75 mm PCD	Central M20x1.5	71	2.8	107	4.2	4	8.8
2527-201	±25	5,620	±100	±880	6x M8 on 75 mm PCD	6x M8 on 75 mm PCD	86	3.38	94	3.7	2.5	5.5
2527-100	±50	11,250	-	-	Central M30x2 or 6x M10 on 100 mm PCD	Central M30x2	99	3.9	154	6.06	10	22
2527-111	±100	22,500	-	-	Central M30x2 or 6x M10 on 100 mm PCD	Central M30x2	99	3.9	154	6.06	10	22
2527-115	±250	56,250	-	-	Central M48x2	Central M48x2	131	5.15	203	8	25.5	56.21
2527-125	±500	112,500	-	-	Central M72	Central M72x2 6x M20 on 150 mm PCD 6x M30 on 225 mm PCD	232	9.13	305	12	95	209.4
2527-120	±1000	225,000	-	-	Central M100	Central M100 6x M20 on 150 mm PCD 12x M30 on 225 mm PCD	360	12.17	305	12	140	308.6
2527-140	±2500	562,500	-	-	Central M150	Central M150	450	17.71	428	16.85	322	710

INSTRON

Worldwide Headquarters
825 University Ave, Norwood, MA 02062-2643, USA
Tel: +1 800 564 8378 or +1 781 575 5000

European Headquarters
Coronation Road, High Wycombe, Bucks HP12 3SY, UK
Tel: +44 1494 464646

CEAST Headquarters
Via Airauda 12, 10044 Pianezza TO, Italy
Tel: +39 011 968 5511

F DATA SHEETS CAMERA & LENS

U3-3800CP-M-GL Rev.2.2 (AB12832)

In series
The model is in series and available for the long term.



Specification

Sensor

Sensor type	CMOS Mono
Shutter	Rolling shutter
Sensor characteristic	Linear
Readout mode	Progressive scan
Pixel Class	20 MP
Resolution	20.44 Mpix
Resolution (h x v)	5536 x 3692 Pixel
Aspect ratio	3:2
ADC	12 bit
Color depth (camera)	12 bit
Optical sensor class	1"
Optical Size	13.286 mm x 8.861 mm
Optical sensor diagonal	15.97 mm (1/1")
Pixel size	2.4 µm
Micro lens shift	0.00
Manufacturer	Sony
Sensor Model	IMX183CLK-J
Gain (master/RGB)	-/-
AOI horizontal	same frame rate
AOI vertical	same frame rate
AOI image width / step width	256 / 16
AOI image height / step width	1 / 1
AOI position grid (horizontal/vertical)	16 / 1
Binning horizontal	increased frame rate
Binning vertical	increased frame rate
Binning method	M/C automatic
Binning factor	2 / 4 / 8
Subsampling horizontal	same frame rate
Subsampling vertical	same frame rate
Subsampling method	M/C automatic
Subsampling factor	2, 4, 8

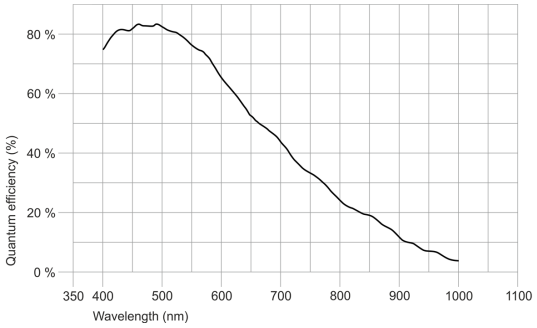

IDS Imaging Development Systems GmbH
Dimbacher Str. 10 · 74182 Obersulm · Germany · Phone +49 7134 96196-0 · E-mail info@ids-imaging.com

Model

Frame rate freerun mode (in 8-bit mode)	19 fps
Frame rate trigger (continuous)	10 fps
Frame rate trigger (maximum)	10 fps
Exposure time (minimum - maximum)	0.053 ms - 814 ms
Long exposure (maximum)	30000 ms
Power consumption	1.8 W - 3.5 W
Image memory	128 MB

Ambient conditions

The temperature values given below refer to the outer device temperature of the camera housing.

Device temperature during operation	0 °C - 55 °C / 32 °F - 131 °F
Device temperature during storage	-20 °C - 60 °C / -4 °F - 140 °F
Humidity (relative, non-condensing)	20 % - 80 %

Connectors

Interface connector	USB 3.0 micro-B, screwable
I/O connector	8-pin Hirose connector (HR25-7TR-8PA(73))
Power supply	USB cable

Pin assignment I/O connector

1	Ground (GND)
2	Flash output with optocoupler (-) - Line 1
3	General Purpose I/O (GPIO) 1 - Line 2
4	Trigger input with optocoupler (-) - Line 0
5	Flash output with optocoupler (+) - Line 1
6	General Purpose I/O (GPIO) 2
7	Trigger input with optocoupler (+) - Line 0
8	Output supply voltage, 5 V (100 mA)

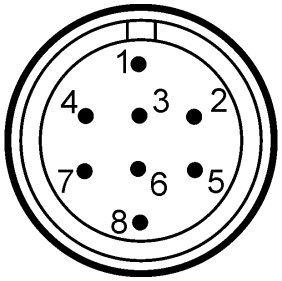

Design

Lens Mount	C-Mount
IP code	IP30
Dimensions H/W/L	29.0 mm x 29.0 mm x 29.0 mm
Mass	49 g

Features

Image Acquisition	Freerun	✓
	Software trigger	✓
	Hardware trigger	✓
	Trigger controlled exposure	-
	Denoiser	✓
	Long exposure	✓
	Line scan	-
	Line scan highspeed	-
	Global start	-
Flashing	Flashing	✓
	PWM flashing	✓

IDS Imaging Development Systems GmbH
Dimbacher Str. 10 · 74182 Obersulm · Germany · Phone +49 7134 96196-0 · E-mail info@ids-imaging.com

Image Adjustments

Auto exposure	✓
Auto gain	✓
Auto whitebalance	-
Color correction	-
Gamma	✓
LUT	✓
Mirror/flip	Y

On-board Image Processing

Pixel formats	Mono8 Mono10 Mono10p Mono12 Mono12p
Region of interest	✓
Decimation (FPGA)	✓
Decimation (Sensor)	-
Binning (FPGA)	✓
Binning (Sensor)	2x2 Color binning on monochrome sensor may cause image artifacts. Horizontal and vertical binning can only be applied jointly.

Others

Chunks	✓
Sequencer	-
Events	✓
Firmware update	✓
1st supported firmware version	2.20

IDS Imaging Development Systems GmbH
Dimbacher Str. 10 · 74182 Obersulm · Germany · Phone +49 7134 96196-0 · E-mail info@ids-imaging.com

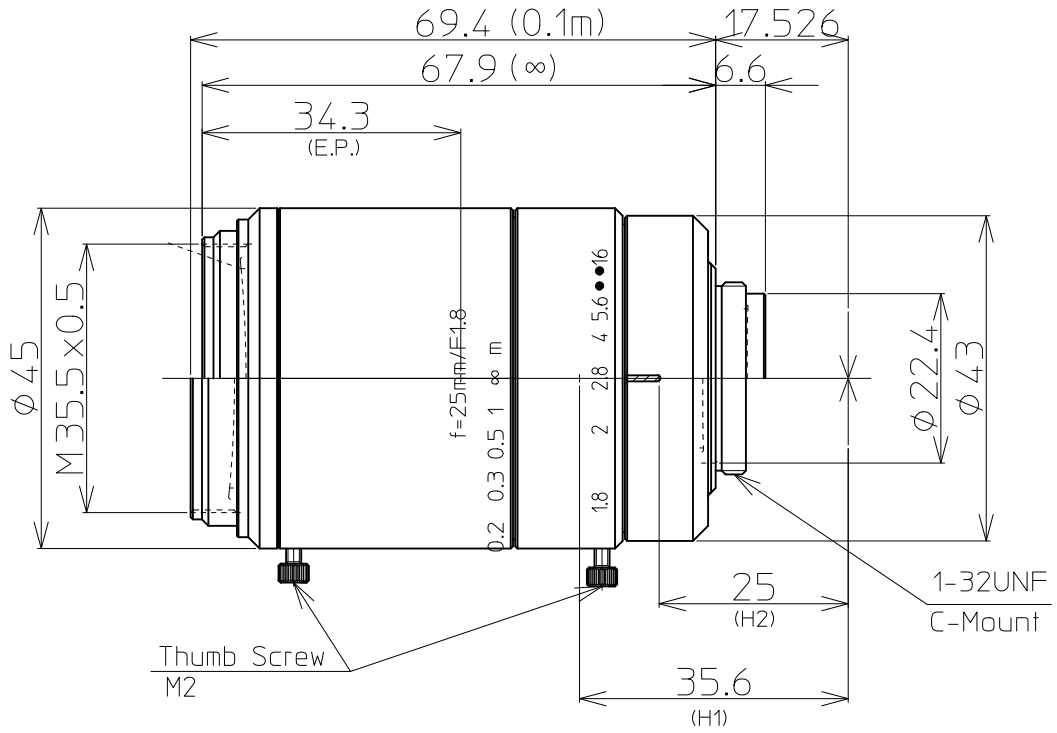

1.1" 1.8/25mm C		1.1"	1"	2/3"
FOCAL LENGTH		f=25mm		
F-NUMBER		F=1.8-16		
PICTURE SIZE		10.6x14.1mm	9.6x12.8mm	6.6x8.8mm
ANGLE OF VIEW (∞)	VER. ANGLE	23.9°	21.7°	15.0°
	HOR. ANGLE	31.5°	28.7°	20.0°
	DIA. ANGLE	38.8°	35.5°	24.8°
DISTORTION (TV)		-0.3%	-0.2%	-0.1%
FIELD OF VIEW (MINIMUM FOCUS DISTANCE)	VER.	48mm	44mm	30mm
	HOR.	64mm	58mm	40mm
	DIA.	80mm	73mm	50mm
MINIMUM FOCUS DISTANCE		0.1m		
FLANGE BACK		17.526mm in air		
BACK FOCUS		13.3mm in air		
FILTER SCREW SIZE		M35.5x0.5		
FRONT/REAR EFFECTIVE DIA.		FRONT φ29.0mm REAR φ18.4mm		
MOUNT		C-MOUNT		
EXIT PUPIL		-67.7mm		
TEMPERATURE RANGE		-10~+50°C		
STORAGE TEMPERATURE RANGE		-20~+60°C		
RESOLUTION CENTER/CORNER		CENTER 200lp/mm CORNER 100lp/mm		
WEIGHT		220g		

NOTE:Specifications and availability are subject to change without notice

注）本仕様については、予告なしに変更する場合があります。

		尺度 1/1	工場番号
		機種名 1.1" F1.8 f=25mm	
		機種番 LM25FC24M 外観図	
2017.09.15	作成年月日		

G CALIBRATION INSERT

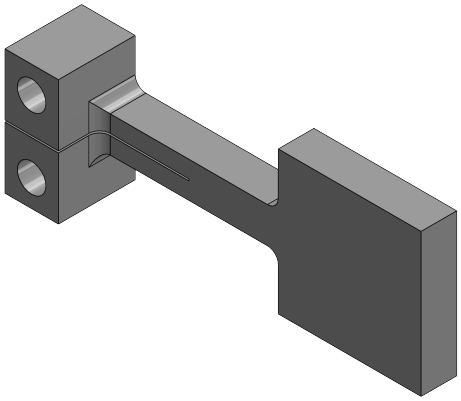

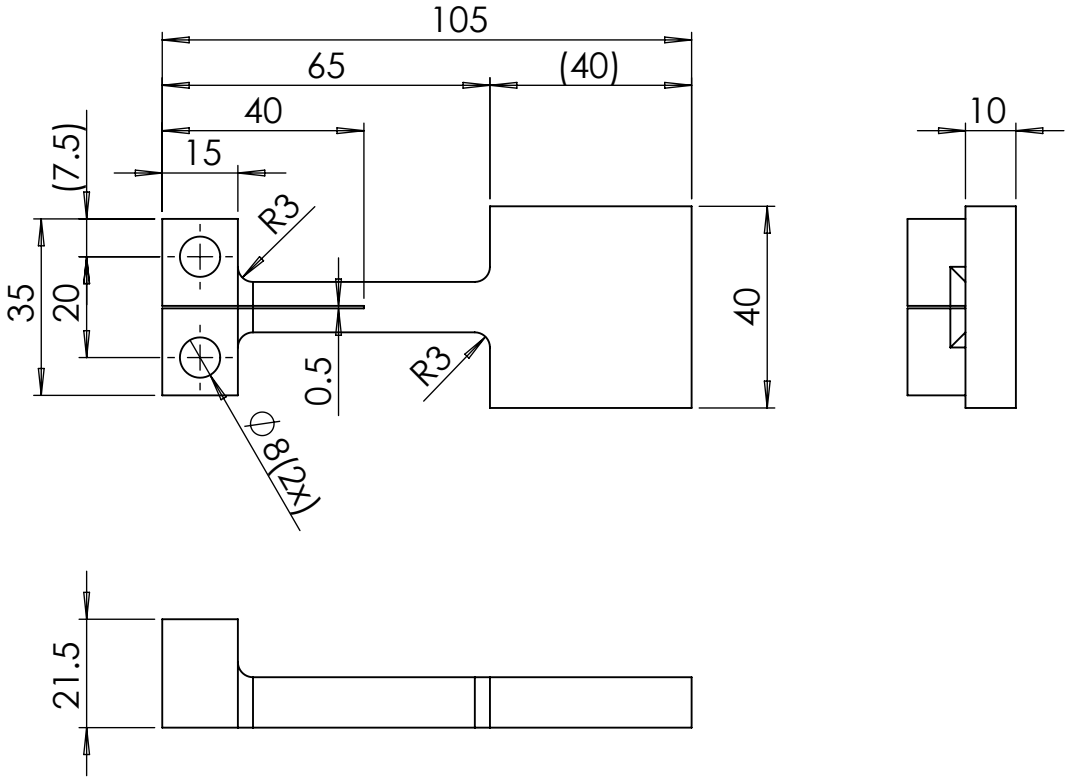

UNLESS OTHERWISE SPECIFIED: DIMENSIONS ARE IN MILLIMETERS SURFACE FINISH: TOLERANCES: LINEAR: ANGULAR:	FINISH:		DEBURR AND BREAK SHARP EDGES	DO NOT SCALE DRAWING	REVISION	
	NAME	SIGNATURE	DATE	TITLE: Calibration insert		
DRAWN	Friso		01/2024			
CHK'D						
APPV'D						
MFG						
Q.A				MATERIAL:	DWG NO. -	A4
				WEIGHT:	SCALE:1:2	SHEET 1 OF 1

H USER INTERFACE

H.1 DCB Fatigue Tester

Figure H.1: 'DCB Fatigue Tester' User Interface

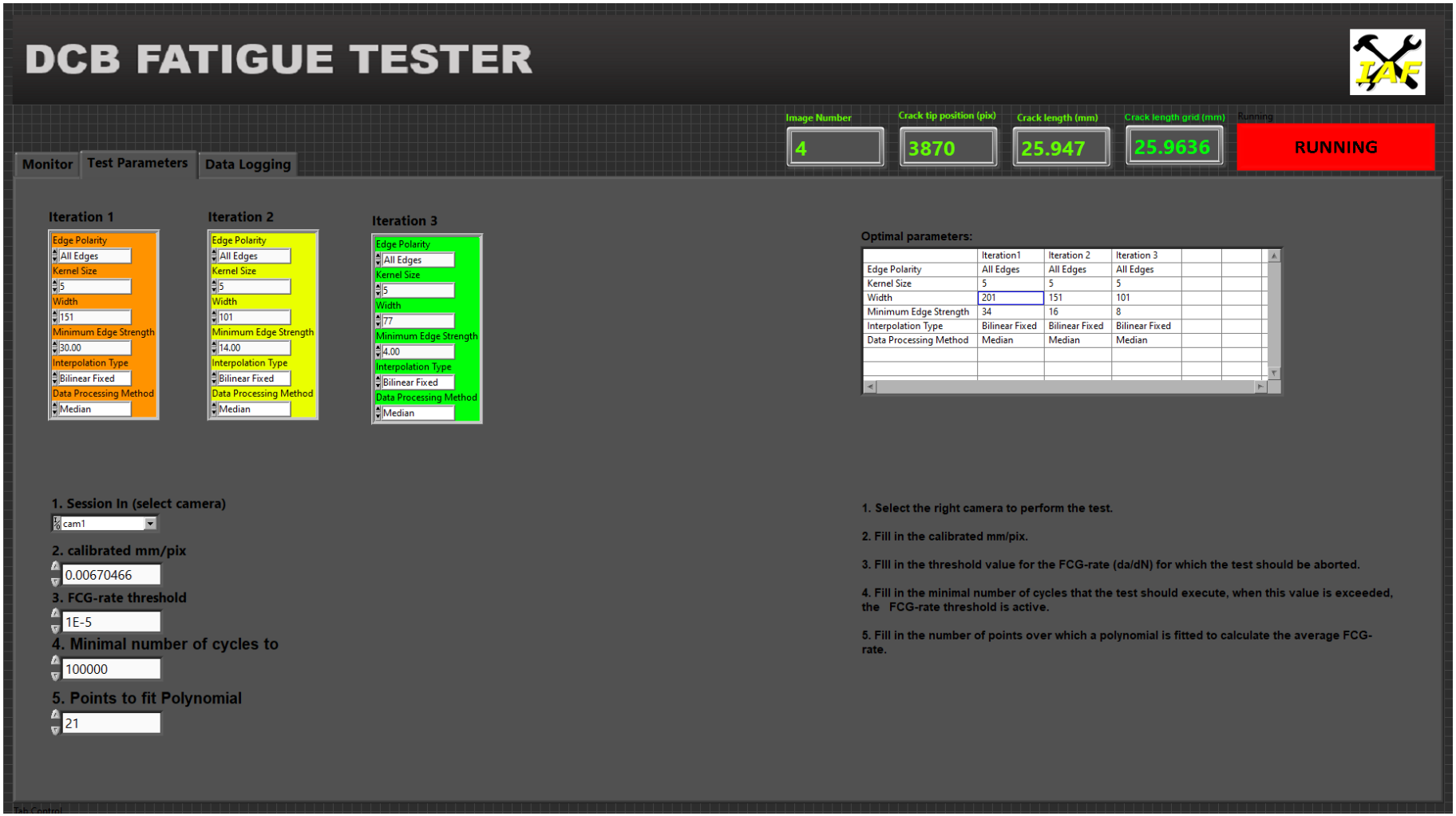

Figure H.2: 'DCB Fatigue Tester' User Interface

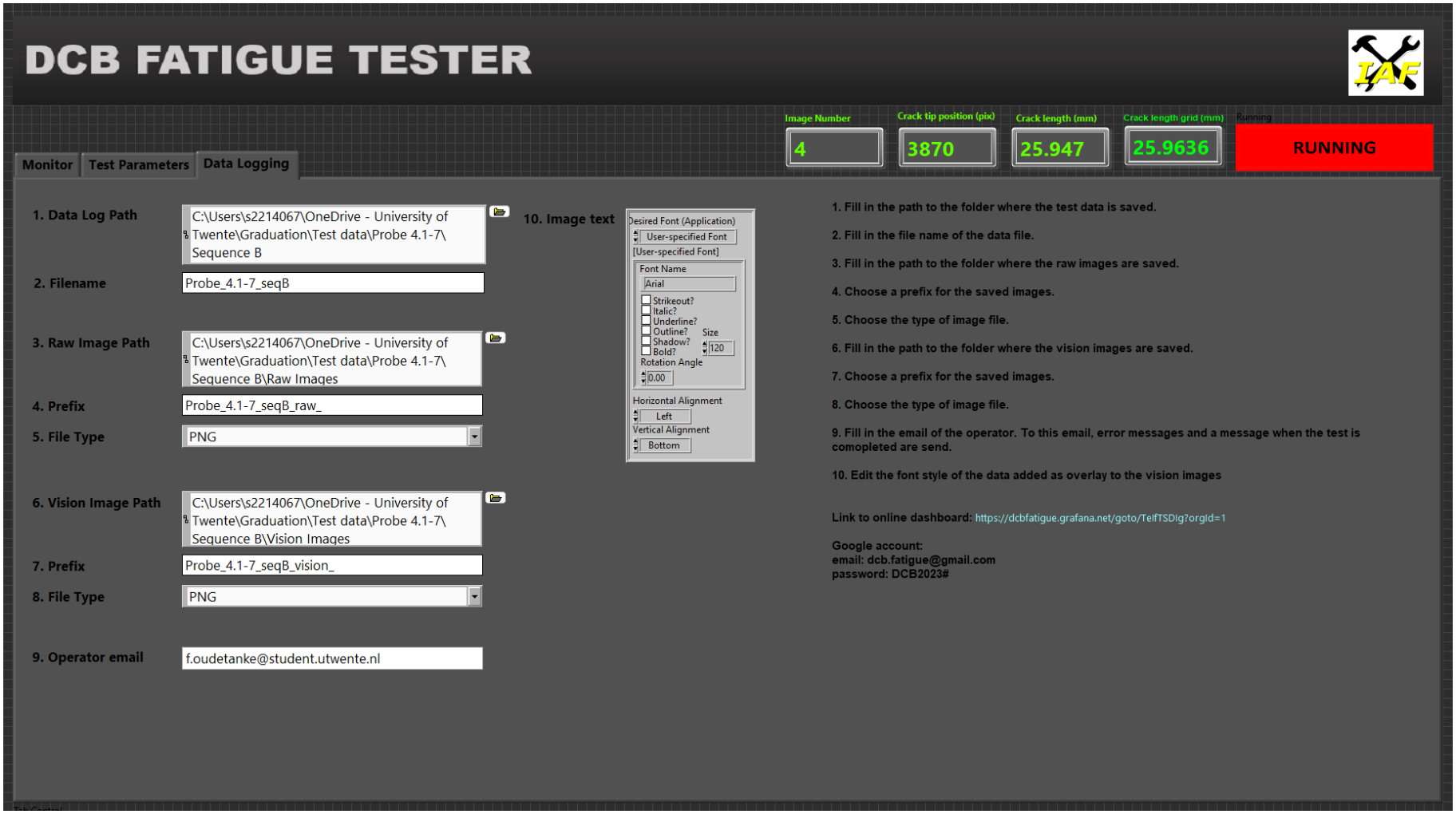

Figure H.3: 'DCB Fatigue Tester' User Interface

H.2 Live Tester

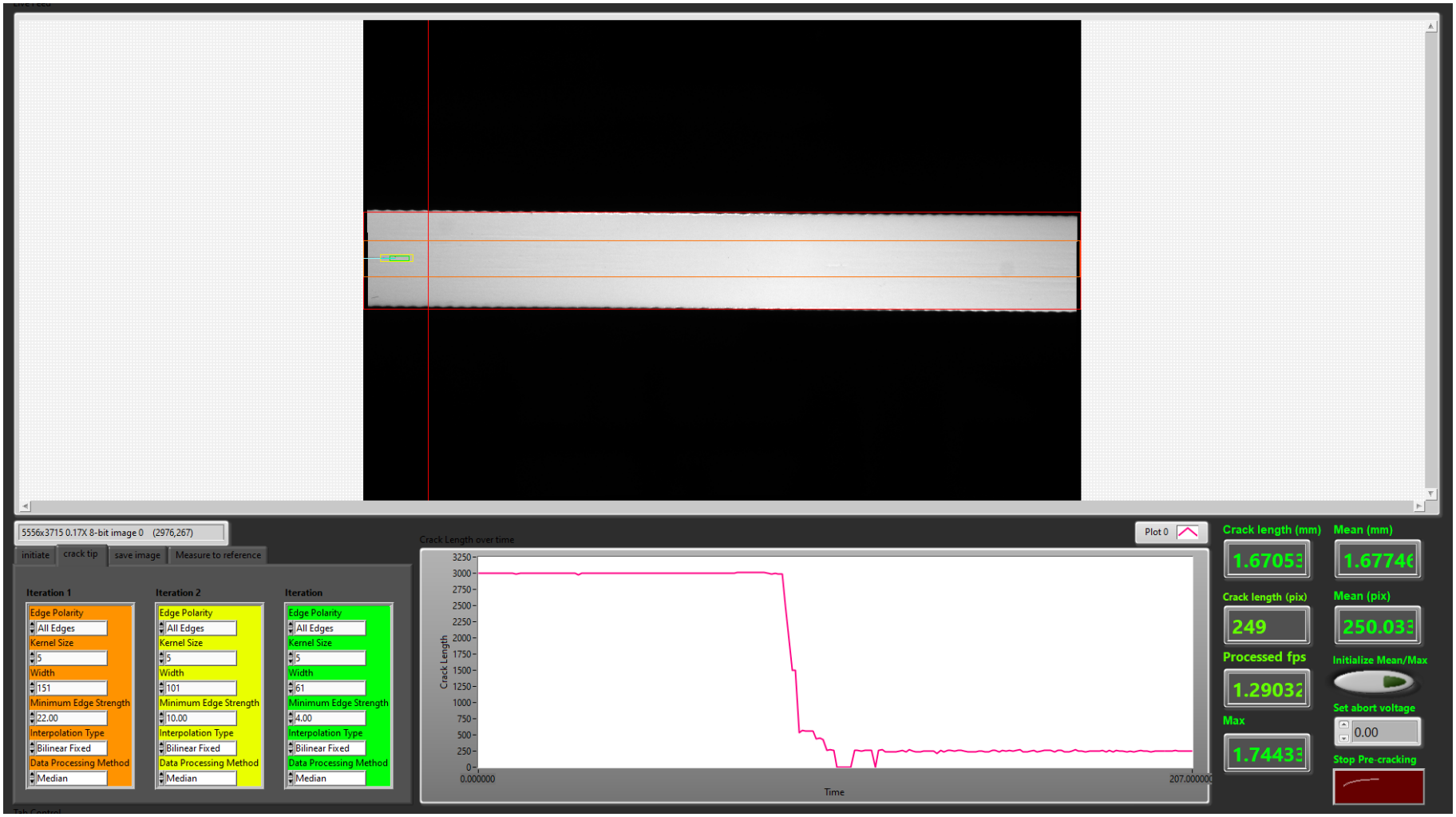

Figure H.4: 'Live Tester' User Interface

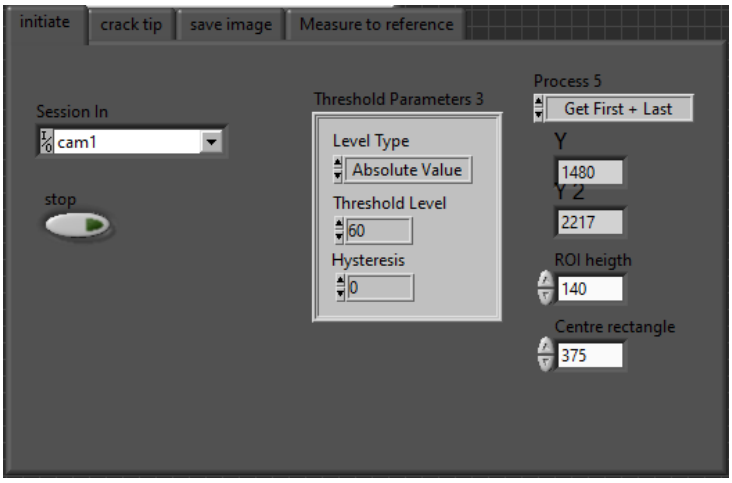

Figure H.5: 'Live Tester' User Interface

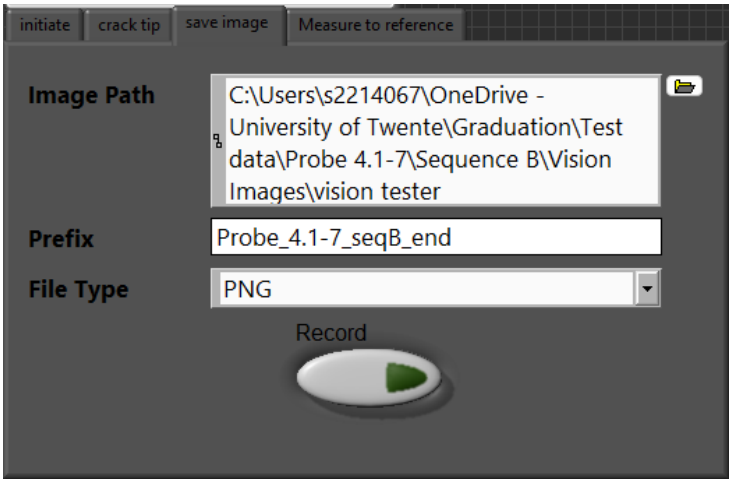

Figure H.6: 'Live Tester' User Interface

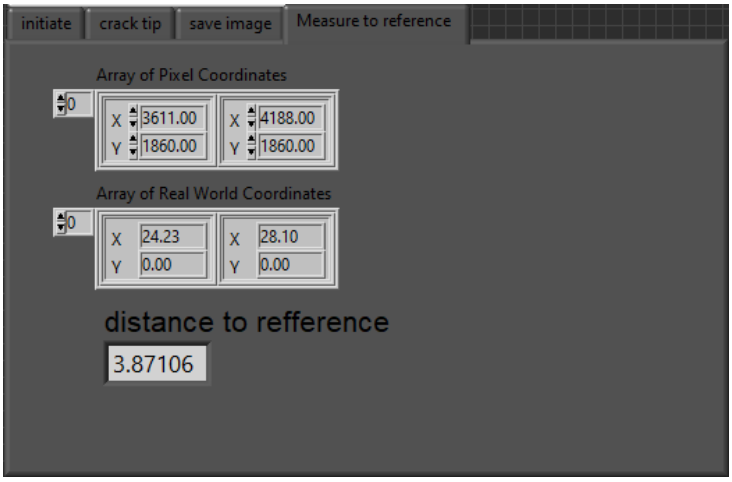

Figure H.7: 'Live Tester' User Interface

I ESTIMATION OF MEASUREMENT UNCERTAINTY

To estimate the measurement uncertainty in the current test setup, the International Organization for Standardization's Guide to the Expression of Uncertainty in Measurement (ISO GUM) [46], along with the documentation by Adams [47], are utilized. For simplification, the energy release rate is determined using the Simple Beam Theory (SBT) formulation, which is expressed as follows:

$$G_I = \frac{3P\delta}{2ba} \tag{I.1}$$

The uncertainty associated with each parameter, specifically P, δ, and b, needs to be determined under the assumption of a rectangular distribution. For parameters characterized by a rectangular distribution, the standard uncertainty is calculated using the following formula:

$$u = \frac{a}{\sqrt{3}} \cong 0.5774a \tag{I.2}$$

Where the containment limits are denoted as $\pm a$, the standard uncertainty for each parameter is obtained as follows:

- Force, P: The containment limits are obtained form the data sheet, which can be seen in Appendix E. Which states an accuracy of $\pm 0.5\%$ for 1/250th of the load cell full scale, i.e. 0.5% of $5kN$ is $0.1N$.
- Displacement, δ: As per ASTM E2309 [48], it is assumed that the testing machine passes the 'Class A' classification, i.e. the testing error on the displacement reading is not greater than $\pm 0.025mm$ or $\pm 0.5\%$ of the total stroke of $60mm$. Hence, the maximum displacement error is considered to be $0.3mm$.
- Width of the specimen, B: The width is measured using a micrometer, which offers an accuracy of approximately $\pm 0.005mm$.

With these values, the standard uncertainty for each parameter can now be calculated.

$$u_P = \frac{0.1}{\sqrt{3}} = 0.057735N \tag{I.3}$$

$$u_\delta = \frac{0.3}{\sqrt{3}} = 0.1732mm \tag{I.4}$$

$$u_B = \frac{0.005}{\sqrt{3}} = 0.0028868mm \tag{I.5}$$

For the delamination length, denoted as a, the standard deviation resulting from random error is given by $u_a = 0.01313mm$. The next step involves calculating the sensitivity coefficients. These coefficients are crucial as they quantify the extent of change in the measurand (the quantity being measured) in response to variations in each input quantity. The sensitivity coefficient for an input quantity can be determined through partial derivatives of the model function f with

respect to the respective input quantities. Mathematically, the sensitivity coefficient, c_i, for an input quantity, x_i, is represented as:

$$c_i = \frac{\partial f}{\partial x_i} \tag{I.6}$$

if this is done for Equation I.1, the following is obtained:

$$c_p = \frac{\partial G}{\partial P} = \frac{3\delta}{2ba} = \frac{G}{P} \tag{I.7}$$

$$c_\delta = \frac{\partial G}{\partial \delta} = \frac{3P}{2ba} = \frac{G}{\delta} \tag{I.8}$$

$$c_B = \frac{\partial G}{\partial B} = -\frac{3P\delta}{2b^2a} = -\frac{G}{B} \tag{I.9}$$

$$c_a = \frac{\partial G}{\partial a} = -\frac{3P\delta}{2ba^2} = -\frac{G}{a} \tag{I.10}$$

To determine the values of these sensitivity coefficients, it is essential to utilize actual data from the test. In this case, data from the last measured cycle of the test is employed.

$$c_p = \frac{G}{P} = \frac{0.45J/mm^2}{38.246N} = 0.01177\frac{\frac{J}{mm^2}}{N} \tag{I.11}$$

$$c_\delta = \frac{G}{\delta} = \frac{0.45J/mm^2}{30.66mm} = 0.01468\frac{J}{mm^3} \tag{I.12}$$

$$c_B = -\frac{G}{B} = -\frac{0.45J/mm^2}{20mm} = -0.02250\frac{J}{mm^3} \tag{I.13}$$

$$c_a = -\frac{G}{a} = -\frac{0.45J/mm^2}{13.68mm} = -0.03289\frac{J}{mm^3} \tag{I.14}$$

Finally, the combined standard uncertainty, u_c is calculated with the following formula:

$$u_c = \sqrt{\sum_i c_i^2 u_i^2} = 0.003719J/mm^2 \tag{I.15}$$

Consequently, the value of G is determined to be $449.94 \pm 3.7J/m^2$.

J UPPER-BOUND CURVE

Table J.1: Values for $\Delta\sqrt{G_{thr}}$ and A to obtain master relation for TC1225 LMPAEK specimen

Sequence	$a_p - a_0(mm)$	R-ratio	$\Delta\sqrt{G_{thr}}(\sqrt{J/m^2})$	$A(J/m^2)$
A	6.82	0.1	11	1400
B	22.40	0.1	13.4	1550
C	41.96	0.1	15	1950
D	57.27	0.1	15.2	1950
E	85.11	0.1	16.5	1850

Table J.2: Values for $\Delta\sqrt{G_{thr}}$ and A to obtain master relation for M30SC/DT120 specimen

Sequence	$a_p - a_0(mm)$	R-ratio	$\Delta\sqrt{G_{thr}}(\sqrt{J/m^2})$	$A(J/m^2)$
A	4.41	0.1	8.2	210
B	22.14	0.1	9.8	275
C	39.89	0.1	11.2	380
D	57.01	0.1	12.15	660
E	73.69	0.1	13.45	800

K DIFFERENCE BETWEEN X & A

In this Appendix, the difference between the horizontally measured x and the actual delamination length a is calculated geometrically. It is assumed that the deformed shape has a constant curvature, $(1/R)$.

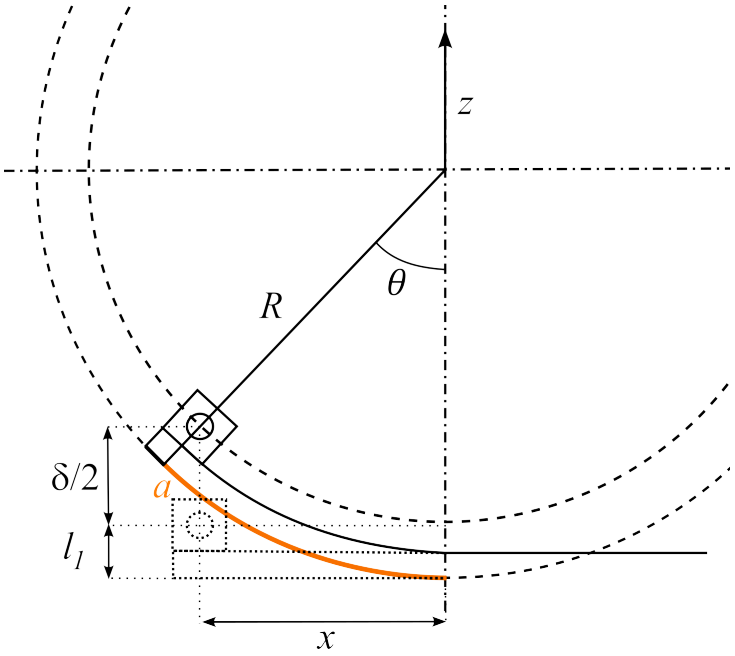

Figure K.1: Schematic illustration of the deformation with a constant curvature

The relation of a circle in Cartesian coordinates is described by:

$$(x-a)^2+(y-b)^2=r^2 \tag{K.1}$$

where (x,y) are the coordinates of any point on the circle, (a,b) are the coordinates of the centre of the circle and r is the radius of the circle. For this situation, Equation K.1 is transformed into Equation K.2 to describe the relations in Figure K.1.

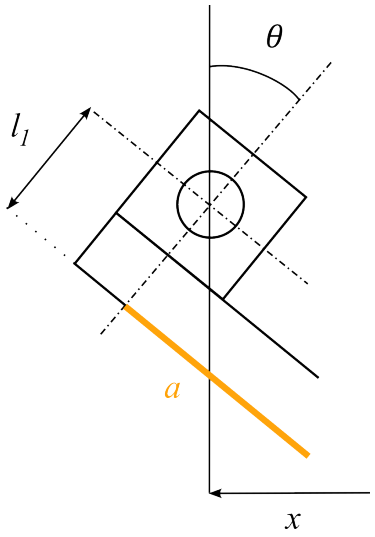

Figure K.2: Schematic illustration of the load block rotation

$$x^2 + (z - R)^2 = R^2 \tag{K.2}$$

In this Equation, z can be replaced by $\delta/2$. Subsequently, for the radius, R, the following relation is obtained:

$$R = \frac{x^2 - \delta^2/4}{\delta} \tag{K.3}$$

For x and a, the following relations are known:

$$x = (R)sin\theta \tag{K.4}$$

$$a = (R + l_1)\theta \tag{K.5}$$

Equation K.4 can be transformed to an Equation for θ:

$$\theta = sin^{-1}\left(\frac{x}{R}\right) \tag{K.6}$$

Since the known parameters are δ and x, the difference between x and a can now be calculated. The data of Sequence B and E, i.e. the test data with a short delamination length and with a long delamination length, is used. Of both sequences, the first and the last measurement point is taken, referred to as points 0 and n.

Table K.1: Validation of distortion model

	N	x	$\delta_{measure}$	R	θ	a	a/x
Seq. B_0	100	74.31	4.0447	1364	0.0545	74.89	1.00783
Seq. B_n	3e5	91.34	4.0447	2062	0.04432	91.81	1.00518
Seq. E_0	100	125.19	13.4467	1162	0.10793	126.51	1.01057
Seq. E_n	4.7e5	147.96	13.4467	1625	0.0912	149.08	1.00755

Table K.1 shows that the largest difference between x and a occurs at the start of Sequence E, which aligns with expectations since the biggest curvature is observed at this phase. However, for a complete delamination length of $126.51mm$, the difference is just a mere $1.32mm$. Therefore, the difference between dx and da can be considered negligibly small.